Développement de nanostructures à base d'AlGaN pour la fabrication de composants émetteurs de lumière UV à pompage électronique

Anjali Harikumar

THÈSE

Pour obtenir le grade de

DOCTEUR DE L'UNIVERSITÉ GRENOBLE ALPES

École doctorale : PHYS - Physique
Spécialité : NANOPHYSIQUE
Unité de recherche : PHotonique, ELectronique et Ingéniérie QuantiqueS

Développement de nanostructures à base d'AlGaN pour la fabrication de composants émetteurs de lumière UV à pompage électronique

Development of AlGaN nanostructures for the fabrication of electron-pumped UV emitters

Présentée par :

Anjali HARIKUMAR

Direction de thèse :

Eva MONROY Université Grenoble Alpes	Directrice de thèse

Rapporteurs :

NOELLE GOGNEAU
Directeur de recherche, CNRS DELEGATION ILE-DE-FRANCE SUD
NIKOLAOS PELEKANOS
Professeur, University of Crete

Thèse soutenue publiquement le **14 juin 2022**, devant le jury composé de :

NOELLE GOGNEAU Directeur de recherche, CNRS DELEGATION ILE-DE-FRANCE SUD	Rapporteure
NIKOLAOS PELEKANOS Professeur, University of Crete	Rapporteur
PIERRE RUTERANA Directeur de recherche, CNRS DELEGATION NORMANDIE	Examinateur
KUNTHEAK KHENG Professeur des Universités, UNIVERSITE GRENOBLE ALPES	Président
SEBASTIEN PLISSARD Chargé de recherche, CNRS DELEGATION OCCITANIE OUEST	Examinateur
JULIEN BARJON Professeur des Universités, UNIVERSITE DE VERSAILLES - SAINT QUENTIN	Examinateur

Invités :

STEPHEN PURCELL
Professeur des Universités, UNIVERSITE LYON 1 - CLAUDE BERNARD

Acknowledgements

My PhD was was conducted in l'Institut de recherche interdisciplinaire de Grenoble (IRIG) of the "Nanophysique et Semiconducteurs (NPSC)" group at "Commissariat à l'énergie atomique et aux énergies alternatives (CEA)" in Grenoble, France. During this time, I had the opportunity to meet and learn from incredibly talented and dynamic researchers doing impressive works in the field of nitrides. I want to take the time to sincerely thank each and every one who had a direct or indirect impact on my work (I hope I did not leave anybody out).

First and foremost, I want to thank my PhD supervisor, **Eva Monroy**. Without her incredible support, constant guidance and open mindedness, I do not think this PhD would have been this memorable or impactful in my life. Working with her, I have learnt many valuable lessons, not just in science but also in life. Her energy is contagious and makes you want to work harder while also enjoying it in the process. I will forever cherish these 3 years because of the amazing time spent with her and hope to implement everything I learnt from her in my life.

Next, I would like to thank **Stephen T. Purcell** for being a huge collaborator in my work and always extending his help for one of the most important aspects of my research work. I will always cherish the fun discussions we had at the lunch table in Lyon. I also want to deeply thank **Fabrice Donatini** for sending my way his incredible support, knowledge and help for my measurements in CNRS-Néel Institute. Unfortunately, three years were not enough for me to build enough muscle to be able to pump the helium tank manually the way he does!

I also want to thank **Yann Genuist, Yoanne Curé, Jean Dussaud** and **Fabien Jourdan** for their technical support for the MBE and other machines without which I could not performed my work. Special thanks to **Luigia** for being an immense support and help for all the admin work. I want to express my deep gratitude to **Edith Bellet-Amalric** for always helping me with the XRD measurements, **Catherine Bourgerol**, and **Martin D. Hertog** for the amazing TEM images.

I would also like to thank Jean-Michel Gerard for welcoming me in the PHELIQS group at CEA. I also want to express my gratitude towards to the heads of our NPSC lab, **Régis André** and **Bruno Gayral** for welcoming me in the team and extending any kind of support I needed. Thanks, Régis for always making sure to keep the mood light and interesting around the lab and thanks Bruno for being so effective in keeping the PL running while also taking incredible pictures at Ganext 2021. I also want to thank others who had an impact on my work, directly or indirectly: **Le-Si Dang, Christophe, Adéline Grenier, Névine Rocher**, **Moïra Hocevar**, **Gille Ledoux**, **Joël Emery, Joël Bleuse.**

I would like to extend my gratitude towards the jury of my PhD defense. I would like to first thank the reviewers: **Noëlle Gogneau** and **Nikos Pelekanos** for taking the time to review my work. I would also like to thank my PhD examination committee, **Kuntheak Kheng (president of the panel), Pierre Ruterana, Sébastien Plissard** and **Julien Barjon** for accepting to be a part of the jury and examine the PhD work and defense.

Having spent most of my time with my colleagues from CEA, it goes without saying I am thankful for each one for making this journey fun and exciting. Starting with my office-mate and real life cheerleader, **Ioanna**, then **Mada, Marion, Jane, Sergi, Rémy, Alex, Vincent, Thibault, Elçin, Sylvain, Akanksha, Saptarshi, Lucie, Matteo, Anh, Akhil, Saransh, Romain, Nathaniel, Guilerhme, Maria, Samar, Raouia, Ali, Corentin, Françis, Ghenwa, Yassine, Zijie**. I had a lovely time with everyone as we spent these years with laughter and fun. I will always cherish our Thursday night outs, NPSC weekends etc. This PhD would not have been the same without you people.

Next, I would like to thank my family and friends from India. Thank you **amma** and **accha (Rekha** and **Hari)** for always being my pillars of support. Thank you for providing your daughter the means to achieve her dreams and always showering her with love. Thanks, Arun, for being my wise young brother, always ready to extend support when needed. Thanks **Ammu edathi** and **Ponnu** (**Krishna** and **Gatha**) for being a huge source of support and advice, and for being my bestie cousins. Thanks **Rachel, Aditi, Hafsa, Annet, Kasi, Tarab** for being the nicest friends ever!

Finally, I want to thank my partner, **Cédric**, for all his help and support throughout this roller coaster journey. Thanks for taking care of me in times when I was too tired to take care of myself. You are an inspiration to me every day!

Table of Contents

1 Context and targets 7

1.1 History of UV light for disinfection 7

1.2 UV light emitters 7

1.2.1 Germicidal UV radiation 7

1.2.2 Current technologies 8

1.3 III-Nitrides for UV light emission 9

1.4 Structure of the manuscript 10

2 Introduction 11

2.1 III-Nitride semiconductors: background and concepts 11

2.1.1 Crystal properties 11

2.1.2 Band structure 14

2.1.3 Elastic properties 16

2.1.4 Spontaneous and piezoelectric polarization 17

2.2 Electron beam pumped lamps 18

2.2.1 Introduction and motivation 18

2.2.2 Working principle 19

2.2.3 Efficiency 20

2.2.4 State of the art 21

3 Experimental techniques and methods 25

3.1 Epitaxial growth 25

3.1.1 Description of PA-MBE growth technique 27

3.2 Substrates 32

3.2.1 Sapphire-based substrates 32

3.2.2 Si(111)-based substrates 33

3.2.3 Growth of nitride heterostructures: GaN, AlN, AlGaN NWs and QDs 34

3.3 Characterization techniques 39

3.3.1 X-Ray Diffraction 39

3.3.2 Transmission Electron Microscopy (TEM) 40

3.3.3 Atomic force microscopy 41

3.3.4 Scanning Electron Microscopy 43

3.3.5 Photoluminescence 43

3.3.6 Cathodoluminescence 46

3.4 Simulations 48

3.4.1 NextNano[3] 48
3.4.2 Monte Carlo simulations using CASINO software 49
4 AlGaN/AlN Quantum dots in GaN nanowires 51
4.1 Introduction and motivation 51
4.2 Design of the structure 52
4.3 Optical characterization 56
4.3.1 Photoluminescence 56
4.3.2 Cathodoluminescence 58
4.3.3 Stability under electron pumping 59
4.3.4 Penetration depth and efficiency under electron pumping 60
4.4 Conclusions 62
5 AlGaN/AlN quantum dots 65
5.1 Introduction and motivation 65
5.2 QDs with target wavelength: 270 nm 67
5.2.1 Design and growth conditions 67
5.2.2 Structural characterization 69
5.2.3 Spectral behavior 72
5.2.2 Band profile simulations 72
5.2.3 Assessment of the Internal Quantum Efficiency 76
5.2.4 Efficiency under electron beam pumping 78
5.3 Towards shorter wavelengths: Increasing the Al content 80
5.3.2 Growth conditions 80
5.3.3 Optical characterization 82
5.3.4 Power efficiency measurements 83
5.4 Conclusions 84
6 Conclusions and perspectives 87
6.1 Conclusions 87
6.2 Perspectives 88
6.2.1 Nanowire technology 88
6.2.2 Stranski-Krastanov QD technology 88
7 Bibliography 93

1 Context and targets

1.1 History of UV light for disinfection

Since the outbreak of the Ebola virus in 2014 and the more recent pandemic of the coronavirus disease 2019 (COVID-19), there has been a significant interest in germicidal ultraviolet (GUV) lamps for disinfection. The term GUV comes from the general concern among the population about ionizing radiation (like X-rays and gamma rays). Using the term, GUV prevents undesired concerns about a similarity with those radiations. Another non-technical term is germicidal light.

The first utilization of UV emission for disinfection was in 1877 for disinfecting surfaces, then in 1908 for water disinfection in Marseille, France and then 1935 for air [1–3]. GUV is being used in many countries to control airborne transmission of tuberculosis (TB) [4]. The germicidal application that saw the most progress in terms of advancement and acceptance is water disinfection. Air disinfection can be accomplished through several techniques: irradiating the air in the top of the room only, irradiating the full room (when the room is not occupied by humans or some sort of protective clothing is worn), and irradiating air as it passes through enclosed air-circulation and heating, ventilation, and air-conditioning (HVAC) systems. More-widespread use of GUV is often limited by safety concerns, but these are manageable and dismissible compared to potential advantages regarding prevention of infection.

1.2 UV light emitters

1.2.1 Germicidal UV radiation

The ultraviolet (UV) light is a band of the electromagnetic spectrum with wavelengths ranging from 10 nm to 400 nm. The UV spectral range can be divided into 4 regions depending on the wavelengths: the vacuum-UV from 10 to 200 nm, UV-C from 200 to 280 nm, UV-B from 280 to 315 nm and UV-A from 315 to 400 nm. The wavelengths ranging between 200 to 300 nm, roughly the UV-C plus a bit of UV-B will be referred to as deep ultraviolet or DUV range from now on. The response of genetic material, or deoxyribonucleic acid (DNA), to be more precise, is in the UV range [5]. UV irradiation breaks the hydrogen bond between adenine and thymine of DNA and creates a covalent bond between the thymine groups, as shown in Figure 1. The new covalent bond is much stronger than the hydrogen bond it replaces. This prevents the DNA replication process that of the microbes. Bacteria have a typical lifetime of just a few minutes, and so it is rendered harmless.

Now, there are two maxima of this response of the pathogens, both in the DUV. One at 255-270 nm and the other at 220-230 nm. The UV LEDs community has extensively studied the 255-270 nm range and much speculation has been going around for the range of 220-230 nm range, which is supposedly non-hazardous to humans [6,7].

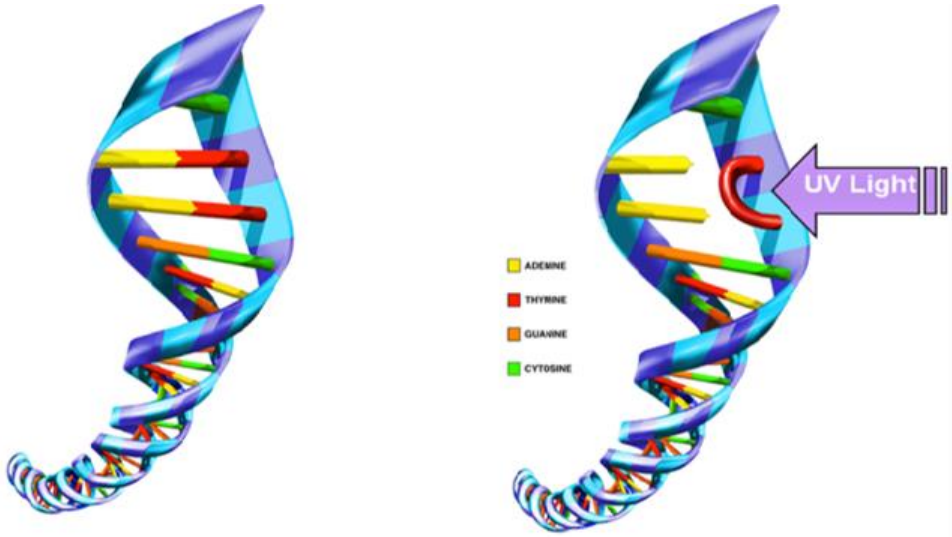

Figure 1. Response of pathogens to UV light. The DNA hydrogen bonds break and a new bond between the thymine groups form, preventing the microbes from reproducing (Retrieved from: https://www.researchgate.net/post/How_does_UV_light_prevent_the_growth_of_bacteria/5a29e59bdc332d76e0103747/citation/download).

1.2.2 Current technologies

Currently in the field of disinfection, the following types of lamps are being used and studied:

- **Low-pressure mercury lamp:** Historically, the most common type of lamp used to produce UVC radiation was the low-pressure mercury lamp, which has its main (>90%) emission at 253.7 nm. This type of lamp also produces other wavelengths. As an important drawback, mercury is known to be toxic to humans and to the environment.
- **Excimer lamp or Far-UVC lamp:** These types of lamps are based on excited dimers, with a peak emission of around 222 nm and are considered safe for usage around humans.
- **Pulsed xenon lamps:** These lamps, which emit a short pulse of broad spectrum (including UV, visible and infrared) light, and then filtered to emit mainly UVC radiation and are sometimes employed in hospital settings to treat environmental surfaces in operating rooms or other spaces. These are usually employed when no humans are occupying the space.
- **Light-emitting diodes (LEDs):** Light-emitting diodes (LEDs) that produce UV radiation are also becoming more commonly available. Typically, LEDs emit a very narrow wavelength band of radiation. One advantage of LEDs over low-pressure mercury lamps is that they contain no mercury. However, they pose multiple manufactural and efficiency related drawbacks that are yet to be solved.

Out of the lamps listed above, the most commonly used technique for GUV for disinfection are short-wavelength low-pressure mercury vapor tubes that emit at the resonance line of 253.7 nm. Despite being a low-cost, efficient method, it is also one that utilizes a toxic element with profuse amounts of side effects on human health and the environment. Mercury is used in a wide range of everyday products and is released into the atmosphere, soil and water from various sources. Hence, while we use it for water purification, we end up polluting the environment once it becomes waste.

Apart from their highly toxic nature, they also present efficiencies of 30%, which demands for a high operation voltage of up to 400 V. The device is somewhere between 2,000 up to 10,000 h. Also, they require a high warm-up period to reach full light output.

These devices and all mercury-based components are called to be forbidden. This is part of the Minamata Convention on the Mercury treaty signed by the United Nations and in place since August 2017 [8]. In the upcoming years, the extraction of mercury from mercury mines will slowly phase out and the need for environmental-friendly, efficient and more economical alternatives surge. In light of the high demand for more sustainable approaches, the development of low energy and economical devices that deliver high power efficiency is of utmost importance now. An immense amount of research centers and researchers are now brainstorming and investigating everyday on possible non-polluting, recyclable alternatives that can also be potentially miniaturized without a compromise on efficiency.

1.3 III-Nitrides for UV light emission

One group of materials intensely being studied for such UV disinfection devices are III-nitrides, particularly $Al_xGa_{1-x}N$ alloys. These materials present a direct band gap that can be tuned from 365 to 200 nm as a function of several parameters including the aluminum composition. Therefore, $Al_xGa_{1-x}N$ material is of huge interest in the UV research community and great progress has been made in the past years as far as light output power and device efficiency is concerned.

III-nitride materials are well known for their application in blue emitters and general lighting. The discoveries at the basis of the GaN blue LEDs have led to three Japanese researchers, namely, Professor Isamu Akasaki and Professor Hiroshi Amano from Nagoya University and Professor Shuji Nakamura from Nichia Corporation research center, win the Nobel prize in Physics in 2014. They were able to solve one of the major constraints while working with GaN materials, i.e. p-type doping being very difficult. Now, the efficiencies of blue LEDs can be as high as 90%. Industry giants including Nichia, LG, Panasonic, Philips, Osram, RIKEN, etc. have been publishing innovative advances in improving the efficiencies of nitride LEDs.

Since these advancements, ternary and quaternary nitride alloys have proven to be promising candidates for the production of LEDs emitting in the UV-A, UV-B, and UV-C wavelength regions. However, the efficiency of UV LEDs is much below that of their visible counterparts and their overall performance is still far below what is expected by the market. The power conversion efficiency and lifetime are to be improved if we wish to see industrial progress. Although highly efficient LEDs emitting at around 400 nm are commercially available [9], the efficiencies decrease as the wavelength moves deeper into the UV region. The challenges in doping layers with high Al contents and the difficulty in forming ohmic contacts due to the large band gap of the semiconductor material result in unreasonable operational voltages, and severe self-heating affects the lifetime of the devices [10]. Therefore, despite over 20 years of extensive research, the external quantum efficiency (EQE) of $Al_xGa_{1-x}N$ LEDs is still very low in the 255-265 nm wavelength range to be fully able to replace mercury lamps.

To be able to tackle the problems related to UV LEDs, a promising alternative to LEDs are electron beam pumped UV lamps. These lamps are based on utilizing the emission obtained from energetic electron injection in semiconductor materials. The generation of electron-hole pairs occurs through the mechanism of impact-ionization, i.e. when a high-energy electron collides with another electron in a bound state (i.e. in the valence band), part of the initial electron kinetic energy can be used to promote the second particle to an excited state within the conduction band, generating an electron-hole pair that can recombine radiatively. This is the premise of my research work and I focused my work on creating semiconductor structures apt for such devices.

1.4 Structure of the manuscript

This manuscript is organized in six chapters. Aside from this context chapter, chapters 2 and 3 are introductory, and chapters 4 and 5 present and discuss the experimental results. A last chapter draws conclusions and proposes perspectives for future studies.

Chapter 2 is a general introduction to the properties of III-nitride semiconductors, describing their crystal structure, structural and elastic properties to shed light on the electronic and optical performance. We make a particular emphasis on nanostructures such as the planar layers of self-assembled quantum dots (QDs) and QD systems in the self-assembling NW. In addition, we make an introduction to electron pumped UV lamps.

Chapter 3 tackles with the experimental techniques and the simulation methodology used in this thesis. We start with the process of epitaxial growth using plasma-assisted molecular beam epitaxy (PA-MBE). Then, we present the different characterization techniques used. In particular, we studied the morphology and structure of our samples using transmission electron microscopy (TEM), X-ray diffraction and atomic force microscopy (AFM), and the optical properties were evaluated by photoluminescence and cathodoluminescence techniques. Finally, this chapter provides details on the simulation methods used to model our samples.

Chapter 4 discusses the design and characterization of nitrogen polar $Al_xGa_{1-x}N/AlN$ ($0 \leq x$ 0.1) QD superlattices integrated along GaN NWs for application in pumped UV sources. A promising nanostructure with desirable properties for electron pumped UV lamps are nanowires. In this chapter, we first describe the growth conditions and the systematical evaluation of the optical performance of GaN/AlN superlattices on NWs for different thicknesses of dots/barriers and the effect of incorporating Al into the dots.

Chapter 5 describes the $Al_xGa_{1-x}N/AlN$ Stranski-Krastanov QD superlattices designed and synthesized for forming the active region of electron pumped UV emitters. Working with planar layers embedded with QDs potentially provides higher confinement resulting in better efficiencies and are more robust. We study two series of QD samples. The first series consist of QDs with x = 0 and x =0.1, studying the effect of the metal-to-nitrogen ratio during the deposition of the QDs. In the second series, we fix the metal-to-nitrogen ratio and increase the Al content in the QDs up to x = 0.8, to reach shorter wavelengths. In both series, we describe the structural characteristics and optical performance of these structures.

Chapter 6 summarizes the work accomplished and the main achievements of this PhD work. It also includes a beginning of future work for this project that has already been commenced by me with promising prospects.

2 Introduction

In this chapter, the key characteristics of III-nitride binary and ternary semiconductors will be covered in detail. The chapter explains the basic structural and elastic properties of III-nitrides and gives the state of the art of electron beam pumped UV lamps. The section that takes care of the electron beam pumped emitters is largely taken from our review paper: "**Electron beam pumped light emitting devices"** Cuesta S, Harikumar A and Monroy, E J. Phys. D: Appl. Phys (2022) [11].

2.1 III-Nitride semiconductors: background and concepts

III-V compound semiconductors are chemically formed by a third (3A) column element (B, Al, In, Ga) and a fifth (5A) column element (N, P, As) (see Figure 2). Out of these, III-nitride semiconductors (AlN, GaN and InN) have attracted a plethora of research for the past few decades because of the flexibility and promising attributes they exhibit for the design of light emitting devices. The range of the fundamental bandgap of III-nitride alloys ranges from the near infrared (NIR) for InN (around 1.9 µm, i.e. ~ 0.64 eV [12]) to the ultraviolet (UV) for AlN (200 nm, i.e. ~ 6.2 eV [13]). Therefore, the synthesis of III-nitride alloys and their bandgap engineering by also going towards low-dimensional nanostructures, such as quantum wells (QWs), nanowires (NWs) and quantum dots (QDs) would make it possible to fabricate devices along this large spectral range.

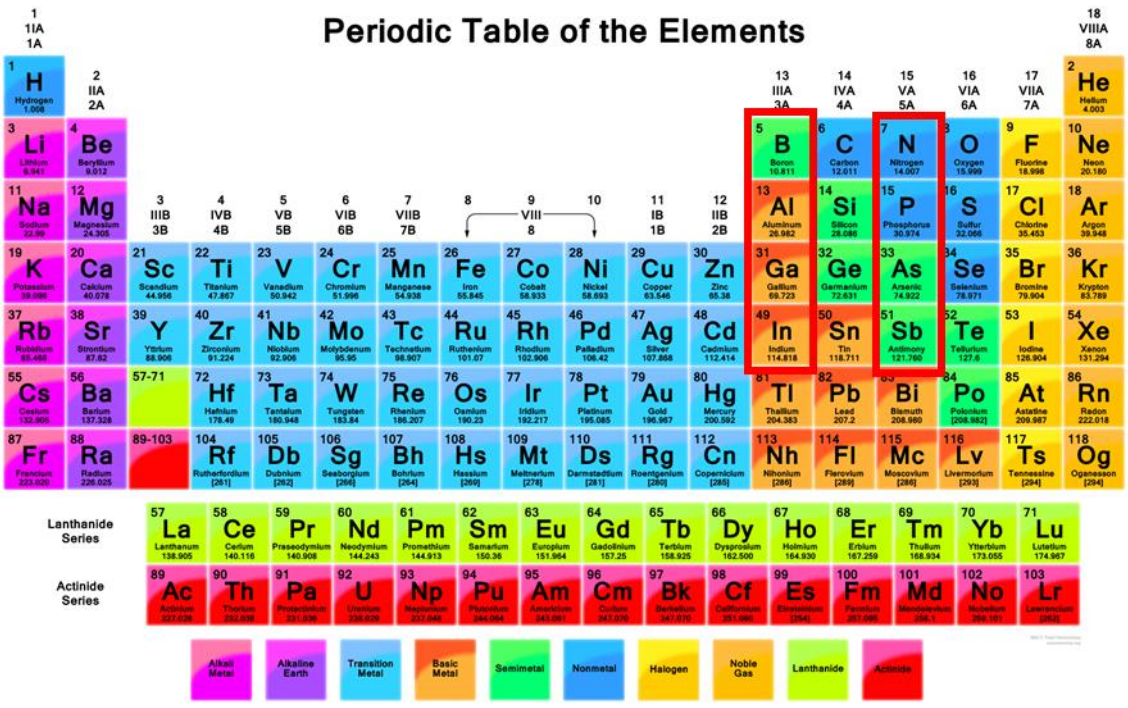

Figure 2. Periodic table of elements highlighting the 3rd and 5th column elements forming the III-V materials category (adapted from (Helmenstine 2017) [8]).

2.1.1 Crystal properties

III-Nitride semiconductors (AlN, InN and GaN) as well as their ternary alloys such as $Al_xGa_{1-x}N$ appear in three crystalline configurations, namely hexagonal wurtzite (α-phase), cubic zinc blende (β-phase) and cubic rock salt (γ-phase) structures.

The rock salt phase is the least common phase since it is the most unstable. This phase belongs to $Fm\bar{3}m$ space group and the unit cell is considered to be a face-centered (fcc) cubic lattice, shown in Figure 3. Rock salt phase requires very high pressures and temperature for growth and was not considered for this work.

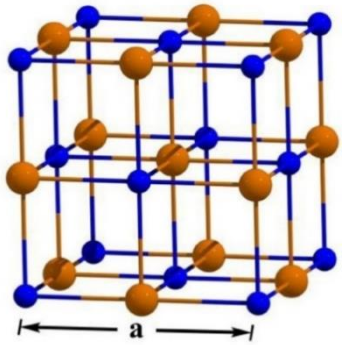

Figure 3. Crystal structure of Rocksalt III-N with of metal (yellow) and N (blue) atoms.

The cubic zinc-blende phase of III-nitrides is illustrated in Figure 4(a). This structure belongs to the $F\bar{4}_3m$ space group. It consists of two interpenetrating face-centered cubic sublattices shifted with respect to each other by ¼ [111]. As a result, this structure exhibits an ABCABC pattern, as shown in Figure 4(b), with the C-plane rotated by 60° with respect to A, in the [111] direction. Each metal atom is tetrahedrally connected to four nitrogen atoms, and A, B and C refer to Ga–N atomic bilayers. AlN, GaN, and InN have a tendency to crystallize in the wurtzite structure, but cubic zinc-blende growth can be achieved by controlling the growth parameters and using cubic substrates, such as (001) 3C-SiC or (001) GaAs [14].

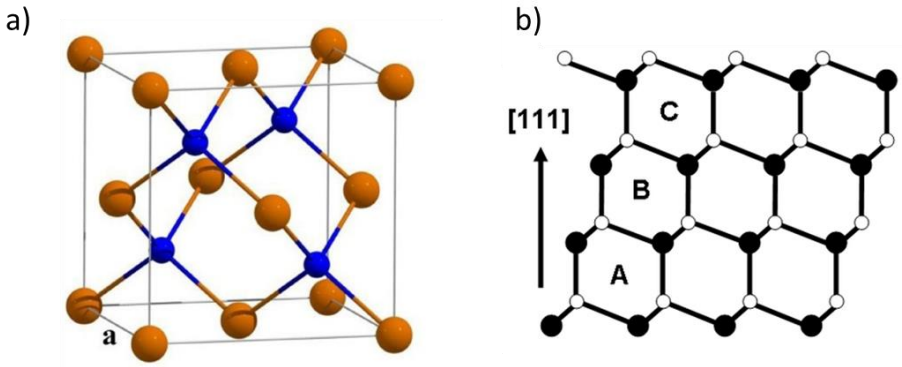

Figure 4. (a) Crystal structure of zinc-blende III-N with of metal (yellow) and N (blue) atoms. (b) The stacking sequence ABCABC of the close packed planes of metal (black) and N (white) atoms.

Hexagonal wurtzite (WZ) is the most thermodynamically stable crystal structure of GaN, AlN and InN. Wurtzite belongs to the space group $P6_3mc$ and point group 6 mm. The basal *c*-plane (0001) is the most commonly used crystal orientation, since it is easily grown on (0001) sapphire or (0001) SiC. As illustrated in Figure 5(a), the wurzite lattice is mainly defined by two parameters, the basal parameter a, which is the length of the edge of the hexagonal base and the axial parameter *c*, perpendicular to the basal plane, which is the height of the lattice. The structure consists of two hexagonal sublattices of metal (Al, Ga, In) and nitrogen (N) atoms which are shifted with respect to each other by $u = {}^{3}/_{8}$ [0001]. The atoms are arranged in an ABABAB stacking order (Figure 5(b)) where each metal atom is tetrahedrally connected to four nitrogen atoms, like in the case of cubic GaN.

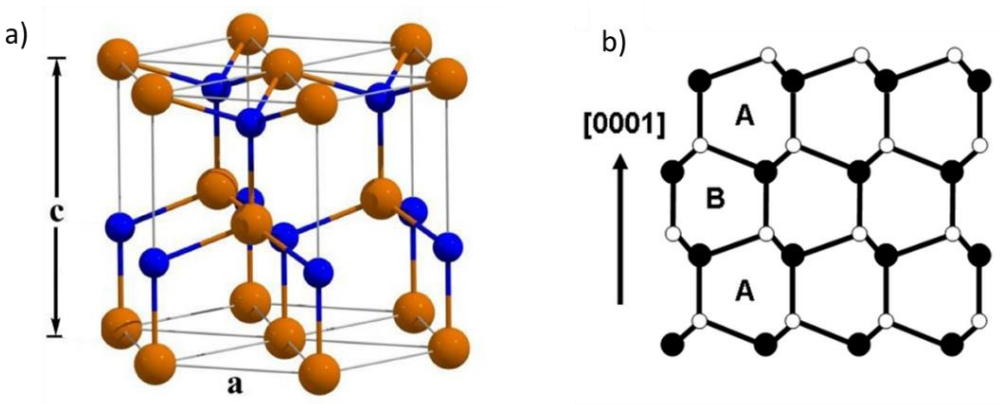

Figure 5. (a) Crystal structure of wurtzite III-N with of metal (yellow) and N (blue) atoms. (b) The stacking sequence ABABAB of the close packed planes of metal (black) and N (white) atoms.

In an ideal wurtzite crystal, the *c/a* and *u/c* ratios are 1.633 and 0.375, respectively. However, due to the difference in metal ions and the bond lengths, the resultant c/a ratios of AlN, GaN, and InN differ from each other. Table 1 summarizes the *a* and *c* parameters for GaN, AlN and InN at room temperature (300K) and atmospheric pressure.

Lattice parameters	GaN	AlN	InN
a (Å)	3.189	3.112	3.545
c (Å)	5.185	4.982	5.702
c/a	1.626	1.6	1.612

Table 1. Lattice parameters in GaN, AlN and InN materials [15,16].

From this point onwards, we will only consider the wurzite phase unless mentioned otherwise.

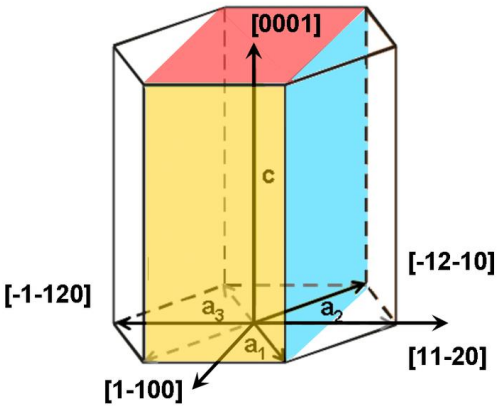

Figure 6. Wurzite hexagonal unit cell. The c-plane (0001), m-plane (1-100) and a-plane (11-20) are indicated in red, yellow and blue, respectively.

In a hexagonal system, the crystallographic directions and planes are named after the {h, k, i, l} Miller-Bravais indices. These are the projections in the basal cell of the prospective directions of the vectors { $\overrightarrow{a_1}$, $\overrightarrow{a_2}$, $\overrightarrow{a_3}$}, respectively. Since $\overrightarrow{a_1} = -(\overrightarrow{a_3} + \overrightarrow{a_2})$ the sum of the first three indices is zero: i = −(h + k). In the case of the hexagonal system, the [hkil] direction is perpendicular to the (hkil) plane only for some plane families. This is the case for those illustrated in Figure 6, which depicts the (0001) c-plane (red) along with the (1-100) m-plane (yellow) and the (11-20) a-plane (cyan).

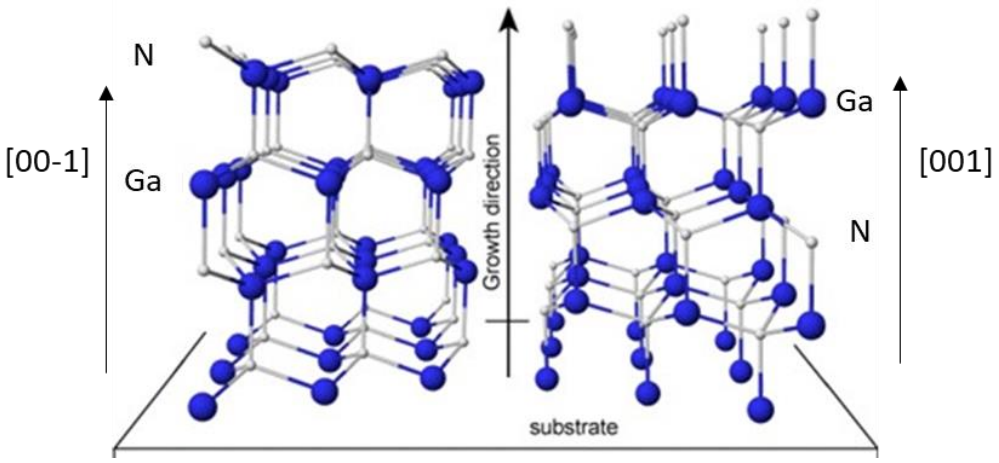

Figure 7. Crystal structure of GaN depicting N-polar (000-1) orientation (left) and N-polar (0001) orientation (right) [17].

Since the hexagonal lattice of wurzite III-nitrides is not centrosymmetric, this means the [0001] and [000-1] directions are not equal, see Figure 7. Considering the Ga-N bond that is perpendicular to the c-plane, then the vector pointing from Ga to N is said to be arbitrarily in the [0001] direction. If the material is grown along this direction, then it is called Ga-polar, and if it is grown in exactly the opposite direction, then it is called N-polar.

2.1.2 Band structure

By solving the Schrödinger equation of non-interacting electrons in a periodic lattice we get the band structure of a semiconductor. To visualize the band gap one must plot the energy vs. wave vector $k = (k_x, k_y, k_z)$. There are 4 symmetry points that occur in the first Brillouin zone labelled as Γ, Δ, Λ, Σ. Usually, the $E_n(k)$ band structure is plotted for values of k along lines connecting these symmetry points in the k-space. The band gap is defined as the energy difference between the lowest point of the conduction band and the highest point of the valence band. A direct band gap semiconductor is one in which these lowest and highest points of the conduction band and the valence band, respectively, occur at the same symmetry point, then the material is said to have a direct band gap.

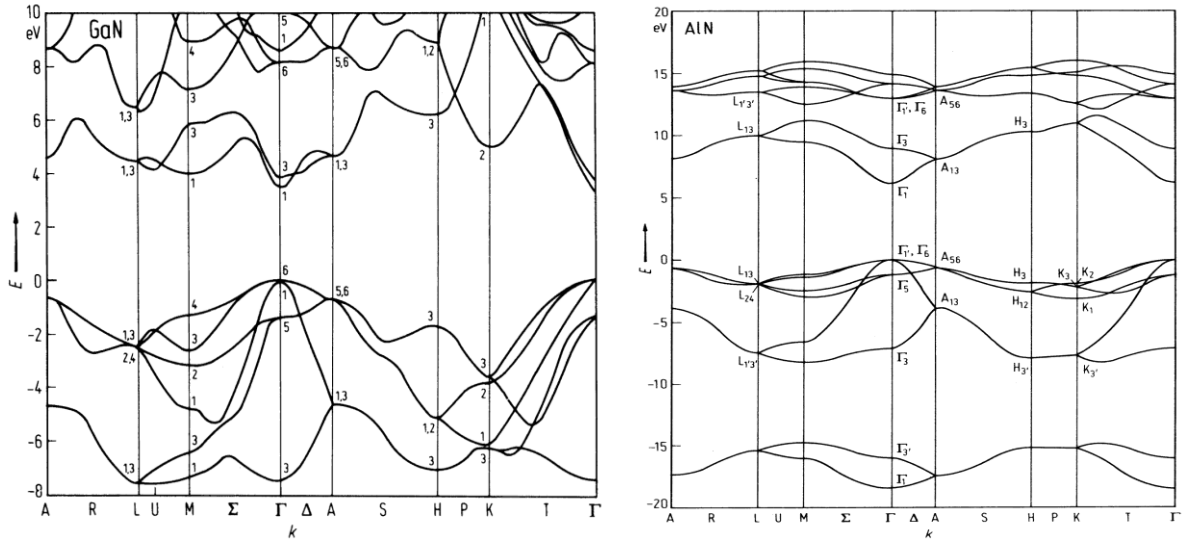

Figure 8. a) Band structure of wurtzite GaN in the 1st Brillouin zone. b) Band structure of wurtzite AlN in the 1st Brillouin zone [18].

III-Nitride semiconductors are direct band gap materials, meaning their optoelectronic properties are determined by the band structure near the center of the Brillouin zone at the Γ point where the wave vector $\vec{k} = \vec{0}$. Therefore, the minima of the conduction band and the maxima of the valence band both are in the Γ point, as is seen in Figure 8.

Due to the lack in symmetry for III-nitrides along c-axis and the spin-orbit interaction, we observe a degeneracy splitting of the valence band into three sub-bands, namely, the heavy hole (HH), light hole (LH) and spin-orbit (CH). Due to the crystal field splitting, the energy order of the three valence sub-bands is different for AlN and GaN. As illustrated in Figure 9, for GaN, the highest sub-band is the HH, followed by the LH, then CH band. Due to this, CH energy has a positive value of 22 meV [19] and the HH band is the top-most valence band. Since the HH subband is in the orbital state perpendicular to the c-axis, photons exhibit a maximum luminescence intensity for TE polarized light for GaN [20], meaning luminescence is stronger along the c-axis <0001> direction. Whereas for AlN, the CH is the top-most sub-band, followed by HH and LH [20]. Therefore, the CH energy has a negative value of -165 meV and the CH subband is the top-most band valence band. Since, CH is of the orbital state parallel to the c-axis, photons exhibit a maximum luminescence intensity for TM polarized light for AlN [21], i.e. strong parallel to the c-plane and weak perpendicular to it. The effective masses for GaN and AlN are listed in Table 2.

Assuming a parabolic structure at $\vec{k} = \vec{0}$, we use the effective mass approximation to explain the band structure. This would mean that the electron and hole behavior can be modelled as a free particle with a fixed potential having an effective mass m*. The optical properties of GaN are not well understood even now, due to which, in literature, there is a large dispersion of values of hole effective masses[22]. Some of the typical values at room temperature (T=300 K) for electrons (e) and heavy-holes (hh) in GaN and AlN are listed in the Table 2.

	GaN	AlN
m_e^*	$0.2m_0$ [15]	$0.32m_0$ [23]
m_h^*	0.3-2.2m_0 [24], [25], [26], [13], [22]	$1.44m_0$ [27]

Table 2. Effective masses for electrons (e) and heavy-holes (hh) in units of the free electron mass m_0.

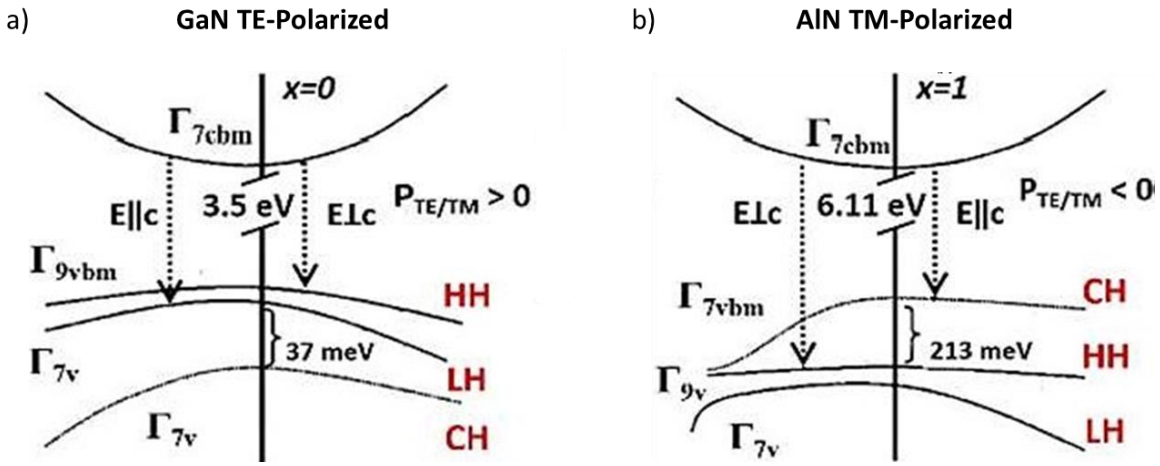

Figure 9. a) Schematic of the band structure of TE polarized WZ GaN at the Γ point. b) Schematic of the band structure of TM polarized WZ AlN at the Γ point (Adapted from Khee Ng et al. [28]).

The bandgap of ternary compounds like AlGaN is approximated by the following quadratic equation:

$$E_{\mathrm{G(AB)}} = \mathrm{x}E_{\mathrm{G(A)}} + (1 - \mathrm{x})E_{\mathrm{G(B)}} - \mathrm{x}(1 - \mathrm{x})\mathrm{b} \quad (2.1)$$

Here, b is the bowing parameter which takes into account the deviation from a linear interpolation between the two binaries A and B having an alloy mole fraction x. For the alloy AlGaN, the bowing parameter is reported to be 0.8-1.3 eV [29].

The value of the band gap is influenced by the temperature through the thermal expansion coefficient of the crystal lattice or from the electron lattice interactions, which is calculated by the Varshni equation:

$$E_{g(\mathrm{T})} = E_{g(\mathrm{T=0\ K})} - \frac{\alpha_V \mathrm{T}^2}{\beta_D \mathrm{D} + \mathrm{T}} \quad (2.2)$$

where α_V and β_D are the Varshni and Debye coefficients, respectively, the values of which are listed in Table 3 for GaN and AlN.

	GaN	AlN
$E_{g(\mathrm{T=0\ K})}$	3.507	6.23
$\alpha_V\ (meV/K)$	0.909	1.999
$\beta_D\ (meV)$	830	1429

Table 3. Bandgap at T=0 K and Varshni and Debye coefficients for GaN and AlN [15].

2.1.3 Elastic properties

Due to the lattice mismatch between the material and the substrate, as well as the difference in the thermal expansion coefficients, a strain is induced during the epitaxial growth. This strain directly impacts the bandgap, optical and electronic properties of the III-nitride material.

In the regime of linear elasticity, we can equate the relation between the stress (σ_{ij}) applied to a material and the strain ($\varepsilon_{\mathrm{kl}}$) with Hooke's law:

$$\sigma_{\mathrm{ij}} = \sum_{\mathrm{kl}} \mathrm{C}_{\mathrm{ijkl}}\varepsilon_{\mathrm{kl}} \quad (2.3)$$

where $\mathrm{C}_{\mathrm{ijkl}}$ is the fourth-order elastic tensor.

To better understand the notation, especially that of the fourth order elastic tensor, we introduce the indices {1, 2, 3, 4, 5, 6}, which now replace the pairs of indices {xx, yy, zz, yz, zx, xy}, respectively. For the strain it is as follows:

$$\varepsilon_1 = \varepsilon_{xx}\ ;\ \varepsilon_2 = \varepsilon_{yy}\ ;\ \varepsilon_3 = \varepsilon_{zz} \quad (2.4)$$

$$\varepsilon_4 = \varepsilon_{yz} + \varepsilon_{zy}\ ;\ \varepsilon_5 = \varepsilon_{zx} + \varepsilon_{xz}\ ;\ \varepsilon_6 = \varepsilon_{xy} + \varepsilon_{yx} \quad (2.5)$$

Similarly, for the stress, we consider:

$$\sigma_1 = \sigma_{xx}\ ;\ \sigma_2 = \sigma_{yy}\ ;\ \sigma_3 = \sigma_{zz} \quad (2.6)$$

$$\sigma_4 = \sigma_{yz} + \sigma_{zy}\ ;\ \sigma_5 = \sigma_{zx} + \sigma_{xz}\ ;\ \sigma_6 = \sigma_{xy} + \sigma_{yx} \quad (2.7)$$

Considering a hexagonal symmetry, the six elastic modules of a second-order elastic tensor can be represented by a 6x6 stiffness Voigt or matrix. Five out of these six elastic modules are independent

and $C_{66} = \frac{1}{2}(C_{11} - C_{12})$, as illustrated in Equation 2.7:

$$\begin{pmatrix}\sigma_1\\ \sigma_2\\ \sigma_3\\ \sigma_4\\ \sigma_5\\ \sigma_6\end{pmatrix} = \begin{pmatrix}C_{11} & C_{12} & C_{13} & 0 & 0 & 0\\ C_{12} & C_{11} & C_{13} & 0 & 0 & 0\\ C_{13} & C_{13} & C_{33} & 0 & 0 & 0\\ 0 & 0 & 0 & C_{44} & 0 & 0\\ 0 & 0 & 0 & 0 & C_{44} & 0\\ 0 & 0 & 0 & 0 & 0 & \frac{1}{2}(C_{11} - C_{12})\end{pmatrix}\begin{pmatrix}\varepsilon_1\\ \varepsilon_2\\ \varepsilon_3\\ \varepsilon_4\\ \varepsilon_5\\ \varepsilon_6\end{pmatrix} \quad (2.8)$$

One can determine the elastic stiffness constants by performing Brillouin or Raman scattering. However, most of the times, there still exist discrepancies between the experimental and calculated data due to the issues faced during the growth of high quality crystals. As a comparison, I have summarized below the theoretical and experimental values of the C_{ij} parameters for III-nitrides:

	C_{11}	C_{12}	C_{13}	C_{33}	C_{44}	References
GaN	374	106	70	379	101	[30] Exp.
	390	145	106	398	105	[31] Exp.
	396	144	100	392	91	[32] Theo.
	367	135	103	405	95	[33] Theo.
AlN	411	149	99	389	125	[34] Exp.
	410	140	100	390	120	[35] Exp.
	398	140	127	382	96	[32] Theo.
	396	137	108	373	116	[33] Theo.

Table 4 Experimental (Exp.) and theoretical (Theo.) stiffness constants of GaN and AlN.

Using Hooke's law (Eq. 2.3), it is possible to calculate the strain induced in the layer by looking at the stress distribution. During the epitaxial growth of III-nitride thin films on the (0001) plane, the in-plane stress is known to be uniform (meaning, $\sigma_{11} = \sigma_{22} = \sigma$) and there is no stress or sheer stress along the <0001> direction (biaxial stress configuration). For this particular case, and in absence of plastic relaxation, the Hooke law can be simplified as the following, with the coefficients given in Equations 2.10 and 2.11:

$$\begin{pmatrix}\sigma\\ \sigma\\ 0\end{pmatrix} = \begin{pmatrix}C_{11} & C_{12} & C_{13}\\ C_{12} & C_{11} & C_{13}\\ C_{13} & C_{13} & C_{33}\end{pmatrix}\begin{pmatrix}\varepsilon_1\\ \varepsilon_2\\ \varepsilon_3\end{pmatrix} \quad (2.9)$$

$$\varepsilon_1 = \varepsilon_2 = \varepsilon_{xx} = \frac{a_s - a_0}{a_0} \quad (2.10)$$

$$\varepsilon_3 = \varepsilon_{zz} = 2\frac{C_{13}}{C_{33}}\varepsilon_{xx} \quad (2.11)$$

where a_s and c_s are the lattice parameters of the substrate and on which the thin films are grown and a_0 is the bulk (relaxed) lattice parameter of the strained layer.

2.1.4 Spontaneous and piezoelectric polarization

A crystal is said to possess a spontaneous polarization ($\vec{P}_{sp}$) if the centers of the positive and negative charges in the crystal structure do not coincide naturally. One of the prominent properties of III-nitrides is the spontaneous polarization that exists due to the asymmetry in their hexagonal

wurtzite crystals. This is the result of nitrogen atoms being more electronegative than the metal atoms. The III-N bonds act as electrostatic dipoles, and the charge distribution does not cancel out along the [0001] direction unlike their cubic counterparts. The values of spontaneous polarization for III-nitride materials are listed in Table 5.

	GaN	AlN	Ref.
P_{sp} (C/m^2)	-0.029	-0.081	[36]
P_{sp} (C/m^2)	-0.032	-0.100	[37]

Table 5. The values of spontaneous polarization for GaN and AlN.

On the application of external stress on to the III-nitride crystal lattice, the lattice parameters c and a change. Thus, the polarization strength changes and this additional polarization in strained crystals is known as piezoelectric polarization ($\vec{P}_{pz}$). The total polarization in a crystal is calculated as the vector sum of the two polarization components (mentioned above) and can be represented as:

$$\vec{P} = \vec{P}_{sp} + \vec{P}_{pz} \tag{2.12}$$

Now, the piezoelectric tensor $\vec{P}_{pz}$ has three independent components for hexagonal crystals. Two of these components are involved in the piezoelectric polarization induced along the c axis or in the basal plane. The calculation of $\vec{P}_{pz}$ for wurtzite III-nitrides grown along the c axis is done with the following equation [38]:

$$P_{pz} = \mathrm{e}_{33}\varepsilon_{zz} + 2\mathrm{e}_{31}\varepsilon_{xx} \tag{2.13}$$

where e_{ij} are the piezoelectric coefficients of the material. Now, using equation 2.11 in equation 2.13, the amount of the piezoelectric polarization in the direction of the c axis can be represented as:

$$P_{pz} = 2\left(e_{31} + e_{33}\frac{C_{13}}{C_{33}}\right)\varepsilon_{xx} \tag{2.14}$$

The piezoelectric coefficients for AlN and GaN are listed in Table 6:

	GaN	AlN
e_{33} (C/m^2)	0.73	1.46
e_{31} (C/m^2)	-0.49	-0.60

Table 6. Piezoelectric coefficients for AlN and GaN [36].

2.2 Electron beam pumped lamps

2.2.1 Introduction and motivation

LEDs based on AlGaN semiconductors have long been pushed as a replacement for mercury lamps at 260-270 nm [39], as they are non-toxic, their emission is spectrally tunable to more efficient disinfection wavelengths, and they exhibit long lifetime and fast switching capabilities. However, despite there being a plethora of research in III–V LEDs, their performance is still not at the level of mercury arc lamps. Laboratories report record LED EQEs close to 20% at 275 nm [40], yet commercial devices exhibit efficiencies lower than 1%. This limited performance is attributed to drawbacks such as lack of UV transparent AlN substrates, low light extraction efficiency, low conductivity of the doped

regions (particularly in the p-type layers) and high resistivity of the contacts. These issues become more severe at shorter wavelengths. LEDs emitting at 222 nm are not commercially available and their EQE in the laboratory is below 0.1% [39].

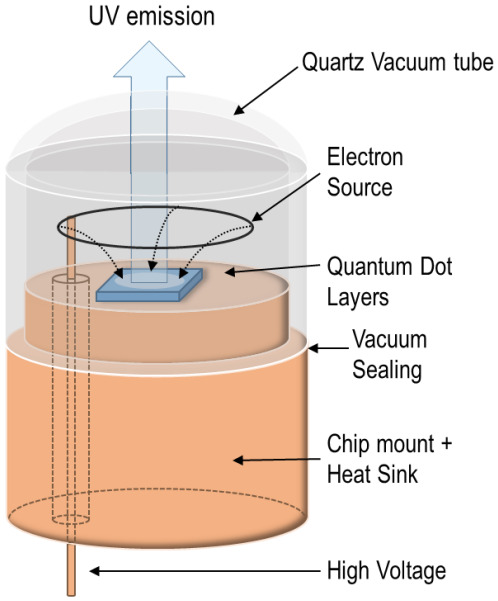

Figure 10. Typical structure of an electron beam pumped emitter containing Vacuum tube with a cold cathode (e.g. a CNT grid) for electron injection in the active semiconductor grid.

Electron beam pumped lamps are an alternative under consideration [39,41–43], as they can potentially solve the existing obstacles for obtaining efficient semiconductor-based UV emitters. The active materials of an electron beam pumped UV lamp do not require p-type doping, and there is no need of an electron blocking layer to compensate for the asymmetry in the transport properties of electrons and holes [39]. Due to these advantages, electron pumped UV lamps have the potential to perform beyond current state-of-the-art of UV emitters in terms of energy consumption, emission power, cost and recyclability.

2.2.2 Working principle

A typical structure of an electron beam pumped emitter is displayed in Figure 11. These electron beam pumped devices consist of a vacuum tube that contains the cathode, which serves as the electron gun, and the anode, which is the cathodoluminescent element. Electrons are accelerated from the cathode to the anode by an acceleration voltage, V_A. These high-energy electrons generate electron-hole pairs in the anode by impact-ionization, and photons are emitted as a result of the electron-hole pair recombination. With proper design and mounting schemes, one can prevent heating and possible hazards from soft x-ray generation.

In electron beam pumped lamps, the semiconductor geometry must be adapted to maximize the energy conversion, keeping in mind the penetration depth of the electron beam, R_e. Incident electrons will lose energy during the penetration due to scattering with valence and core electrons. A first empirical approach to estimate R_e is [44]:

$$R_e = \frac{4.28 \times 10^{-6}}{\rho} V_A^{1.75} \tag{2.15}$$

where ρ is the material density (in g/cm^3) and V_A is the acceleration voltage (in kV). This simple expression was improved by Everhart and Hoff [45], who delivered more accurate equations leading to the Monte Carlo simulations used nowadays. Figure 11 presents Monte Carlo simulations on the trajectory of the electrons injected in GaN (ρ = 6.15 g/cm^3) and AlN (ρ = 3.23 g/cm^3), for various values of V_a. The results illustrate the effect of voltage and material density.

Therefore, a key factor for maximizing the conversion energy is engineering an active region that overlaps with the expected electron trajectories.

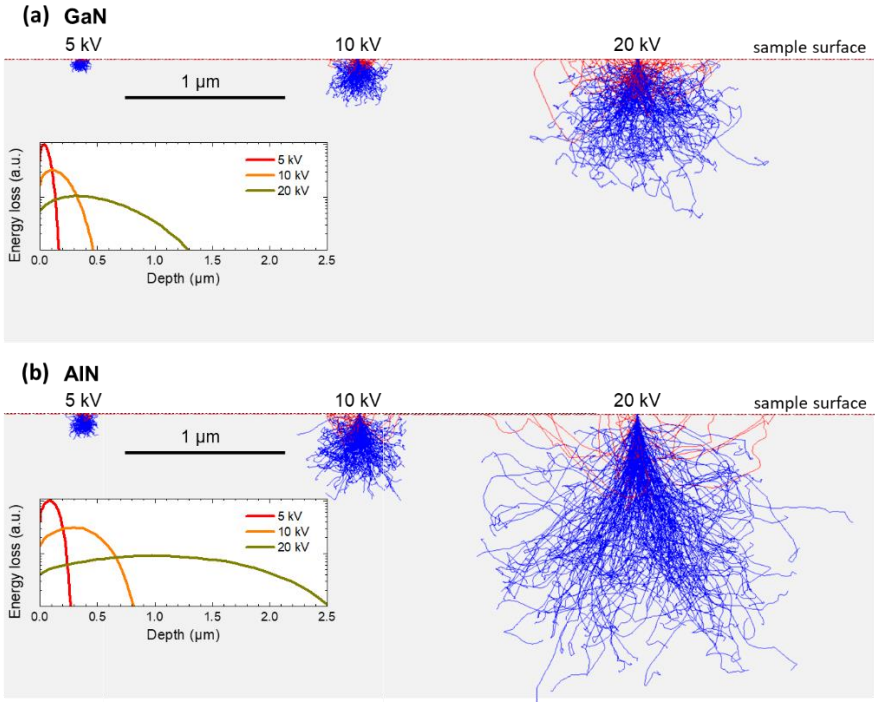

Figure 11. Monte Carlo simulations of the electron trajectory in (a) GaN and (b) AlN for Va = 5 kV, 10 kV and 20 kV. The trajectories of absorbed electrons appear in blue and those of backscattered electrons are depicted in red. The inset plots represent the electron energy loss, i.e. the distribution of the cathodoluminescence (CL) emission intensity, as a function of the penetration depth in both materials (cite review paper)

2.2.3 Efficiency

The performance of a light emitting device is characterized by its external quantum efficiency (EQE) or wall-plug efficiency (WPE). The EQE is the ratio of the number of photons emitted externally from the LED to the number of electrons passing through the device. The carrier injection efficiency (η_{inj}) is defined as the ratio of the number electron hole pairs recombining within the active region over the number of carriers injected into the device and the light extraction efficiency (η_{ext}) is the ratio of exiting photons from the device with respect to the photons created in the active region coming from radiative recombination. The EQE depends on η_{rad}, η_{inj}, η_{ext} by the following relation:

$$EQE = \eta_{rad} \cdot \eta_{inj} \cdot \eta_{ext} = IQE \cdot \eta_{ext} \quad (2.16)$$

The EQE is probably one of the most important parameters when talking about light emitting devices because it takes into account the influence of the optical efficiency as well as of electrical efficiency.

For LEDs, the internal quantum efficiency or radiative efficiency of a device, IQE is the efficiency of converting carrier current to photons. So, it can be defined as the product of the radiative

recombination efficiency, η_{rad}, and the carrier injection efficiency, η_{inj}.

$$IQE = \eta_{rad} \cdot \eta_{inj} \tag{2.17}$$

In a light emitting device, the radiative and non-radiative recombination processes take place hand in hand. So, higher radiative recombinations rates over non-radiative implies a better IQE. The carrier lifetime is an important characteristic of the active region and must be studied when manipulating the IQE of a device. A low radiative lifetime is necessary to yield a high IQE. The improvement of IQE can be attained by a good material quality limiting non-radiative recombination centers or traps, such as point defects or threading dislocations [46].

The wall plug efficiency, or sometimes also known as the power efficiency, is the ratio of the radiant flux (i.e. the total radiometric optical output power of the device, measured in watts) and the electrical input power, i.e. the efficiency of converting electrical to optical power:

$$WPE = \frac{P_{out}}{I \cdot V} \tag{2.18}$$

where P_{out}, I, and V represent the optical output power, operating current, and operating voltage of the lamp, respectively.

Ideally, the bias applied on an LED is approximately equal to the band gap energy. Therefore, in a promising device, the WPE should be approximately equal to the EQE. So, WPE and EQE are related through the following equation [39,47]:

$$WPE = EQE\frac{\hbar\omega}{e \cdot V} = EQE \cdot \eta_{el} \tag{2.19}$$

where $\hbar\omega$ is the emitted photon energy, and η_{el} the electrical efficiency, which is the ratio of the mean energy of the photons emitted and the total energy that an electron acquires from the power source.

When considering cathodoluminescent lamps, the above definition changes, in that, η_{el} is now defined as the ratio between the energy of the emitted photon and the energy required to create an electron-hole pair and it depends on the band gap energy, E_G of the semiconductor. So, the WPE is now related to the EQE in the following way:

$$WPE = EQE\frac{\hbar\omega}{\beta E_G} \tag{2.20}$$

where β is a material-dependent coefficient associated defined as the ratio between the average energy required to create one electron-hole pair and the band gap energy. Generally β is assumed to be ≈ 3 [44], meaning the WPE cannot exceed 33% of the EQE. Note that $\beta \approx 3$ is reported for direct-band-gap materials where the effective masses of electron (m_e) and hole (m_h) are approximately equal, whereas theoretical calculations predict lower values $\beta \approx$ 1.5-2 in wide band gap materials with $m_h > m_e$ [48,49].

2.2.4 State of the art

Electron beam pumped UV lamps have been demonstrated using various anode materials. In 2009, Watanabe et al. (Tsukuba University and Futaba Corporation) successfully managed to fabricate a handheld UV lamp equipped with a field-emission array, and delivering stable UV output power of 0.2 mW at 225 nm with an acceleration voltage of V_a = 8 kV. The anode material was highly purified

hexagonal BN (hBN) powder. Under extreme conditions (V_a = 9 kV, 100 μA), a maximum output of 1 mW was achieved over several hours of operation. The EQE was estimated at 0.6%, still a record value at that wavelength [50]. Then, it was in 2017 Lee and Song (Korea Atomic Energy Research Institute and Kongju National University) reported a UV cathodoluminescent device emitting at ≈ 325 nm using *exfoliated* hBN, prepared by sonication and centrifugation of hBN powder in isopropyl alcohol [51].

Most of the research on electron beam pumped UV lamps is seen to be focused on the development of AlGaN-based anodes [41,42,52–58]. In 2010, Oto et al. first reported the application of electron beam pumping to AlGaN/AlN quantum wells, obtaining UV emission at ≈ 240 nm [41]. However, the values of efficiency reported in this paper are in contradiction with the theoretical expectations of the electron beam pumped mechanism. Then, in 2011, Shimahara et al. demonstrated a UV lamp emitting at 247 nm, with an anode consisting of a Si-doped AlGaN film grown on an AlN-on-sapphire template [52]. A maximum output power of 2.2 mW was obtained for 100 μA at 10 kV, which corresponds to WPE = 0.22%. Immediately after, Matsumoto et al. reported the successful fabrication of a compact, handheld UV emission device through the integration of a highly efficient anode containing AlGaN/AlN quantum wells and graphene nanoneedles as field electron emitters [53]. The device exhibited an output power of 20 mW (7.5 kV/80 μA) and $WPE \approx$ 3.3%.

In 2015, Ivanov et al. [54] attained 4.7 mW output power at 270 nm with an anode consisting of $Al_{0.6}Ga_{0.4}N/Al_{0.7}Ga_{0.3}N$ multiple quantum wells (MQWs) with $IQE \approx$ 50%. In the continuous wave (cw) regime, the WPE of the structures was about 0.24%. In parallel, in 2016, Tabata-Vakili et al. [56] showed peak output power > 200 mW at 246 nm when pumping a sample consisting of ten $Al_{0.56}Ga_{0.44}N/Al_{0.9}Ga_{0.1}N$ (1.5 nm/40 nm) quantum wells with an acceleration voltage of 12 kV and a beam current of 4.4 mA (WPE = 0.43% for an estimated $IQE \approx$ 23%).

An interesting approach from the semiconductor viewpoint was developed by Ioffe Institute and partners, using extremely thin (1-3 atomic layers) GaN quantum wells. Thickness fluctuations in such quasi-two-dimensional GaN layers lead to strong exciton localization and high radiative efficiency. With this approach, they demonstrated structures delivering an output power of ≈160 mW (≈39 mW) in pulsed (cw) mode at 285 nm [55]. In this case, the anode material consisted of a 40-period $Al_{0.75}Ga_{0.25}N$/GaN (31 nm/≈1 ML) MQW. The maximum WPE was estimated at ≈ 0.86% (≈ 0.43%) in pulsed (cw) mode. Later, in 2018, Jmerik et al. reported electron beam pumped UV emission at a much shorter wavelength, 235 nm, from a sample consisting of 360 periods of GaN/AlN (1.5 ML/5.5 nm). The output power reached 150 mW (20 mW) in pulsed (cw) mode pumping at 20 kV/1 mA. This corresponds to WPE = 0.75% (0.14%) in pulsed (cw) mode [57]. Exploiting this approach of ultrathin GaN/AlN MQWs, this collaboration demonstrated UV light sources with a record output power of ≈ 2.2 W at 258 nm, with pulsed electron beam pumping at 18 kV/37 mA [42].

As an alternative to the use of III-N semiconductors, in 2016, Ichikawa et al. (Hamamatsu) reported a UV lamp based on an anode consisting of praseodymium-doped lutetium garnet aluminate (Pr:LuAG) synthesized by pulsed laser deposition on sapphire [59]. The peak emission obtained was at around 307 nm in response to the electron beam irradiation (10 kV/200 μA). They achieved an UV output power of 21.2 mW with WPE = 1.06%. Based on this work, an electron beam pumped UV light source using Pr:LuAG was commercialized by Hamamatsu. The product integrated a high-voltage power supply enabling 12 V input operation. It delivered a nominal output power of 10 mW with a life cycle of at least 10,000 h [59].

Oxide materials have also been considered as potential anode for UV lamps. In 2018, Yoo et al. (Kyung Hee University in Korea) demonstrated a UV emitter incorporating a carbon nanotube (CNT)

based cold-cathode (V_A = 7 kV, 0.3-0.5 mA) and an anode consisting of ZnO ink deposited on a quartz substrate and annealed at 1000°C, to form crystalline Zn_2SiO_4 [60]. They obtained deep UV emission peaking at 208, 226 and 244 nm. The same group demonstrated UV emission at 363 nm using SrB_4O_7:Eu as anode material, also with a CNT cold cathode [61]. Unfortunately, there was no information about emitted power or WPE.

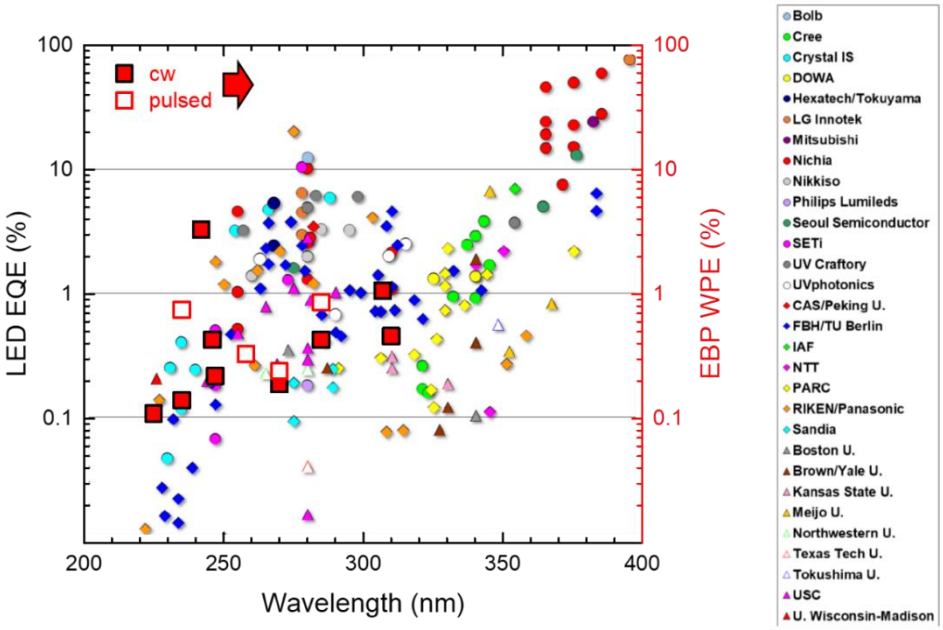

Figure 12. WPE of electron beam pumped (EBP) devices in the literature [32,40,42–47,52]] (plotted as larger red squares: solid red for those measured with continuous wave excitation and red outlined for those measured in pulsed mode) compared to the EQE of reported AlGaN-based LEDs. [The LED EQE data is reprinted from ref. [47]].

Material	λ (nm)	V_a(kV)	P_{max} (mW)	cw/pulsed	WPE (%)	Ref.
hBN	225	3-8	0.2	cw	0.11	[50]
exfoliated hBN	350	9	--	cw	--	[51]
$Al_{0.6}Ga_{0.4}N$/AlN QWs	240	8	100	cw	--	[41]
Si-doped AlGaN	247	10	2.2	cw	0.22	[52]
$Al_{0.7}Ga_{0.3}N$/AlN QWs	242	2-3	20	cw	3.3	[53]
$Al_{0.56}Ga_{0.44}N/Al_{0.9}Ga_{0.1}N$ QWs	246	12	200	cw	0.43	[56]
GaN/AlN QWs	235	20 15	150 28	pulsed cw	0.75 0.14	[57]
AlGaN/AlGaN QWs	270	16 20	60 4.7	pulsed cw	0.24 0.19	[54]
GaN/AlGaN QWs	285	15 15	150 39	pulsed cw	0.86 0.43	[55]
GaN/AlN QWs	258	18	2200	pulsed	0.33	[42]
Pr:LuAG	307	10	21.2	cw	1.06	[59]

Table 7 Summary of operation parameters of electron beam pumped UV lamps: operation wavelength (λ), acceleration voltage (V_A), maximum output power (P_{max}), cw or pulsed operation, and wall plug efficiency (WPE).

Finally, Ozol et al. [48] recently discussed the possibility to use various phosphors as cathodoluminescent elements for the fabrication of UV lamps. In their view, the most promising materials are based on $Li_2B_4O_7$ doped with Ag (emission around 270 nm) or Cu (around 365 nm).

As a summary, Figure 12 and Table 7 displays currently available WPE data from electron beam pumped UV emitters, compared to the EQE data of AlGaN-based LEDs in the literature [47]. To make a fair comparison, we must keep in mind that WPE and EQE are not equivalent. The best value of LED WPE reported in the 270-280 nm range is 5.7% [40], corresponding to an EQE = 20%. Let us recall, LEDs are bound by equation (2.17), i.e. $WPE = EQE \times \hbar\omega/(e \cdot V)$. In this spectral range, $\hbar\omega$ varies from 4.13 eV at 300 nm to 5.64 eV at 220 nm. Then, in UV LEDs, the operation voltage is relatively high due to the important access resistance. For LEDs emitting around 260 nm (≈ 4.77 eV), the operation voltage is in the range of 6 to 16 V, which means that $\hbar\omega/(e \cdot V)$ varies between 0.8 and 0.3. And the LED EQE plotted in Figure 12 should be multiplied by $\hbar\omega/(e \cdot V)$ to obtain the LED WPE. Keeping this difference in mind, the performance of electron beam pumped UV lamps is comparable to that of UV LEDs, in spite of a much reduced research available. It is important to note that most of the groups here worked on QW structures and going to the dots and wire regime, one can profit from higher confinement and end up with a more efficient devices. Also note, for instance, that none of the groups working on electron pumped UV lamps made particular effort to improve the light extraction efficiency or the device thermal dissipation. With all these considerations, the electron beam pumped technology looks very promising in terms of performance, particularly at short wavelengths, in the 220-240 nm spectral range.

An improvement in IQE of the anode is definitely beneficial for UV emitters. Hence, the use of two and three dimensional structures like nanowires and quantum dots where carrier confinement leads to an enhancement of the radiative efficiency at room temperature [43,62–65]. From the optical point of view, the nanowire shape also spontaneously favors light extraction. This is the clue that was explored in this doctoral work.

3 Experimental techniques and methods

In this chapter, I will explain the experimental and simulation techniques that were applied in this work. The text starts with the epitaxial growth process using plasma-assisted molecular-beam epitaxy, monitored with reflection high-energy electron diffraction as real-time *in-situ* characterization technique. Further, I will introduce various characterization techniques, namely, scanning electron microscopy, x-ray diffraction and atomic force microscopy for structural studies, and photoluminescence and cathodoluminescence techniques for optical measurements. Finally, I will talk about the simulation methods used to model my samples.

3.1 Epitaxial growth

When a crystalline material is deposited onto a crystalline substrate and the deposited crystal lattice is aligned with that of the substrate, the process is known as "*epitaxy*". Etymologically originating from Greek, "epitaxy" is translated to being "arranged upon" and this is exactly what happens during growth. Once on the surface of the substrate, the atoms propagate by surface diffusion until they reach a thermodynamically favorable location and make a bond with the substrate. Figure 13 illustrates the various processes that take place on the surface during epitaxial growth. These are namely adsorption, diffusion, nucleation, desorption, aggregation etc. Since the atoms require time for diffusion and settling on the surface, the quality of the film can degrade at high growth rates.

Epitaxy is divided into two kinds:

- Homoepitaxy: When the deposited material is grown on a substrate made of the same material, it is called homoepitaxy. This method is used when one requires a pure material or when a different doping level is desired.
- Heteroepitaxy: When the deposited material is grown on a substrate made of a different material, it is called heteroepitaxy. This method is used when the material is not available in its bulk form to be used as a substrate or when one needs to grow integrated crystal layers, called heterostructures.

In absence of mechanical strain (lattice-matched growth), and as a result of all surface processes taking place during epitaxial growth, the following growth modes can be obtained:

(a) Multi-layer growth: If the adatom diffusion length is short, the nucleation of clusters with formation of multiple layers is obtained, forming a rough surface.

(b) Layer-by-layer growth: If the diffusion length is long, it results in the nucleation of monolayer (ML) clusters, with the atomic layers completed one by one.

(c) Step-flow growth: When diffusion length is even longer, the longer diffusion length gives the adatoms enough mobility to reach the step edges, which are often energetically favorable incorporation sites.

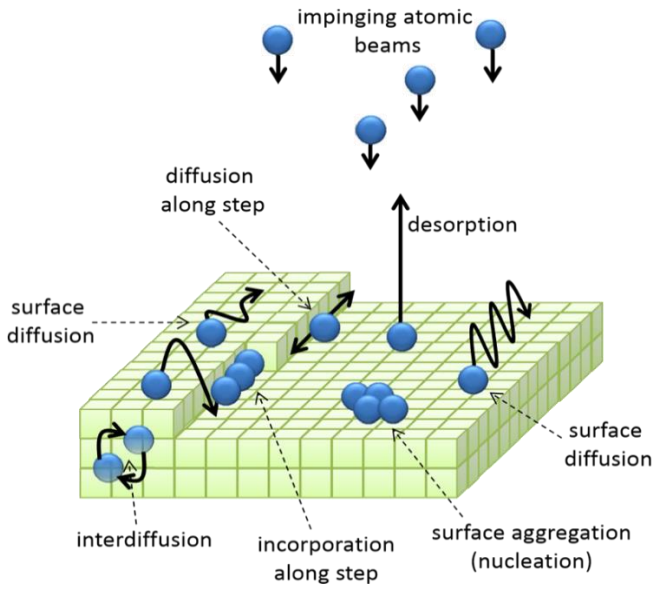

Figure 13. Illustration of the various processes occurring on the growth surface during epitaxial growth. Adsorption and surface diffusion of atoms, formation of crystalline lattice and desorption of particles from the surface [66].

In presence of mechanical strain (lattice-mismatched growth), and depending on the growth parameters, three growth methods are observed, as illustrated in Figure 14:

a) Layer or Franck-Van der Merwe growth mode (FM): This type of growth ensures that a new layer starts to grow only after the preceding one is complete, resulting in 2D growth. Note here that release of misfit strain could lead to dislocations.

b) Layer plus island or Stranski Krastanov growth mode (SK): This type is a combination of 2D layer and 3D growth mode. The islands grow after wetting of surface layer by layer until a critical thickness where the relaxation of strain happens. If growth is continued, it can result in the formation of misfit dislocations (SK-MD).

c) Island or Volmer-Weber growth mode (VW): In this type of growth, the deposited atoms cannot diffuse past the island boundaries due to large lattice mismatch. Due to the lack of wetting, multiple monolayers can be formed as high islands after light coverage.

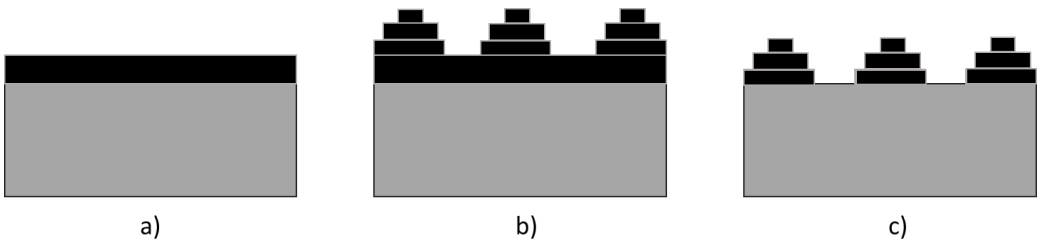

Figure 14. Various heteroepitaxy growth modes: a) Franck van der Merwe, b) Stranski-Krastanov, and c) Volmer-Weber.

It is reported that the formation of SK QDs in III-As system such as InAs/GaAs is a result of the large lattice mismatch ($\varepsilon=\Delta a/a\approx 7\%$) between the layers [67]. Although, in a II-VI system, which also has large lattice mismatch ($\varepsilon\approx 6\%$), no clear islands are reported [68]. On the other hand, the GaN/AlN system that despite having a lower lattice mismatch in comparison ($\varepsilon \approx 2.4\%$) is known to show a clear 2D-3D transition. Therefore, we can safely deduce that the growth mode depends not only on the

lattice mismatch between growth layer and the substrate but also on the growth conditions. Therefore, it is possible, for instance, to switch between FM and SK growth modes along the growth of a sample.

The growth mode is given by the process that grants the minimum free energy per unit area, which is represented as $E = E_{strained\ epilayer} + E_{surface}$, for a certain film thickness h (h > 1 monolayer (ML)). Henri Mariette [69] performed a detailed analysis on the equilibrium model by calculations based on the formation energies of SK, FM and MD and the critical SK thickness, h_c^{SK}, and the critical plastic thickness, h_c^{MD}. Figure 15 is the phase diagram showing the expected growth mode derived from the minimized formation energy as a function of the deposited thickness and the ratio between the two critical thicknesses η given by:

$$\eta = {h_c^{MD}}/{h_c^{SK}} \tag{2.21}$$

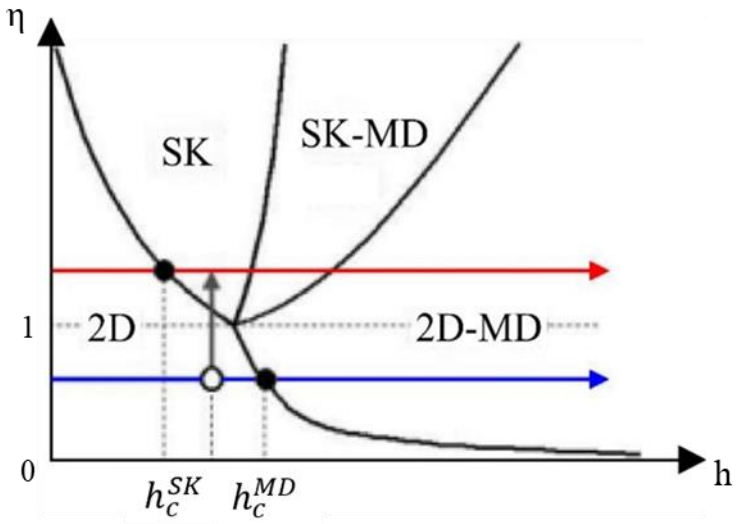

Figure 15. Phase diagram illustrating the expected growth mode as a function of the deposited thickness [69]

From this diagram, we can deduce that when we take, for example, η > 1 (red arrow), the strain will relax first by the formation of islands when attaining h_c^{SK}, and then misfit dislocations will appear at higher thicknesses. This is the situation when GaN is grown by MBE under N-rich conditions. On the contrary, η < 1 (blue arrow) implies $h_c^{MD} < h_c^{SK}$, and so the growth favors a plastic relaxation by formation of dislocations once the thickness reaches the critical thickness h_c^{MD}. This is the situation in the case of MBE growth of GaN under Ga-rich conditions. The gray arrow represents the effect of a growth interruption during Ga-rich growth: the change of surface energy when the Ga excess is evaporated results in a sudden increase of η, and SK islands can form in a layer that was originally 2D.

3.1.1 Description of PA-MBE growth technique

There are several growth techniques utilised for the growth of semiconductor materials, namely, liquid phase epitaxy (LPE), vapour phase epitaxy (VPE) and molecular beam epitaxy (MBE). The choice of the growth technique always comes down to a compromise between quality and cost of the final sample.

During the course of my PhD work, I worked with the MBE method for growth of my samples. MBE is one of the most advanced single crystal thin film deposition techniques, invented in the late

1960s at the Bell Telephone Laboratories by A. Y. Cho and J. R. Arthur [70]. In its most basic form, molecular beam epitaxy (MBE) is the process where a substrate is placed in ultra high vacuum (UHV) and the source materials for the film are evaporated from their elemental sources. The evaporated molecules or atoms travel as a plasma or beam, striking the substrate, where they then adsorb and nucleate on the surface. MBE was the first technique allowing the growth of perfectly abrupt superlattices.

The advantages of using MBE are manifold. First, the temperature requirement for growth with MBE is lower than that of VPE and we can achieve a relatively low growth rate (lower than 1 ML/s). This slow growth rate ensures a better quality crystal growth. In addition, MBE growth takes place in UHV (ultra high vacuum) environment, which provides the possibility to have in-situ control over the growth by utilizing techniques such as reflection high energy electron diffraction (RHEED) or quadrupole mass spectrometry. MBE growth processes are very reproducible which is a very important factor in research to enable the production of materials with critical demands of dimension, chemical composition, etc. Another reason that makes MBE superior is the fact that it can develop thin films in the out-of-equilibrium conditions. This allows room for constant experimentation opportunities and testing possibilities to be able to stabilize materials that do not exist spontaneously in nature and achieve structures with new material properties. MBE was the first technique allowing the growth of perfectly abrupt superlattices. However, the low growth rate, expensive growth processes and high cost of maintenance are still some of the drawbacks in terms of industrialization of the technique.

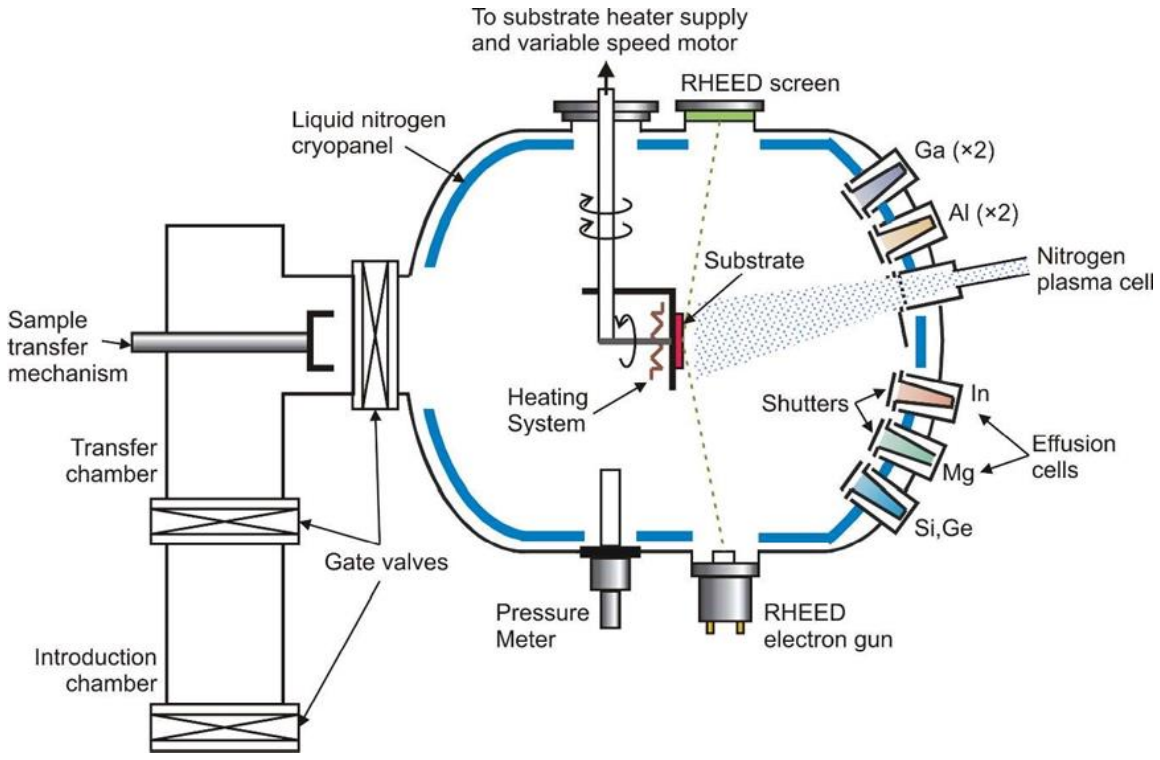

Figure 16. Schematics of the PAMBE used in this study (modified from[71]).

The structure of a typical MBE chamber is illustrated in Figure 16. The substrate is first cleaned chemically and secured on a molybdenum holder called MOLYBLOC, mechanically or with melted indium, which holds the substrate by surface tension. It is then ready to enter the MBE machine. There are three main blocks in the MBE, namely, the introduction chamber, transfer chamber and growth

chamber. The sample is first placed in the introduction chamber and then moved to the growth chamber via the sample exchange load lock. From there it is moved to the growth chamber where it is fixed on to a 4-axis manipulator, which allows automatic rotation and heating of the substrate. In order to load the samples, the introduction chamber is first opened and then evacuated down to 10^{-8} to 10^{-9} mbar. The transfer chamber is a transfer module permanently kept at a pressure of about 10^{-9} to 10^{-10} mbar. The growth takes place in the growth chamber, which is initially evacuated close to 10^{-11} mbar by a cryogenic pump combined with the cryogenic cooling down of the chamber walls with liquid nitrogen.

The nitrogen source is introduced by plasma dissociation of high purity N_2 (6N5) to create active nitrogen free radicals, in which case the technique will be known as plasma assisted MBE (PA-MBE). This terminology differentiates it from other sources of nitrogen like ammonia-based sources. Our MBE system is equipped with an automatic N plasma source HD25 supplied by Oxford Applied Research. The output power is varied to modify the flux of active nitrogen. In our case, the nitrogen flux was regulated through a mass flow at either 1 sccm with a radio frequency power of 250W corresponding to a growth rate of 0.25 ML/s. The growth of III-nitrides in this type of system occurs under a nitrogen pressure of about 5-9 × 10^{-6} mbar.

In Figure 16, we can see the various effusion cells, including Ga, Al, In, Si, Mg and Ge. The basic structure of an effusion cell is depicted in Figure 17. The molecular beams of Al, Ga, Si and Ge are generated from high-purity solid metals loaded in effusion cells, which consist of a crucible surrounded by heating coils. The Knudsen-type crucibles are made of pyrolytic boron nitride. By proportional-integral derivative controllers, accurate regulation of the cell temperatures is achieved. By raising up the temperature of the effusion cells, the sources are evaporated and a mechanical shutter in front of each cell is used to interrupt and control the flux flow (*i.e.* stop or start the doping and deposition).

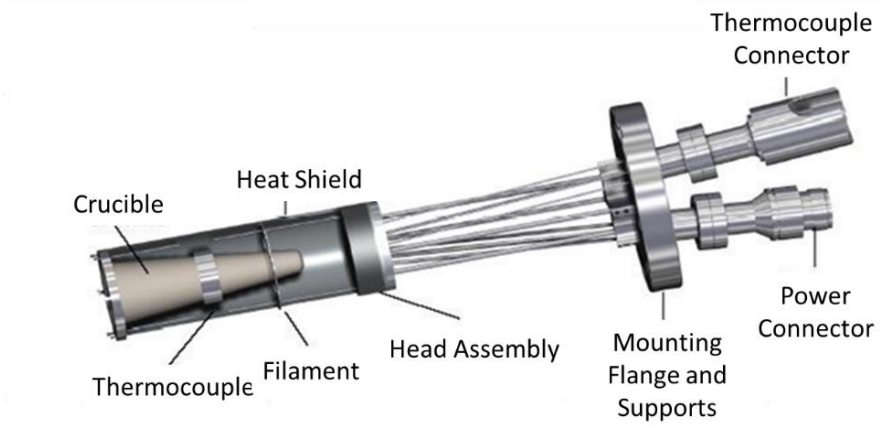

Figure 17. Schematics of an effusion cell.

The MBE growth chamber is kept at UHV and the walls are cooled down with liquid nitrogen. There are only two heat points in the chamber: effusion cells and the substrate, which is kept at a suitable growth temperature (around 720°C in our case). The evaporation rate is controlled by setting the cell temperature. The atoms then deposit and crystallize by reacting with the substrate. At this point, the crystal growth is not at thermodynamic equilibrium, meaning it is mostly governed by the kinetics of the surface processes, illustrated in Figure 13. As a result, the main growth parameters are the substrate temperature, the effusion cell temperatures, the nitrogen cell power and the nitrogen flow.

The MBE system contains an in-situ and real-time characterization tool, called RHEED, in order to monitor the growth by studying the morphology and crystal structure of the growing surface. Electrons are emitted from a gun (hot filament), excited by a 1.5 A current and under a high accelerating voltage (32 keV, in our case) towards a substrate, with a grazing incidence of the order of 2-3°. After interaction with the surface of the sample, the electrons form a diffraction pattern on a phosphorous screen mounted on the opposite side of the gun inside the chamber. These diffracted electrons correspond to the intersection of the surface electronic density Fourier transform with the Ewald sphere of radius $k_0 = \frac{2\pi}{\lambda}$, where λ is the wavelength of the electron, as shown in Figure 18 [66].

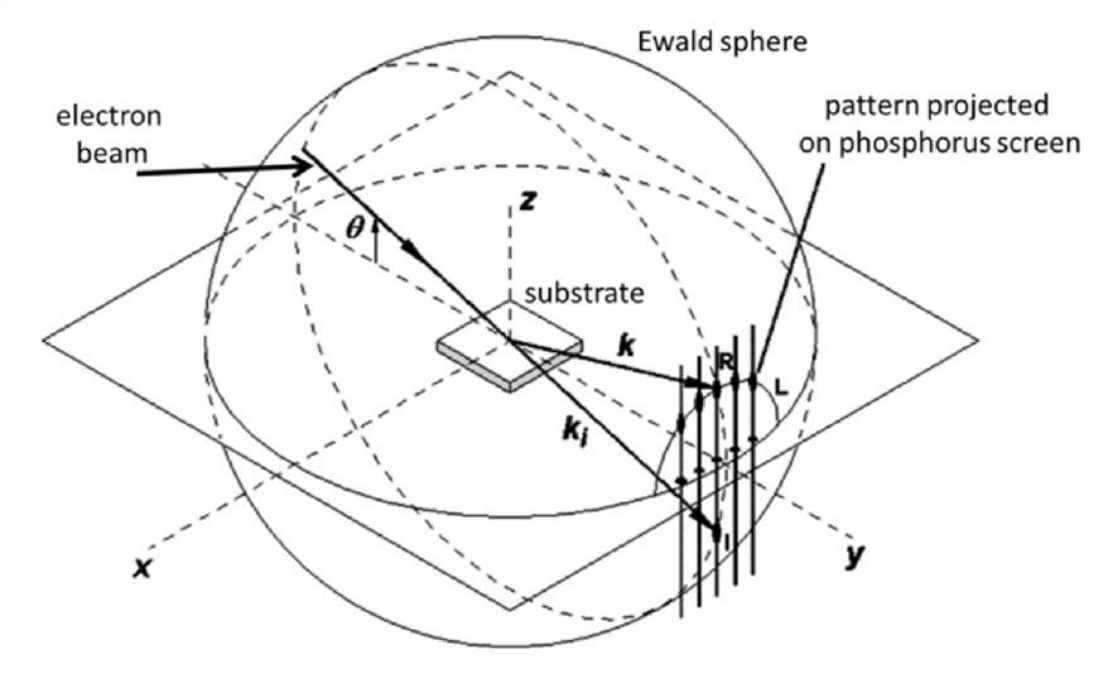

Figure 18. Ewald sphere and the RHEED principle [66].

The RHEED pattern is created by the interaction of the emitted electrons with the first atomic layer at the surface of the sample. These patterns, essentially, inform us about the crystallographic plane arrangements, flatness of the surface, sizes of grains/domains of surface structures, the epitaxial relationship between grown films and islands with respect to the substrate [72]. To better understand the diffraction patterns, various cases of surfaces and resulting patterns are represented in Figure 3.6. For an atomically smooth, ideal surface, the theoretical RHEED pattern should be constituted by infinitesimal spots aligned on a radial arc as perpendicular arcs [73]. Due to the non-idealities of the surface, in reality, and due to the fact that the beam is never perfectly monochromatic, the reciprocal lattice of an ideal surface tends to become streaks, as shown in Figure 19. Due to in-plane periodicities as a result of disorder in a polycrystal, the pattern is ring shaped: sign of a poor crystalline quality with varied orientations of the grains. If there are small steps on the surface or asperities on the sample, the diffraction pattern is constituted of spots. The same way, one can observe the growth of large "island" facets or 3D (e.g. QDs) with additional lines on the RHEED pattern. The "high" islands (e.g. NWs) introduce an out-of-plane periodicity, resulting in the lengthening of RHEED spots.

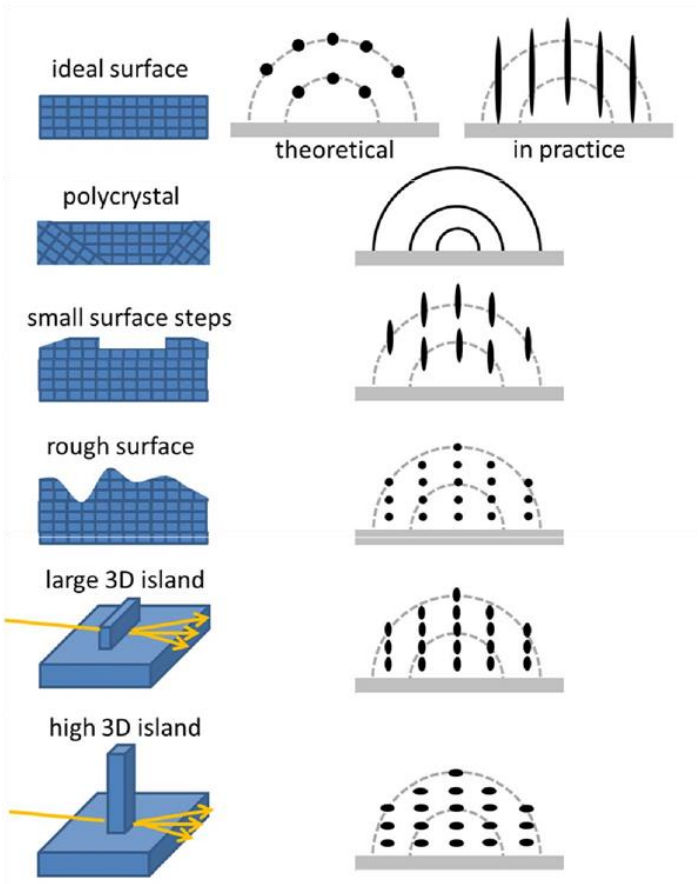

Figure 19. Typical surface morphologies and their respective RHEED patterns [66].

By studying the RHEED intensity, we are able to measure the growth rate under layer-by-layer growth conditions. During the growth, the density of atoms at the surface is time-dependent and gives an oscillatory variation of the RHEED intensity as a function of time. Considering a flat surface, the coverage of atoms on the surface can be termed as θ. When the layer is fully grown, the coverage is considered to be minimum (i.e. n^{th} layer, $\theta = 0$). Starting with this maximum coverage, we can explain the determination of growth rate as illustrated in Figure 20. For intermediate coverage, the intensity reduces with an increase in coverage up until $\theta = 0.5$. At this point, the roughness is at its maximum and the intensity is at its lowest. Taking the growth further would increase the coverage but decrease the roughness as shown in Figure 20. At $\theta = 0.75$, the intensity is recovered as the roughness is reduced as the growth continues to take up more adatoms. The surface flattens at $\theta = 1$, giving a maximum RHEED intensity again and the cycle of the process continues with further growth. Therefore, a single RHEED intensity oscillation period corresponds to a single layer growth. While operating the PAMBE system, the calibration of the growth rate and the control of the alloy composition and thickness of the layers were done by observing these RHEED oscillatory behaviors.

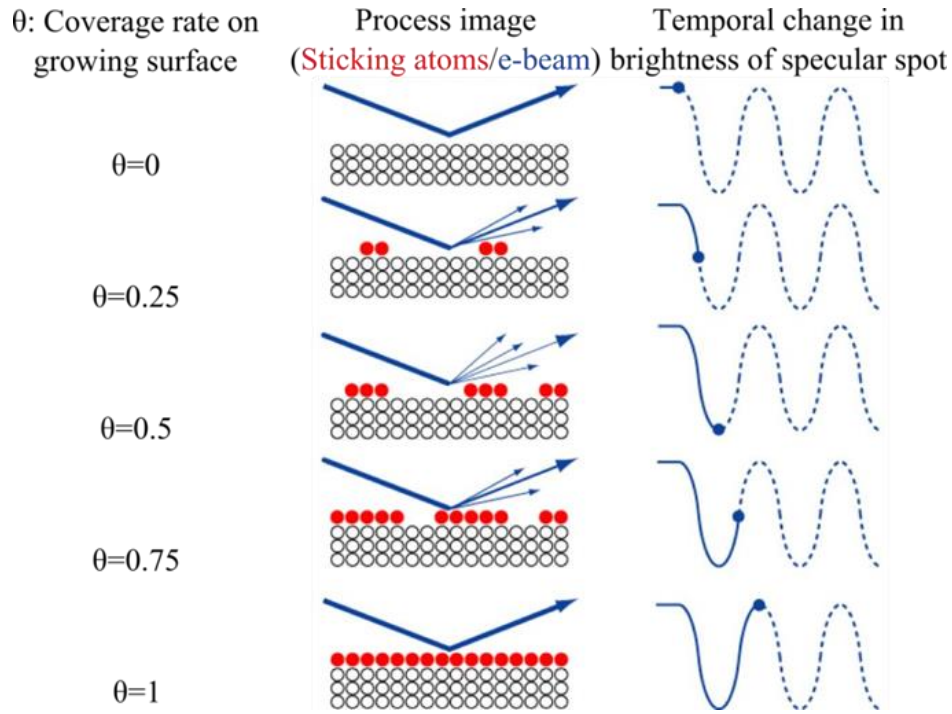

Figure 20. Schematic to describe the procedure to determine the growth rate by varying the RHEED intensity. The red dots correspond to the adatoms that form during the formation of the layer formation, the white dots correspond to the adatoms in deep layers, which are not reflected by the RHEED intensity, and the blue arrows represent the electron beam that hits the surface of the material (modified from [74].

3.2 Substrates

For the growth of AlN/AlGaN heterostructures, AlN substrates would be the more ideal choice. Bulk AlN exists in the market but it is expensive (> 3000 € per 2 inch wafer of non-transparent AlN grown by sublimation techniques). Furthermore, bulk substrates absorb ultraviolet light due to the presence of carbon impurities. Transparency can be achieved by compensation (e.g. attaining the adequate oxygen-to-carbon ratio), but compensated substrates are even more expensive (> 5000 € per 2 inch wafer) Therefore, growth is usually performed on foreign substrates.

The selection of substrate for III-N heteroepitaxy is be made by taking into account parameters such as lattice constant, thermal expansion coefficient, requirement of III-N epilayer orientation, defect density, purity etc. Possible choices of substrate for the growth of III-N are usually sapphire-based, Si(111)-based or SiC-based substrates. In this work we used two types of substrates depending on the desired heterostructure: AlN-on-sapphire templates for QDs and silicon substrates for NWs. The substrates are cleaned chemically with organics (trichloromethane, acetone and methanol) and sonicated to remove surface grease, dirt etc. Later, it is baked for 30 minutes in the growth chamber to further remove surface hydrocarbon molecules. A thin AlN layer is grown before starting the growth of the quantum dots. Growing this AlN buffer layer prior to GaN nucleation on the substrate is known to decrease defects density and increase surface smoothness.

3.2.1 Sapphire-based substrates

Sapphire substrates come cheap in the market and is the most common choice for growth of planar structures in nitrides. Although sapphire (α-Al_2O_3) has a rhombohedral structure, it can also be described by a hexagonal cell that is larger than the basic rhombohedral unit cell [75] (Figure 21). The hexagonal unit cell gives the lattice parameters a = 4.765 Å and c = 12.982Å. The growth of GaN or AlN

epitaxial layer on *c*-plane sapphire results in c-plane oriented layers with an in-plane rotation of 30° with respect to the sapphire(0001) substrate. This reduces the lattice mismatch between the epitaxial layer and the sapphire from 30% to 13.9%.

The sapphire templates used in this work were 1-µm-thick AlN on c-sapphire. The AFM image of these types is substrates in provided as Figure 22. These templates were deposited by MOVPE at Dowa Electronics Materials Co., Ltd. They consist of 1.0±0.1 µm-thick AlN(0001) on c-plane sapphire. The FWHM of the ω-scan measured by x-ray diffraction around the (0002) reflection is smaller than 150 arc sec, and the dislocation density is ≈ 109 cm^{-2}.

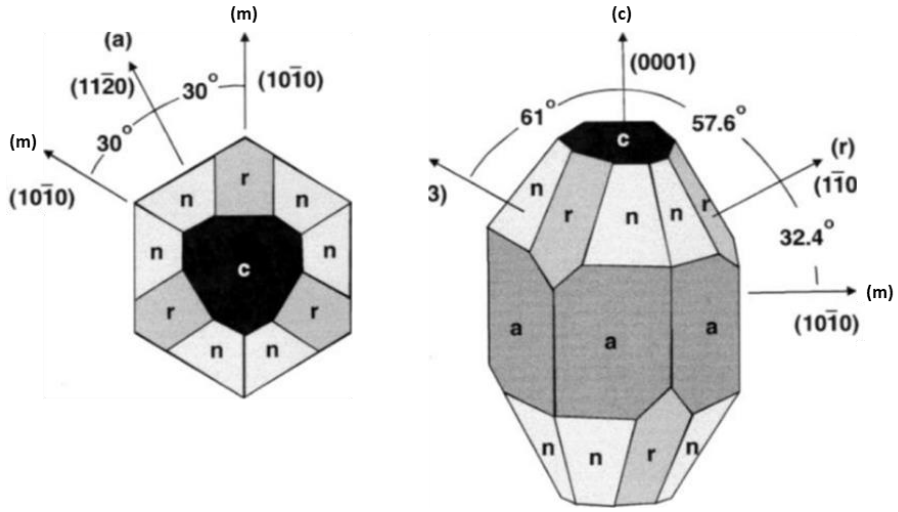

Figure 21. Illustration of the rhombohedral structure and the surface planes of sapphire [75].

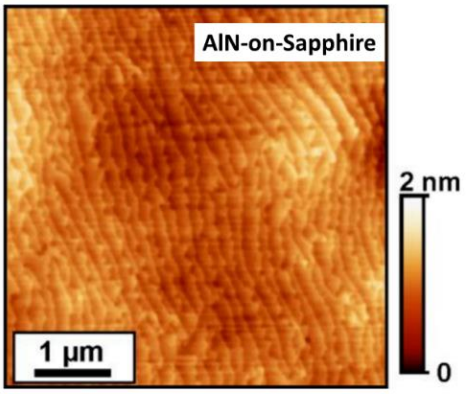

Figure 22. AFM images of the AlN-on-sapphire templates [76].

3.2.2 Si(111)-based substrates

Silicon is the most widely used material in the semiconductor electronic industry since it has many advantages, such as good thermal and electrical conductivity, reasonable prices, large scale productions support etc. The common crystal structure for Si substrate is a diamond structure with a lattice parameter, a=5.431 Å as illustrated in Figure 23. The (111) surface has a hexagonal geometry which compares well with a hexagonal system, giving an in-plane lattice parameter a_{hex}= $a_{cubic}\sqrt{2}/2$= 3.840 Å.

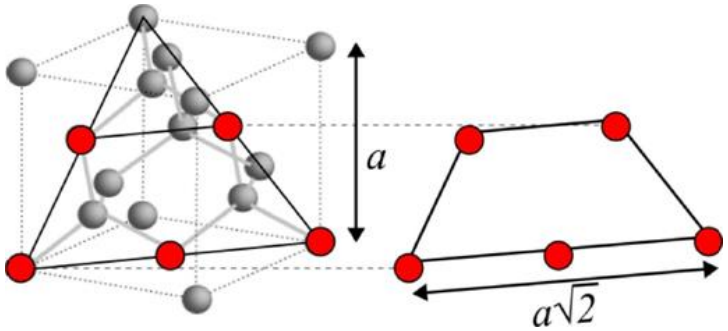

Figure 23. Silicon diamond crystalline structure compared to hexagonal structure.

Using Si(111) as a substrate for III-nitride materials has faced many challenges such as strain generated cracks (due to higher thermal expansion coefficient) and higher defect density due to lattice mismatch [77]. Hence, we used silicon-based substrates for the growth of III-nitride NWs because the differences of lattice parameters do not degrade the crystal quality for their growth as compared to their planar counterparts.

For the growth of our NWs, we used n-type Si(111) substrates with a thickness of 500±25 µm. These substrates were provided by BT Electronics.

3.2.3 Growth of nitride heterostructures: GaN, AlN, AlGaN NWs and QDs

This subsection will present detailed information on the mechanisms of MBE growth in III-nitride compounds using PA-MBE. Here, I will talk about the growth of the NWs and QDs heterostructures of GaN, AlN and AlGaN. The information presented in this section was available at the beginning of my PhD growth. Developments made during my PhD are presented in the following chapters.

a) Growth of GaN (0001)

Before the start of my PhD thesis, the PAMBE growth of 2D and 3D GaN structures were well developed, in particular for the c-plane growth front [78,79]. A well accepted model for explaining the GaN layer formation occurring during growth [80] is schematically represented in Figure 24. The phenomenon of the impinging atomic nitrogen getting attached to the growing surface is called adsorption. The impinging Ga atoms are also adsorbed on the surface but in a weakly bound physisorbed state. These can be easily desorbed from the surface. Some of the Ga adatoms could then move from this state to a chemisorbed state by forming new chemical bonds on the surface. The reverse process: chemisorbed Ga atoms converting back to a physisorbed state, can also occur. When a Ga atom meets a N atom in this chemisorbed state, is when a GaN layer is formed.

When grown N-rich, the GaN layer tends to present a facetted surface [65,81–83]. Therefore, a Ga excess, i.e. the surface covered by a layer of adsorbed Ga atoms, is a necessity to be able to get flat GaN layers [81]. In the Figure 25, a study on four regimes of Ga coverage as a function of impinging Ga flux was measured at a substrate temperature T = 740°C and under N flux = 0.28 ML/s:

- A: For Φ_{Ga} < 0.3 ML/s, a small quantity of Ga is present on the GaN surface;
- B: For 0.3 ML/s < Φ_{Ga} < 0.5 ML/s, >1 ML of Ga is present on the surface;
- C: For 0.5 ML/s Φ_{Ga}< 1 ML/s, a bilayer (2 ML) of Ga is present on the surface;
- D: For Φ_{Ga} > 1 ML/s, the system reaches the Ga accumulation regime, forming Ga droplets on the surface.

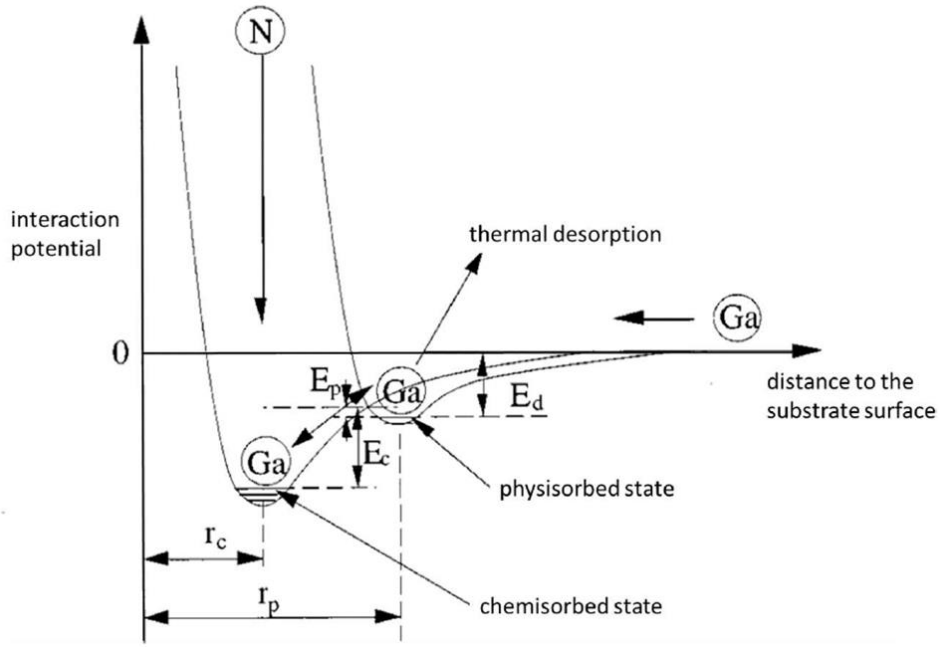

Figure 24. Schematic representation of the processes occurring during a GaN layer growth with MBE [84]. Adsorpton happens when the impinging atomic nitrogen adheres to the growing surface. The impinging Ga atoms are also adsorbed but in a weakly bound physisorbed state. It could be desorbed from this surface. Some of the Ga adatoms can be moved from this state to a chemisorbed state through the formations of new chemical bonds at the surface. The reverse process can also occur: chemisorbed Ga atoms can be transferred back to a physisorbed state. In the chemisorbed state, when the Ga atom meets an N atom, a GaN layer is formed.

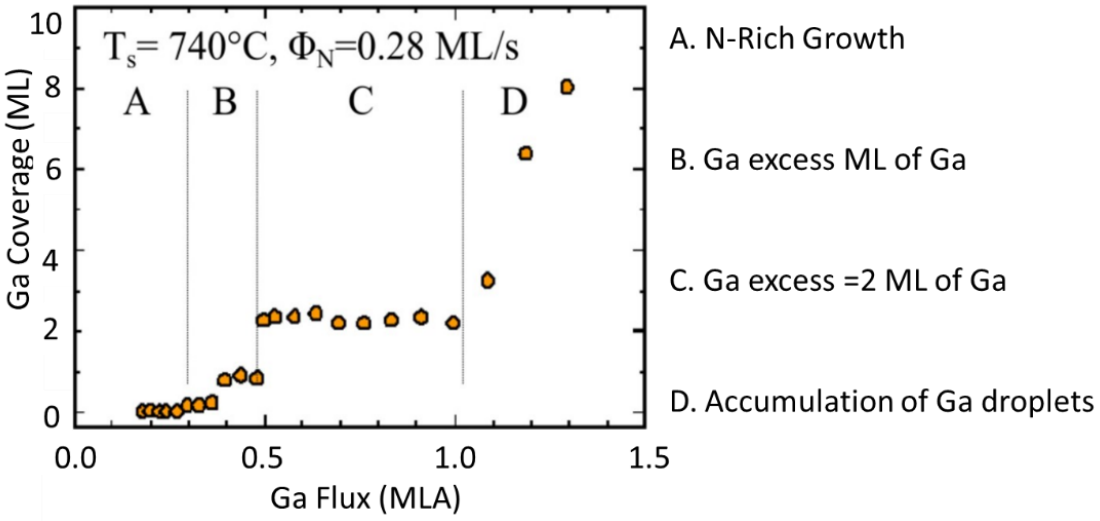

Figure 25. Ga coverage on top of the GaN (0001) surface as a function of the supplied Ga flux, measured at substrate temperature Ts=740°C and under N flux =0.28 ML/s [81].

It is important to note that the above described experiment was performed at 740°C and that at different temperatures the Ga desorption characteristics differ and this might affect Ga desorption characteristics and in turn changing the stated boundaries, as is illustrated in Figure 26 [83].

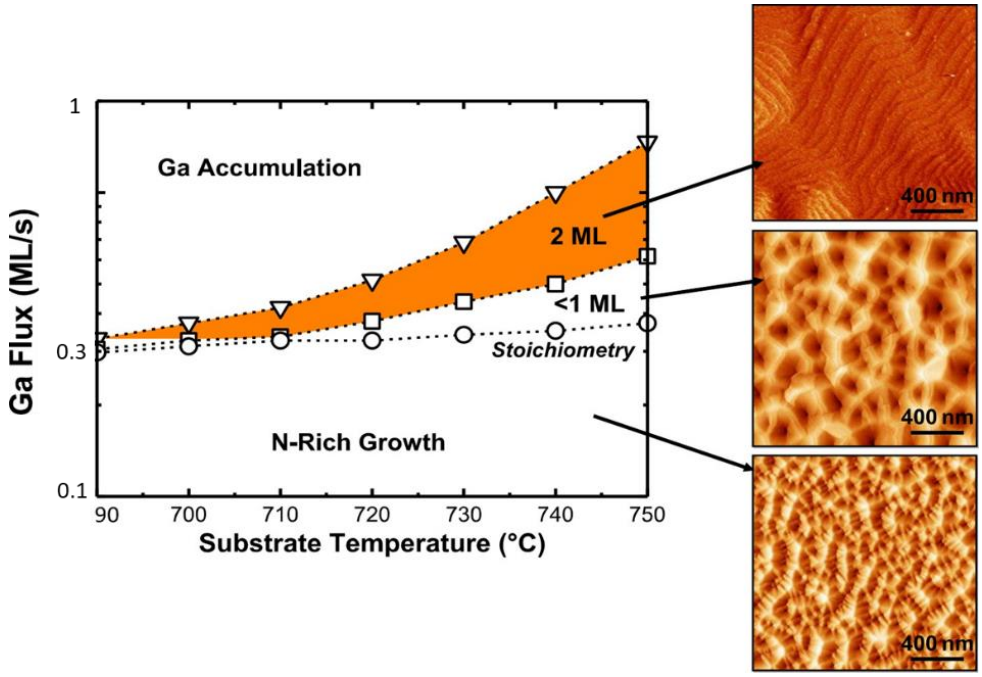

Figure 26. Ga coverage regimes as a function of substrate temperature as well as impinging Ga flux. Insets show atomic force microscopy images taken in the different growth regimes. z-scales are 5 nm, 150 nm and 100 nm (top to bottom) (modified [85]).

It has been established that the growth of GaN with a Ga excess of 2 ML reduces the (0001) surface energy, thus favoring 2D growth (see images of the sample surface in figure 23). This Ga bilayer [86] follows a laterally-contracted Ga bilayer model [87], as illustrated in Figure 27.

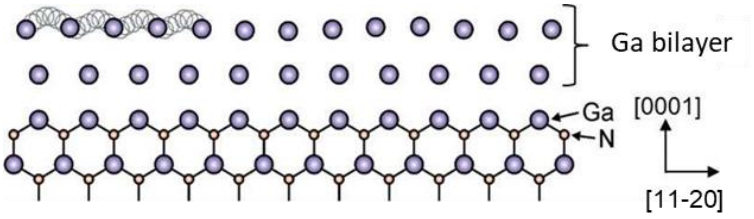

Figure 27. Schematic view of the laterally-contracted Ga bilayer model [87].

b) Growth of AlN (0001)

As is in the case of 2D GaN, the growth of 2D AlN also requires metal-rich conditions. When the growth temperature of III-N system is lower than 800°C [88], the excess of Al atoms tends to stay adsorbed on the surface. The excess Al is recognized by the shadow lines in RHEED pattern taken along azimuth, as is seen in Figure 28. These shadow lines are the proof of the excess metal Al as it has a smaller lattice constant in comparison to that of AlN. The excess Al is removed, since it does not desorb by itself, by a growth interruption under N atmosphere. This step captures the excess Al and forms AlN on the growth surface. This consumption time is used to quantify the Al excess and calculate the Al cell temperature which gives Al:N stoichiometric growth conditions.

Since the Al-N binding energy is much higher than the Ga-N binding energy, it results in preferential formation of AlN in the presence of Al, Ga, and N [89]. This phenomenon can be exploited when growing AlN at stoichiometry by using the additional Ga flux as a surfactant to improve mobility of adatoms at the growing surface. Hence, a smooth surface morphology is obtained without Ga incorporation into the AlN layer [90].

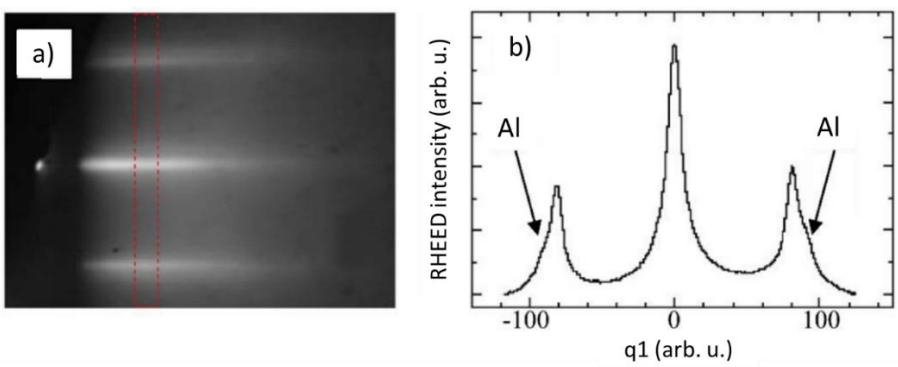

Figure 28. a) The RHEED image of an Al-rich AlN surface (azimuth<11-20>) b) Intensity profile along the direction of the region highlighted by a dashed rectangle in (a) where the extra lines indicate the presence of excess Al [85].

c) Growth of AlGaN (0001)

As it is the case with GaN and AlN, the growth of planar AlGaN also demands a metal-rich environment [89,90]. The stronger Al-N bond renders Al to primarily be incorporated in the AlGaN alloy, which means the sticking coefficient of Al is unity. So, making use of this information, the required Al content is calculated from the Al/N flux ratio. An additional Ga flux is then used to generate the metal excess that is required to obtain self-surfactant effects that finally favours 2D growth. This, however, only stands true in the case of low Al content regime and further growth parameter calculations are done for growth of AlGaN with higher Al content [90].

The difference between binding energies of AlN and GaN and the mobilities of Al and Ga adatoms pose certain difficulties during the growth. As a result, high Al content AlGaN has a strong tendency to roughen when grown at high temperature, even under metal-rich conditions. Obtaining flat layers require reducing the growth temperature even below typical values for GaN growth.

d) Growth of Nanowires

NW growth can be achieved with or without catalysts. In this work, GaN NWs were grown by PA-MBE without catalyst, under N-rich conditions on Si(111) substrates to achieve a high density of NWs. Before introducing Si(111) into the PAMBE system, it was cleaned, as usual, by using organic chemicals (dichloromethane or trichloromethane, acetone and methanol). In the growth chamber, the Si(111) substrate was heated to ≈ 880°C for 5 minutes to thermally clean the surface [91]. The proof of a clean surface lies in the observation of a (7×7) reconstruction, as illustrated in Figure 29(c), which appears at 600-850°C.

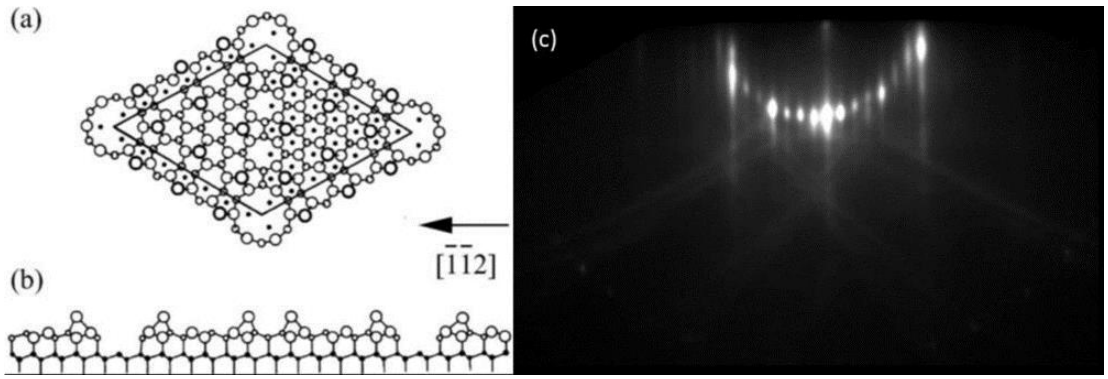

Figure 29. a) top view and b) side view of the Si (111) (7x7) reconstruction [91]. c) 7x7 surface reconstruction shown by RHEED along [-1-12] azimuth [91].

To be able to obtain GaN NWs that are fully vertical and without the infamous tilt (as reported in [92,93]) and the GaN undergrowth, which are parasitic 2D growth of GaN between the NWs, a two-step growth procedure for AlN is used [94,95]. After baking the substrate, it is then cooled down to 200°C, and 1.2 nm of AlN is deposited at stoichiometric conditions at this low temperature. Then, an 8-nm-thick AlN buffer layer is grown at stoichiometric conditions at 670°C. GaN NWs were then grown with a substrate temperature of about 780°C, to obtain a Ga/N flux ratio = 0.25.

The interesting aspect of these NWs were the $Al_xGa_{1-x}N$ dots grown within these wires using the same N-rich conditions as for the GaN base (Ga/N flux ratio = 0.25), and adding an additional flux of Al, $\Phi_{Al} = x/v_G$, where x is the targeted Al mole fraction. In this case, the Al mole fraction in the dots was intentionally kept low, x ≤ 0.1, so as to prevent deformations in the morphology of the NWs and to reduce the effects of alloy inhomogeneity that is quite often observed for x ≥ 0.3 [96]. The AlN sections were grown at stoichiometry (Φ_{Al}/Φ_N = 1, growth rate v_G = 450 nm/h).

e) Growth of AlGaN/AlN quantum dots

The formation of 3D structures on the growth surface calls for an enhanced (0001) surface energy in order to promote faceting by relaxation instead of creating dislocations. This could mean either to grow under Ga-rich conditions and perform a growth interruption in vacuum in to evaporate the excess metal [97,98], or grown under N-rich conditions [99,100]. The two types of growth lead to different results as listed below:

- With metal-rich conditions: $Al_xGa_{1-x}N$ QDs resulting from the growth in metal-rich conditions ($\Phi_{metal} > \Phi_N$) are achieved by performing a growth interruption in vacuum after growing the dots in metal-rich environment [101–103]. It follows a Frank-van der Merve growth mode and when the excess metal is evaporated, the layer re-arranges into 3D nanostructures due to the increase in (0001) surface energy. Due to the metal-rich conditions, the adatoms have a high mobility and result in low density of dots. Figure 30(b) is the AFM image of GaN dots with low density (10^{10} -10^{11} cm^{-2}) grown by Ž. Gačević, A. Das, J. Teubert, et al. who did a comparison of the two types of growth [64].

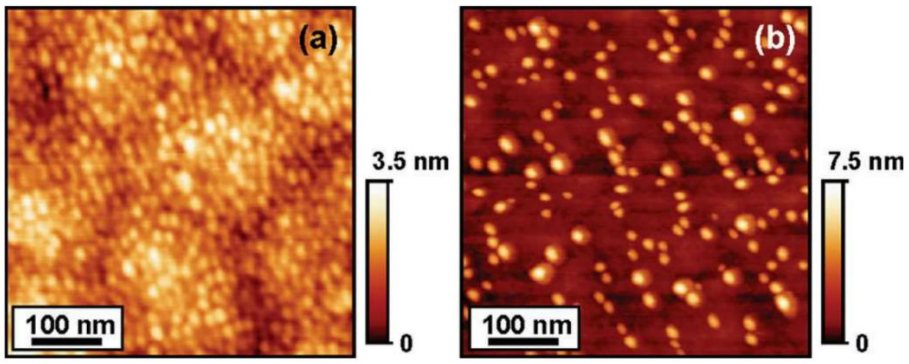

Figure 30. AFM images of GaN/AlN QDs synthesized by the deposition of 4 ML of GaN under a) N-rich and b) Ga-rich conditions. One can observe that N-rich conditions lead to densely populated smaller QDs, while Ga-rich conditions lead to scarcely populated larger dots [64].

- With N-rich conditions: $Al_xGa_{1-x}N$ QDs resulting from growth in N-rich conditions ($\Phi_N > \Phi_{metal}$) can have also been achieved [100], and is the method used in this PhD work [65]. Due to a III/N flux ratio < 1 the surface energy of the (0001) plane increases [86]. Hence, the growth favors the formation of 3D faceted structures. Under these conditions, the growth starts 2D until the deposition of a ~2-ML-thick wetting layer (critical thickness). Further deposition of

$Al_xGa_{1-x}N$ leads to the formation of 3D islands via the Stranski-Krastanov growth mode [99,100]. N-rich growth implies a low mobility of adatoms, which results in a high density of dots. Figure 30(a) is the AFM image of densely populated (10^{11} -10^{12} cm^{-2}), small (1-2 nm high) GaN QDs [64].

3.3 Characterization techniques

3.3.1 X-Ray Diffraction

To study the structural characteristics of our QDs SL in depth, we have used x-ray diffraction (XRD) in a Rigaku SmartLab diffractometer (Figure 31) to extract the periodicity, the strain state of the layers, as well as the crystalline quality of the samples from studying the reflections and their broadening. As x-ray excitation, we used the $k_{\alpha 1}$ emission line of Cu (λ_{XRD}= 0.154056 nm). For this work, we extracted the θ-2θ scans and the reciprocal space maps (RSM) of these samples.

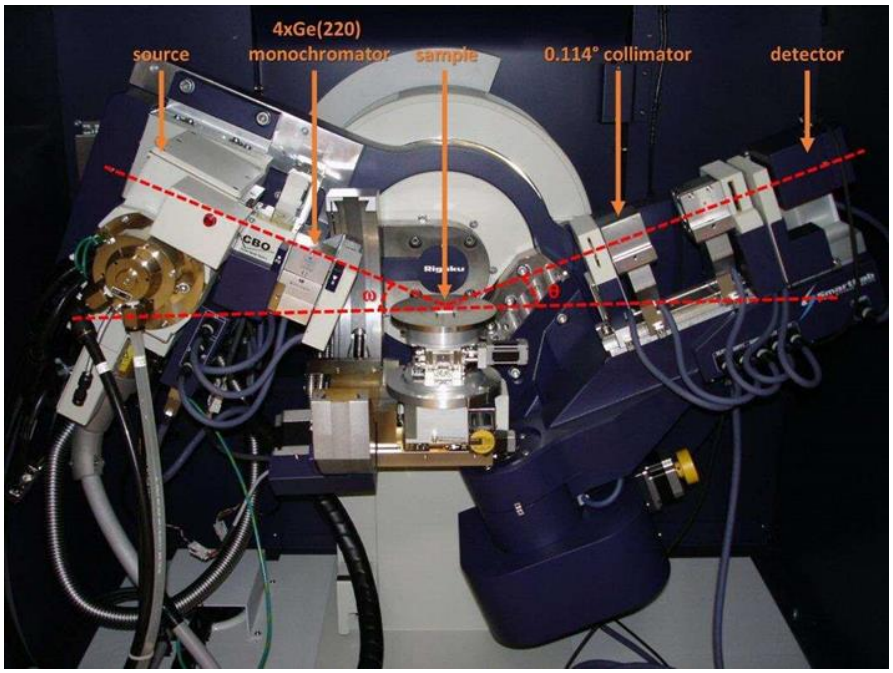

Figure 31. The Rigaku Smartlab system in the used configuration.

The x-ray source is an evacuated tube in which electrons are emitted from a heated tungsten filament and accelerated by an electric potential (≈40 kV) to finally impinge on a Cu target. The x-ray beam coming out from the source is reflected and converted into a parallel beam by a parabolic mirror. A beam of parallel (0.01° divergence) and monochromatic x-rays is incident on a crystal at the angle ω_i, which is the angle between the sample plane and the incident beam. Since the crystal has a periodic structure, we can apply the Bragg's law: $2\mathrm{d}\sin\omega_i = \mathrm{n}\lambda_{XRD}$, where n is an integer and d is the interplane spacing. A highly parallel and monochromatic incident x-ray beam is achieved by using one or two monochromators each consisting of two Ge (220) monocrystals placed between the sample and the detector. This results in an x-ray beam with a wavelength spread $\Delta\lambda_{XRD}/\lambda_{XRD}$ = 2.2 × 10^{-5} and divergence, $\Delta\theta$ = 0.0033°. However, for the NWs the measurements were done in open configuration; which means the detectors were directly exposed. This was done because of the scattering induced by the NWs which leads to broadening of the beams, leaving the high resolution redundant.

To minimize the background noise, the sample is placed on a Si plate. Since the sample surface rarely corresponds to the epitaxial planes due to the substrate miscut, the epitaxial plane needs to be aligned with the optical axis of the setup. To do this, the sample position is precisely controlled with 4 possible angular rotation mechanisms: 3 sample's rotations (ω, , χ) and 1 detector's rotation (2θ), as described in Figure 32. to achieve the resultant position illustrated in Figure 33.

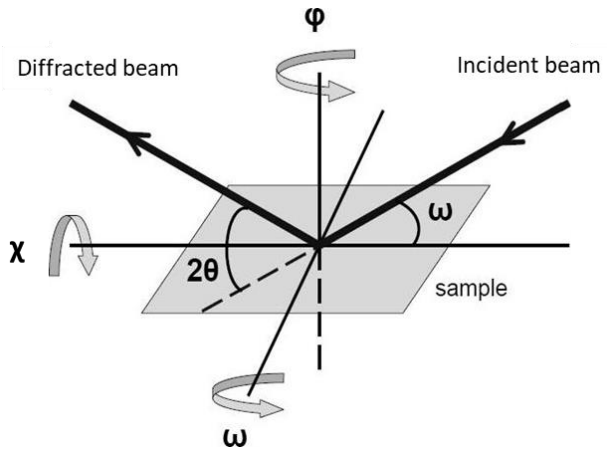

Figure 32. Schematic of all the rotation angles: ω is the angle between by the incident beam and the sample surface; φ is the angle of in-plane rotation, □ is the angle of off-plane rotation; ϑ is the angle defined by the detector direction and the sample surface

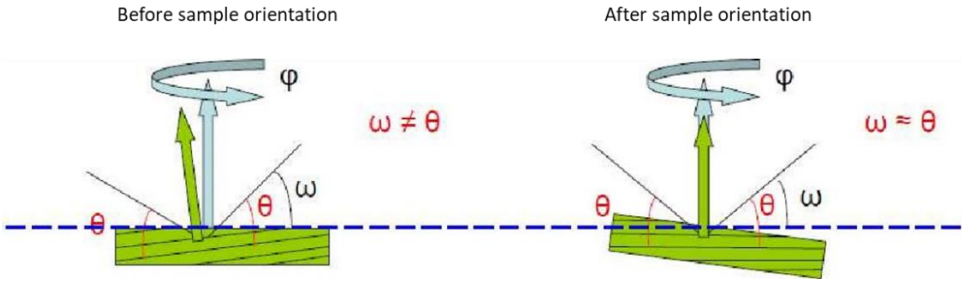

Figure 33. Illustration of the sample position before and after orientation; after rotation, the atomic planes are perpendicular to the φ - axis.

The superlattice period, P_{SL}, can be extracted from the angular separation of two SL satellites in the θ-2θ scans:

$$P_{SL} = \frac{\pm n\lambda_{XRD}}{2\sin\theta_{\pm n} - \sin\theta_0} \tag{3.1}$$

where θ_0 and $\theta_{\pm n}$ are the zero-order and $\pm n$ -order SL satellites, respectively. Information on the mosaicity and crystalline quality of planar structures are extracted from the ω scans. Then, evaluation of the strain state of the layers requires a combination of the θ-2θ scans scans of symmetric reflections and reciprocal space maps of asymmetric reflections, to extract the various lattice parameters using Bragg's law.

3.3.2 Transmission Electron Microscopy (TEM)

Transmission electron microscopy (TEM) is a microscopy technique quite often used to image at a nanoscale level based on the transmission of an electron beam through a sample. The measurements in this work (in chapters 4 and 5) were conducted by M. den Hertog, C. Bougerol and

A. Grenier. Two techniques were primarily performed on a FEI Tecnai microscope and a probe-corrected FEI Titan Themis microscope, both operated at 200 kV:

- High angle annular dark field scanning transmission electron microscopy (HAADF-STEM): Here a focused electron beam is raster scanned over the sample and the intensity of electrons scattered over relatively large angles is collected on an annular detector. The contrast in the image is related to the chemical nature of the atoms (proportional to the atomic mass) and the sample thickness. The influence of diffraction contrast is strongly reduced and it is possible to reach the atomic scale. Hence, a qualitative interpretation of the images is much easier than using TEM techniques.
- High-resolution TEM (HR-TEM): In this method, a parallel electron beam is used and the transmitted beam is captured on a camera. Heavier atoms and thicker regions can appear darker due to absorption of the electrons. Here, imaging at the atomic scale is possible. However, no direct interpretation of the images can be done due to the influence of sample thickness, defocus and diffraction contrast.

In this work, the planar samples were prepared by focused ion beam (FIB) and the nanowires were directly scratched/removed from the substrate with a holey carbon TEM grid.

3.3.3 Atomic force microscopy

Atomic Force Microscopy (AFM) is a commonly utilized characterization technique to examine the surface morphology of the samples. We used a Bruker Icon AFM system operated in the tapping mode with Bruker TESPA-V2 tips for all the samples studied with AFM in this manuscript. Then, the images were processed using the WSxM free software [104].

AFM belongs to the class of scanning probe microscopies (SPM), where a physical probe is used to scan the surface of the sample. The schematics of a typical AFM setup is described in Figure 35. The probe of the AFM is a sharp tip on the end of a cantilever arrangement. It is usually made of silicon nitride or silicon. In contact mode, the tip is made to scan across the sample in all three directions by using piezoelectric actuators. A laser beam reflected from the top of the cantilever is analyzed with a set of photodetectors.

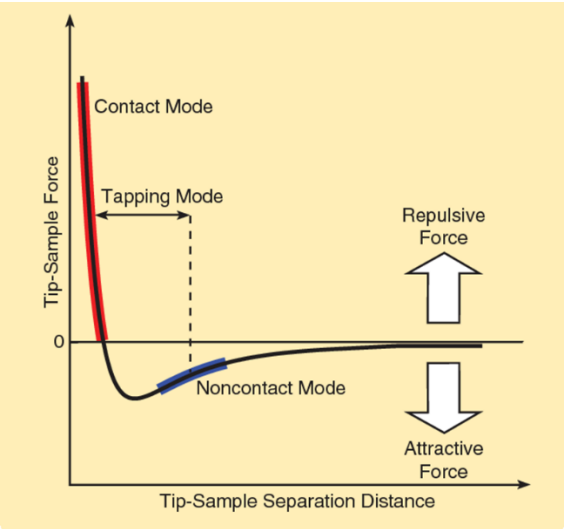

Figure 34. The tip-sample separation distance for the three main modes of atomic force microscope operation. As the tip first approaches the sample, attractive forces dominate. When the tip gets closer to the surface, repulsive forces dominate [105].

There are three most common imaging modes of AFM operation, namely contact mode, non-contact mode, and tapping mode [106]. Each of these modes differ in the way that the tip interacts with the sample during a scan (explained in Figure 34). We primarily used tapping mode, as illustrated in Figure 35, to extract the density and the average height of the QD samples.

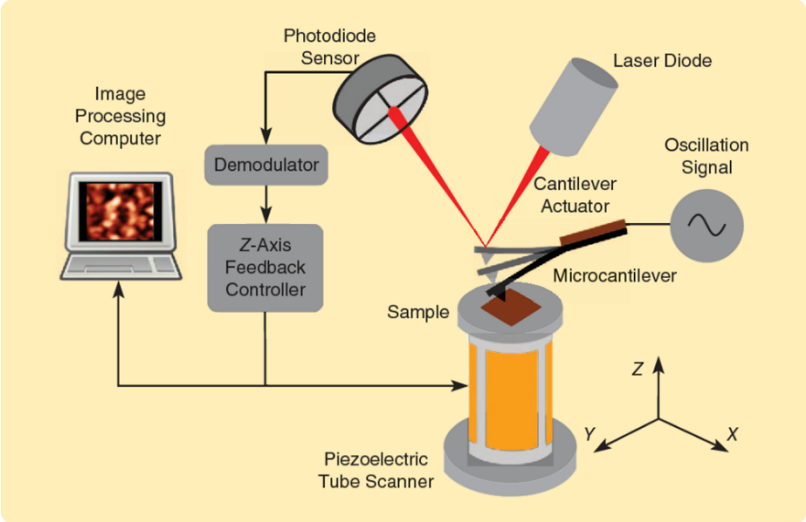

Figure 35. A schematic of the instrumentation of a typical atomic force microscope operating in tapping mode [105].

In tapping mode, the tip operates near its resonant frequency, ω_0,. The high resonance frequency (ω_0>> 1kHz) is advantageous, as it allows us to decouple the tip oscillating frequency from the low-noise frequency induced by the mechanical vibrations. ω_0 is defined by:

$$\omega_0 = \sqrt{k/m} \tag{3.2}$$

where k and m are the force constant and the mass of the tip. When the tip is close to the surface (<100 Å) it is exposed to a Van der Waals interaction gradient. At this point, the derivative of the vertical components F of the forces acting on the probe are measured. The z-gradient of the electrostatic force, ∂F/∂z, affects the resonance frequency of the tip (considering z as the displacement of the tip apex above the contact point). This gradient is defined by:

$$\omega = \omega_0 \sqrt{1 - \frac{1}{k}\frac{\partial F}{\partial z}} \tag{3.3}$$

In the tapping mode, the tip-sample distance or, in other words, the oscillating amplitude is kept in constant using a piezo-electronic actuator and a PID regulator to minimize the force gradient. So, the minimal detectable force gradient is given by [107]:

$$\frac{\partial F}{\partial z} = \frac{1}{A}\sqrt{\frac{4B_k k_B T}{Q\omega_0}} \tag{3.3}$$

where, A is the root mean square oscillation amplitude k_B is Boltzmann constant, A is the root mean square (RMS) oscillation amplitude, B_k is the detection bandwidth and $Q = \Delta\omega/\omega_0$ is the quality factor of the resonance.

3.3.4 Scanning Electron Microscopy

For this project, we investigated the structural and morphological characteristics of the nanowire samples after growth, as well as studies of nanosphere lithography (explained in Chapter 5) by using the Zeiss Ultra55 SEM. As opposed to conventional optical microscopy, one can achieve much higher resolution with SEM due to the smaller effective wavelength of electrons. A high-energy electron beam with an acceleration potential of 3-5 keV was utilized during the operation.

The working principle of an SEM is based on the interaction of a focused high energy beam of electrons with the surface of the material under study. The electrons would loose energy by scattering and getting absorbed in a volume that is in the shape of a tear as illustrated in Figure 36.

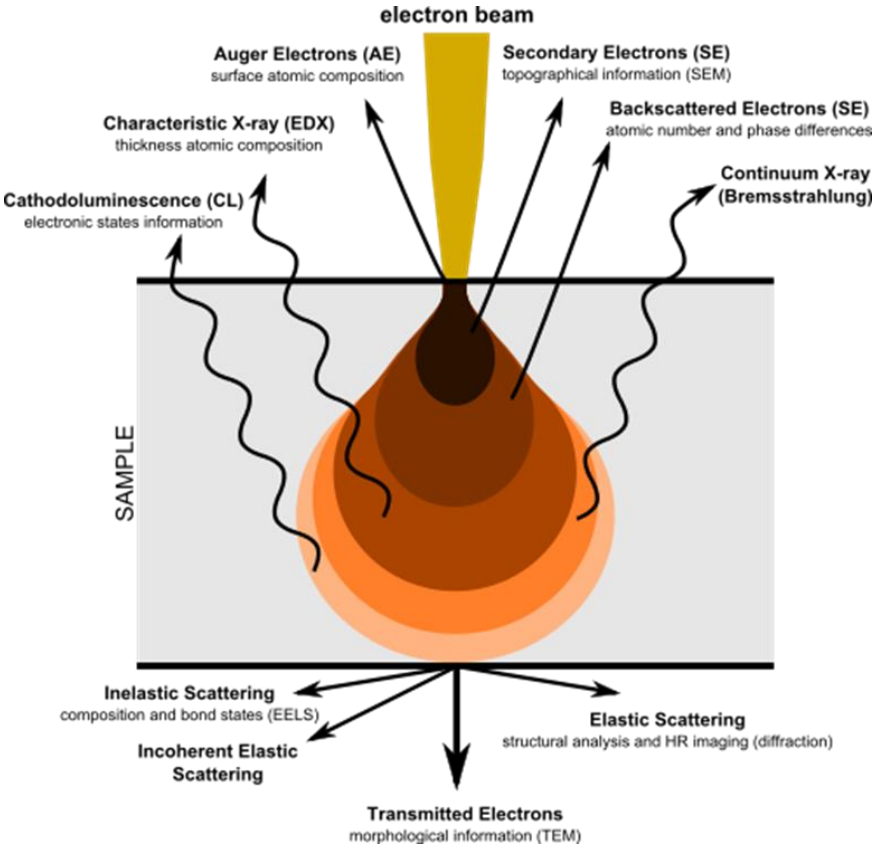

Figure 36. Illustration of the interaction volume of an electron beam impinging the sample, and the particles that are generated. (https://commons.wikimedia.org/wiki/File:Electron_Interaction_with_Matter.svg).

This interaction produces different signals coming from secondary electrons, backscattered electrons and characteristic X-rays, which are collected by detectors. From these signals, different types of images can be formed and displayed as images giving information about the sample's topography (backscattered and secondary electrons) or composition (X-ray). Normally, for this work, we utilize an in-lens detector to collect secondary electrons located inside the column of the microscope leading to efficient electron collection. We mainly collected morphology related information for nanowires and surface topography for the nanosphere lithography experiments.

3.3.5 Photoluminescence

When a material absorbs photons and emits light as a result, the process is called photoluminsescence (PL). We have used this phenomenon extensively in the form of

photoluminescence spectroscopy to study band-to-band transitions and calculate the internal quantum efficiencies (IQE). Furthermore, the technique also lets us assess the elemental composition, the presence of impurities and the material quality. PL has been found to be very sensitive to defects which enables us to detect defect bands and eliminate the causes [108].

In a typical PL setup the sample is illuminated by a laser light with an energy higher than that of the bandgap (E_g) of the sample material. Using this energy, electrons are excited from the valence band to the conduction band creating electron-hole pairs. These electron-hole pairs then recombine through radiative processes, non-radiative processes or a combination of the two. During the measurements, only radiative recombinations are directly detected. Figure 37 shows the possible recombination paths for electron-hole pairs. For each path, depending on the energy level difference between the electron and hole, the photon emitted will have a different energy.

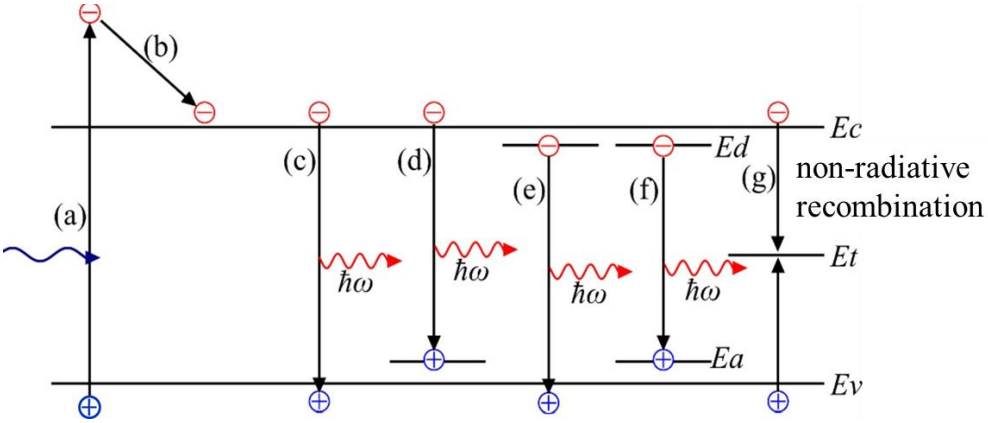

Figure 37. Schematic of carrier generation and the various radiative and non-radiative recombination paths possible.

Following are the main processes as shown in the Figure 37:

(a) Photons with energy larger than E_g and create electron-hole pairs.
(b) The excess excitation energy holes and electrons thermally relaxed to the edges of conduction and valence bands, respectively by releasing the energy in the form of vibrational modes of the crystal or phonons.
(c) Direct recombination occurs when electrons recombine with holes in the valence band, emitting photons with specific energy approximately equal to the E_g. In the case of III-nitrides, the electrons and holes generally form excitons, meaning, particles based on their Coulombic attraction. The recombination energy of these excitons is slightly lower than the semiconductor band gap energy by the value of the exciton binding energy ≈ 25 meV [109,110].

Apart from the excitonic or band to band recombinations, there are other processes that take place, namely:

(d) donor to band recombination
(e) band to acceptor recombination
(f) donor acceptor pair recombination

These processes can emit photons, resulting from additional donor band (E_d) and acceptor band (E_a) appearing in the band diagram. The E_d and E_a can either appear due to unintentional impurities or

lattice defects, or they can be due to intentional doping. Excitons can also be attracted to these impurities, resulting in reduced recombination energy (donor-bound exciton, acceptor-bound exciton) [109].

The recombination of electron-hole pairs does not necessarily lead to the emission of photons. There are various non-radiative recombination paths, for instance, recombination via a mid-gap level (E_t) that lead to:

(g) charge carriers taking relaxation paths via vibrational phonons, meaning, the heating of the crystal. The origin of mid-gap level might be attributed to vacancies, impurities, dislocations, or surface dangling bonds.

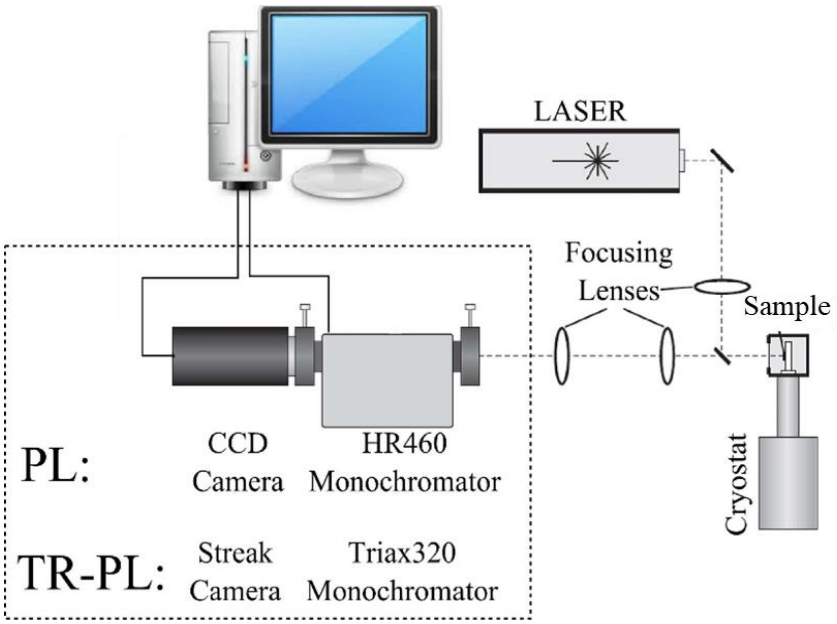

Figure 38. The PL setup used in this study.

Figure 38 illustrates the PL set-up for our experiments. The excitation was generally done under continuous-wave with a frequency-doubled solid-state laser (λ = 244 nm), with a maximum optical power of around 1 mW, focused on a spot with a diameter of ≈100 µm. Additional experiments were performed under pulsed excitation using a Nd:YAG laser (266 nm, 2 ns pulses, repetition rate of 8 kHz), also focused on a spot with a diameter of ≈100 µm. In both cases, the samples were mounted on a cold-finger cryostat, and the PL emission was collected by a Jobin Yvon HR460 monochromator equipped with a UV-enhanced charge-coupled device (CCD) camera.

In this work, the internal quantum efficiency (IQE) has been estimated using PL spectroscopy. Let us recall from section 2.2.2. that the IQE is defined as the efficiency of converting carrier current to photons. So, the room-temperature internal quantum efficiency (IQE) of the nanostructures is often estimated as the ratio of the room-temperature and low-temperature integrated PL intensities, for ease of measurement:

$$IQE\ (300\mathrm{K}) = \frac{I(300\mathrm{K})}{I(0\mathrm{K})} \tag{3.4}$$

This estimation is based on the assumption that the PL intensity saturates at low temperature as a result of the potential carrier freeze out that prevents these carriers from reaching defect-related

non radiative recombination centers. Of course, there is a risk of overstating the IQE in the case of non-radiative recombination paths being active at low temperatures. It could also be overestimated if pumping intensity is high enough to saturate non-radiative recombination paths at high temperatures. The measured IQE can be different under pulsed excitation, due to the difference in the behavior of radiative and non-radiative recombination with respect to time.

To be able to get an IQE that is only associated with material properties, measurements were performed using a continuous-wave laser, and very low power density excitation (10 µW laser power, focused on a spot with a diameter of 100 µm). It is however true that most IQE values reported in literature are measured with a pulsed laser and at much higher power densities [42,111–120], in the range of 5-1000 kW/cm^2 to be close to the operation conditions of LEDs. This procedure leads to higher IQE values, which depend on the pulse width, repetition rate and power density of the pumping laser [111–114,117,121]. Nevertheless, our samples have been characterized with the pulsed laser (266 nm, 2 ns pulses, repetition rate of 8 kHz) and the IQE variation as a function of the excitation power density was recorded purely for the sake of comparison with literature. Measurements were performed at 6 K and at 300 K. Under high excitation, the calculation of the IQE at room temperature must take into account the drop of the PL efficiency at low temperature due to the many-body effects induced by high-power excitation [117,122] so that

$$IQE(300K,P) = \frac{I(300K,P)}{I(0K,P)} \times \frac{I\,(0K,P)/P}{I\,(0K,P_{li})/P_{li}} \tag{3.5}$$

where $I(T,P)$ is the integrated PL intensity as a function of temperature and excitation power (*P*), and P_{li} is an excitation power at low excitation conditions.

3.3.6 Cathodoluminescence

The process of obtaining light emission resulting from electron injection of energy (ranging from 0.2-30 kV for us), into the material is called cathodoluminescence (CL) [123]. CL is one of the generated signals via electron beam excitation method, as illustrated in Figure 36. When exciting a material with an electron beam, the electrons from the valence band are excited to the conduction band when the kinetic energy of the beam is around three times larger than the band gap energy (E_g) of the semiconductor. After thermalizing, electrons recombine with holes in the valence band, releasing photons in the emission range. These photons are then captured on a detector imaging the respective CL spectra. CL has a wide range of applications since the system can be assembled with electron imaging techniques.

One of the applications of CL is to study the emission spectra of the samples, particularly when PL characterization is not possible because the luminescence is expected at energies comparable or higher than the energy of the pumping laser. As CL is an “above band gap” excitation method, all the materials within the excitation volume is excited no matter the value of E_g. This makes it different from PL where the excitation laser typically excites certain parts in the materials having a value of E_g lower than the excitation light whereas the other parts remain transparent. For example, to measure the PL of GaN/AlN SLs, the excitation laser (E_{photon} = 5.08 eV, in one of our cases) can excite only GaN (E_g = 3.51 eV at low temperature [13]) while AlN (E_g = 6.23 eV at low temperature [13]) let photons passing through.

In the case of CL implemented in a scanning electron microscope, various types of measurements can be conducted. For instance, it is possible to concentrate the beam in a fixed spot and measure the emission spectrum or choose a scanning an area and measure the emission map considering a spectral

band, or take an average spectral measurement. In a SEM, the electron beam can be concentrated in a spot smaller than 100 nm, which allows us to characterize a very specific area of a sample. It is also possible to change the volume of excitation, especially along the depth by varying the acceleration voltage.

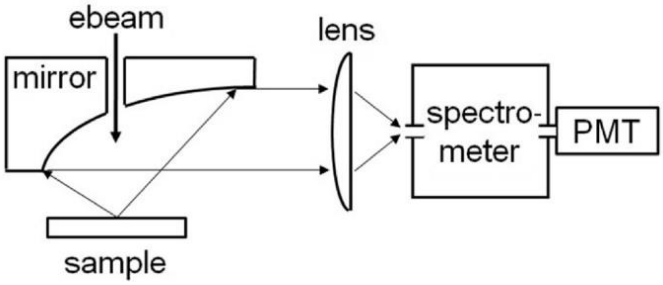

Figure 39. CL imaging set-up [124].

In this work, the spectral measurements were mainly done on a setup consisting of an SEM (FEI Quanta 200) equipped with a cathodoluminescence accessory and a low temperature (liquid helium) stage (Gatan) to be able to conduct low temperature measurements. The optical assembly for the CL imaging is illustrated in Figure 39. The light generated in the sample materials by the SEM electron beam is collected through a parabolic mirror and focused on the entrance slit of a spectrometer (Jobin Yvon HR460). A single-channel Hamamatsu PMT R928 detector is placed at the exit slit of the spectrometer. The current delivered by the PMT is amplified and synchronized to the electron beam scan in order to obtain CL mapping of the sample in monochromatic or panchromatic mode. The electrons pass through the hole in the parabolic mirror and then penetrate into the sample which is placed at the focal point of the mirror. The mirror reflects the emission from the sample into a parallel beam which is focused onto a Jobin Yvon HR460 monochromator. The monochromator scans over a specific range to project photons on to a detector. There are two detectors equipped to the monochromator, i.e. charge-couple device (CCD) camera and photomultiplier tube (PMT) detector. The CCD camera is used to acquire photons as a function of wavelength that is changed by the grating in the monochromator. The PMT is used to obtain the CL intensity mapping at one specific wavelength by synchronizing it to the raster electron beam [124].

To perform additional CL experiments, like angular distribution of the luminescence and WPE calculations, we have used a CL setup available at the Institut Lumière Matière, under the supervision of Prof. S. T. Purcell. The electron beam excitation was provided by a Kimball Physics EGPS-3212 electron gun operated in direct current mode, under normal incidence. The beam spot diameter was 4 ± 1 mm. The gun was operated with an acceleration voltage in the range of 3–20 kV, injecting up to 800 µA of current. The CL emission was analyzed using an ANDOR ME-OPT-0007 UV–NIR light collector coupled with an ANDOR Shamrock500i spectrograph connected to an electron-multiplying CCD Newton 970 from ANDOR operated in conventional mode. To measure the angular distribution of the UV emission, a calibrated UV photodetector (GaP) was attached to a rotator in the chamber and then moved in a circular motion around the sample to be able to measure the luminescence on the top half of the circle, as shown in the Figure 40.

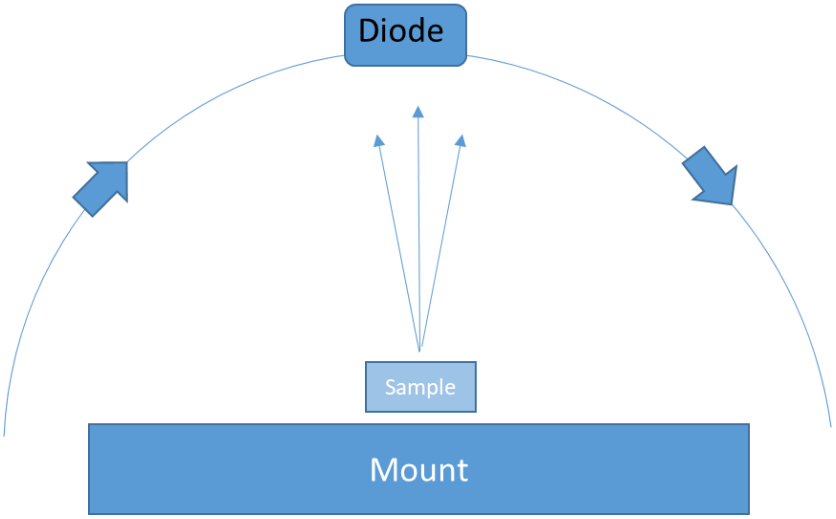

Figure 40. The angular CL imaging set-up with a diode that moves in an angular motion.

For the estimation of the WPE, we used the measurements of angular luminescence and calculated the output power of the samples. As we know from equation 2.18, the WPE is the power efficiency, i.e. the ratio of the radiant flux (measured in watts, P_{opt}) and the electrical input power. Here, P_{opt} is calculated as

$$P_{opt} = \frac{1}{R_\lambda}\int_0^{\pi/2} \frac{I_D}{A_D} 2\pi R^2 \sin\theta d\theta \tag{3.6}$$

where R_λ is the responsivity of the photodiode at λ, R is the distance between the photodiode and the sample and A_D is the optical area of the photodiode, and θ is the angle of rotation around the sample.

3.4 Simulations

3.4.1 NextNano³

Nextnano³ software simulations were carried out for calculating the strain distributions and electronics structure of our samples. This is a commercial software with a self-consistent Schrödinger-Poisson equation solver. The model used to simulate was based on the **k·p** perturbation theory for calculating the quantum levels [125]. In this work, the strain distribution, electronic band structure, quantum levels and recombination probabilities of our nanostructures were simulated in 1D and 3D format. The material parameters used are listed in Table 7 [83]. All the bowing parameters were set to zero for simulating $Al_xGa_{1-x}N$ alloys.

Parameters (Units) [Ref.]	Symbols	GaN	AlN
Lattice parameters (nm) [15]	a	0.3189	0.3112
	c	0.5185	0.4982
Spontaneous polarization (C/m^2) [126]	P_{SP}	-0.034	-0.090
Piezoelectric constants (C/m^2) [127]	e_{31}	-0.49	-0.60
	e_{33}	0.73	1.46
Elastic constants (C/m^2) [31,33]	C_{11}	390	396
	C_{12}	145	137
	C_{13}	106	108
	C_{33}	398	373
	C_{44}	105	116
Band gap (eV) [15,128]	E_G	3.51	6.2
Conduction band offset with GaN (eV) [15,128]	ΔE_{CB}	0	0
Electron effective mass (m_{e0}) [15,129]	m_e^*	0.2	0.3
Hole effective mass (m_{h0}) [15,129]	m_h^*	1.6	1.44
Luttinger parameters [130]	A_1	-5.947	-3.991
	A_2	-0.528	-0.311
	A_3	5.414	3.671
	A_4	-2.512	-1.147
	A_5	-2.510	-1.329
	A_6	-3.202	-1.952
	A_7	0	0
Conduction band deformation potentials [131]	a_{c1}-D_1	-5.81	-4.3
	a_{c2}-D_2	-8.92	-4.6
Uniaxial valance band deformation potentials [131]	D_3	5.47	2.68
	D_4	-2.98	-1.74
	D_5	-2.82	-2.07

Table 8. Material parameters used in nextnano[3]

3.4.2 Monte Carlo simulations using CASINO software

For a more precise estimation of the penetration depth of the electron beam, we performed Monte Carlo simulations of the electron beam interaction with GaN, $Al_{0.67}Ga_{0.33}N$ and AlN varying the V_A, using the CASINO 2.51 software [132]. These simulations study the electron beam interaction with solid structures to precisely predict the volume of material that electrons can penetrate through [133]. The spatial distribution of the electron trajectories is affected by a number of inelastic and elastic interactions that take place within the material. Due to the interaction of the electron beam with an atom, the electrons give up their energy to an electron in the valence band producing an electron-hole pair. These then recombine and subsequently emit photons. By comparing the emission and the Monte Carlo simulations, we can get information regarding the structure (SL thickness in our case) and material properties. The spatial extent of motion of the electrons and interaction depends on the

energy of the incident beam and the material density.

For the simulations, the software takes into account the size of the beam, number of electrons and density of material. We considered ≈ 100,000 electrons and 4 nm of beam radius. For the density, we used ρ = 6.10 g/cm^{-3} for GaN and ρ = 3.26 g/cm^{-3} for AlN.

4 AlGaN/AlN Quantum dots in GaN nanowires

This chapter elaborates on the growth and characterization of GaN NW terminated with an AlGaN/AlN QD superlattice. The text starts with the introduction and motivation to work on NWs for UV lamps, including several advantages. I then introduce the design of the heterostructure and the reasons for fixing the dimensions for our particular application. Finally, I discuss the detailed optical characterization that I performed on these wires to define their cathodoluminescence properties.

The samples presented in this chapter were grown prior to the beginning of my project by Ioanna Dimkou, who was also in charge of the SEM and theoretical calculations. XRD and TEM measurements were performed by Edith Bellet-Amalric and Martien den Hertog. I was responsible for the optical characterization of the structures, including the efficiency measurements. The work was coordinated by Eva Monroy.

The results presented here were accepted for publication as "**Assessment of AlGaN/AlN superlattices on GaN nanowires as active region of electron-pumped ultraviolet sources**", I. Dimkou, A. Harikumar, et al., Nanotechnology 31, 204001 (2020) [122].

4.1 Introduction and motivation

For the purpose of fabricating electron-pumped UV lamps, nanowire arrays are an interesting choice as active media. Semiconductor nanowires have proven to be effective and an innovative material approach for being applied in the fields of electronics, optoelectronics, sensors and energy conversion [122,134]. There are several advantages to the nanowire geometry like strain compliance, high crystalline quality, and the possibility of self-assembled growth on silicon substrates, which reduces the production costs of the final device. From an optical standpoint, the nanowire geometry naturally favours light extraction without the need for any further processing, like surface roughening for planar layers. The implementation of quantum dots within the wires provides three-dimensional (3D) carrier quantum confinement [135–138], which naturally results in an enhancement of the IQE at room temperature [96,139].

It is often a topic of contemplation as to whether these "dots" embedded in NWs with a diameter of around 50 mm are actually "quantum dots" since the potential radial confinement is very weak as opposed to the vertical confinement. Some argue from appearances that these look more like "quantum wells" and prefer to call them "nanodisks". In our case, we choose to call them "quantum dots" due to their optical behaviour. It has been reported in previous studies in GaN/AlN dots in wires, [135], with correlation measurements the antibunching properties [62], which is a signature of quantum dot behaviour. Also, the significant reduction of non-radiative recombination, which gives high PL lifetimes rather stable in the 5-300 K temperature range [140], is a clear indication of 3D confinement of carriers.

I start by explaining the choice and design of the heterostructure. Then the optical performance of a GaN/AlN quantum dot superlattice (SL) in nanowires is compared with the emission of planar GaN/AlN SLs with the same periodicity and thickness grown on bulk GaN substrates along the N-polar and metal-polar crystallographic axes. Then, I show how we adjusted SL peak emission in the range of 340 to 258 nm by varying the dot/barrier thickness ratio along with the Al content in the dots. Finally I will come to the cathodoluminescence studies performed to learn if they are the right fit for application in electron pumped UV lamps.

4.2 Design of the structure

Embedding QDs into NWs is particularly challenging. For their application in electron-pumped devices, it is essential to have reproducible geometry and composition of the quantum dots in a superlattice that is hundreds-of-nanometres long (which exceeds the penetration depth of the electrons). The problem with NWs is that they generally present large spectral dispersion [96,141] due to the variation of the dot geometry [142–144] and variable strain [142,143,145] along the growth axis, the emergence of interdiffusion at the heterointerfaces [96], and the unwanted structural variations appearing due to NW coalescence [146].

To describe the design of N-polar $Al_xGa_{1-x}N$/AlN ($0 \le x \le 0.1$) quantum dot superlattices deposited on self-assembled GaN nanowires we must understand the superlattice. The superlattice here has to be long enough to collect the electron-hole pairs generated by an electron beam with an acceleration voltage V_A = 5 kV. Next, the band gap, E_g, needs to be tuned to achieve the desired peak emission wavelength.

To get an active region of the length larger than the penetration depth of the electron beam, which can be represented as R_e. A widely accepted empirical expression for R_e is:

$$R_e = \frac{4.28 \times 10^{-6}}{\rho} V_A^{1.75} \tag{4.1}$$

where ρ is the material density in g/cm^3 and V_A is the acceleration voltage in kV. When applied to GaN (ρ = 6.10 g/cm^{-3}) and AlN (ρ = 3.26 g/cm^{-3}) while assuming V_A = 5 kV, we get an R_e = 115 nm and R_e = 215 nm, respectively.

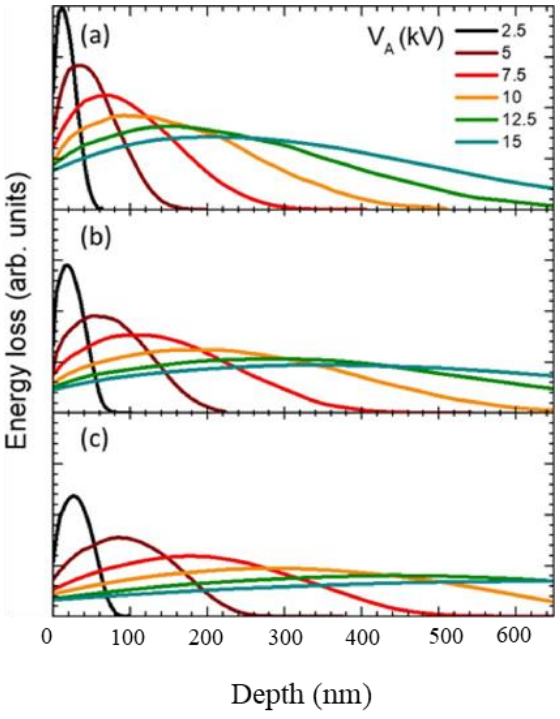

Figure 41. Energy loss as a function of depth by an electron beam penetrating in a) GaN,(b) $Al_{0.67}Ga_{0.33}N$ and (c) AlN for various accelerating voltages, V_A. The curves were obtained by performing Monte Carlo simulations using the CASINO software [132].

Then, for a more precise estimation of R_e, we performed Monte Carlo simulations of the electron beam interaction with GaN, $Al_{0.67}Ga_{0.33}N$ and AlN varying the V_A, using the CASINO software [132]. The obtained results are shown in Figure 41.

With these simulations, the predicted values of R_e at V_A = 5 kV are around 175 nm, 224 nm, and 260 nm for GaN, $Al_{0.67}Ga_{0.33}N$ and AlN, respectively. The reason for considering the penetration depth in $Al_{0.67}Ga_{0.33}N$ is that it reflects the average Al content in the active region for some of the heterostructures studied.

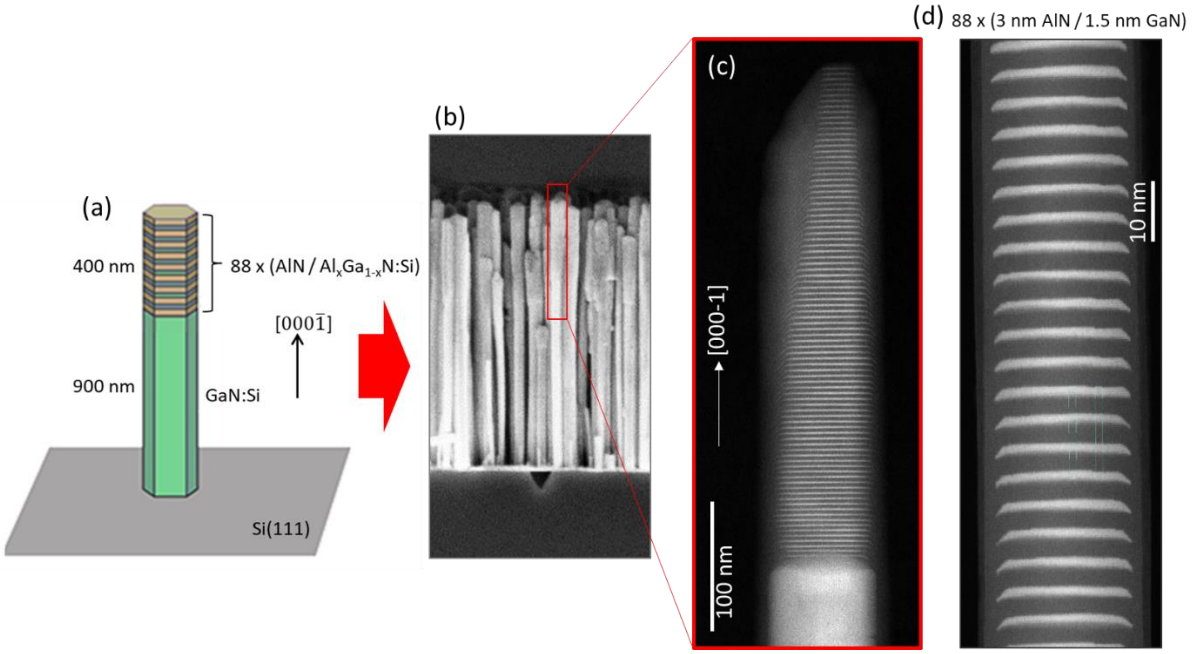

Figure 42. (a) Simplified schematic representation of the grown NW structure along with the (b) SEM image of as-grown sample E3857 (giving the general view of the heterostructure). (c-d) HAADF-STEM views of the SL, where bright contrast corresponds to GaN and dark contrast corresponds to AlN.

Next, to tune the spectral output, the Al content in the dots were varied and the dot/barrier thickness ratio, i.e. the total number of dots and the active region length was kept constant. To be able to properly evacuate charges during the process of electron pumping, the NWs were grown on n-type Si(111) with a resistivity in the range of 0.001-0.005 Ωcm. The NW base and the dots were doped n-type with [Si] = 5×10^{18} cm^{-3} (this value is estimated from Hall effect measurements using the Van der Pauw method on planar Si-doped GaN layers).

These N-polar NWs were grown catalyst-free with a bottom up approach. As explained in Chapter 3, PAMBE was used to grow the NWs on n-type Si(111) substrates after the growth of a low-temperature two-step AlN nucleation layer [43,94,147]. To get a more uniform height across the substrate surface [148], a long (≈ 900 nm) GaN NW base was grown under N-rich conditions (Φ_{Ga}/Φ_N = 0.25). This resulted in a GaN NW density of around 6-8×10^9 cm^{-2}, with a NW diameter in the range of 30-50 nm.

To synthesize the active region, $Al_xGa_{1-x}N$/AlN (x = 0, 0.05, 0.10) was deposited to create the 400 nm long SL, consisting of 88 periods of QDs. The $Al_xGa_{1-x}N$ dots were grown using the same N-rich conditions as utilised for the GaN base (Φ_{Ga}/Φ_N = 0.25). The complete heterostructure was synthesized at T_S = 810 °C without any growth interruption. A summary of the samples under study is presented in Table 9.

Sample	t_W (nm)	t_B (nm)	alloy fraction x	XRD Period (nm)	Peak emission (nm)	IQE (%)	FWHM (nm)	average diameter (nm)
E3857 E3898	1.5	3.0	0	4.4±0.1	340 336	63 60	31 30	54.5±11.6 91.6±19.9
E3858	1.5	3.0	0.05	4.4±0.1	331	34	27	
E3859	1.5	3.0	0.1	4.6±0.1	335	42	29	65.6±14.0
E3861	1.0	4.0	0	5.0±0.1	324	55	25	64.0±28.7
E3862	0.75	3.75	0	4.4±0.1	296	48	22	90.7±29.5
E3863	0.75	3.75	0.1	4.3±0.1	286	44	16	88.8±13.5
E3918 E3864	0.65	3.85	0	4.1±0.1	277 265	29 31	23 36	81.3±16.7 87.5±19.6
E3865	0.65	3.85	0.1	4.1±0.1	258	22	34	91.2±24.4
E3889G	1.5	3.0	0	4.4±0.1	329, 343	<0.05	9, **11**	
E3889N	1.5	3.0	0	4.1±0.1	329, 342, 367	<0.4	9, 13, **24**	

Table 9. Structural and optical characteristics of the samples under study. Nominal thickness of barriers (t_B), nominal thickness of the $Al_xGa_{1-x}N$ wells (t_W), Al concentration in the wells (x), MQW period measured by XRD, peak emission wavelength at room temperature (in the case of multiple peaks, the dominant peak appears in bold fonts), internal quantum efficiency (IQE) at room temperature (measurement under low-injection conditions), and full width at half maximum (FWHM) of the emission at room temperature.

Looking at the SEM image of GaN/AlN QD superlattices on GaN NWs, e.g. Figure 42(b) showing sample E3857, we note the high density of NWs in the ensemble . The HAADF-STEM image of the zoom-in of the SL in E3857, where the bright contrast is GaN and the darker contrast corresponds to AlN. Along the NW, the heterostructure has a general thickness of 1.5 ± 0.2 nm for GaN and 2.8 ± 0.2 nm of AlN, with the whole GaN/AlN QD superlattice enveloped by an AlN shell. Observing along the SL shows that the thickness of the GaN section increases up to 0.5 nm from the base to the end. It can also be observed that the thickness of the AlN shell decreases along the NW growth axis going almost negligible at the top of the NWs and having a maximum thickness of around 5 nm at the interface with the GaN base. It is also apparent that the cross section of the GaN dots is not rectangle, but in fact trapezoidal, with {1−102} facets towards the NW sidewalls. If we study the early stages of the growth of the heterostructure, which are visible in Figure 42(c), there is an obvious diffusion of Ga from the stem into the first two periods of the SL. This type of Al-Ga intermixed regions have been reported previously in GaN/AlN SLs [96]. They are explained by the strain-driven out-diffusion of Ga induced by the lattice mismatch between GaN and AlN.

Figure 43 shows HAADF-STEM images of the sample with smaller QDs, E3865, with zoomed images of the top and bottom of the superlattice. In this sample, the QDs are only 3 monolayers thick. However, homogeneous growth is achieved along the 400 nm of the superlattice. The Ga out-diffusion in the initial stages of the SL growth affects only two AlGaN/AlN periods.

The structural characteristics of the GaN/AlN superlattices were also investigated by high-resolution XRD. Figure 44 shows $\theta - 2\theta$ scans around the GaN (0002) reflection for sample E3857. The result is compared with planar layers with Ga and N polarity (E3889G and E3889N, respectively), with the same SL period as E3857. In the nanowire sample, the angular location of the reflection from the GaN stem is shifted to higher angles with respect to relaxed GaN, which confirms that it is compressively strained by the AlN shell. From the inter-satellite distance, we extract the SL periods listed in Table 9, which are in good agreement with the nominal values. Using the Ga-polar sample as

a reference, the N-polar structure presents broader reflections due to the larger inhomogeneity in quantum well thickness. In the case of nanowires, thickness fluctuations from wire to wire within the ensemble introduce an additional broadening factor. Nevertheless, the satellites of the SL reflection are still well resolved, and their linewidth is comparable to the N-polar structure.

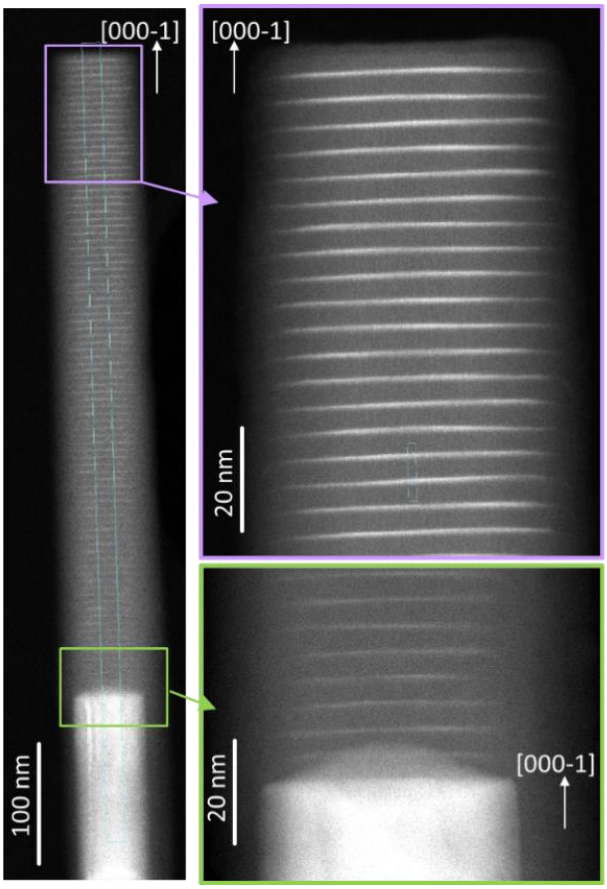

Figure 43. HAADF-STEM image of the sample of SL with with 88 x (3 nm AlN / 0.65 nm AlGaN emitting at 258 nm (E3865). Dark/bright contrast corresponds to Al-rich/Ga-rich areas. We observe homogeneous thickness and strain-driven out-diffusion of Ga extending around 1.5 periods [122].

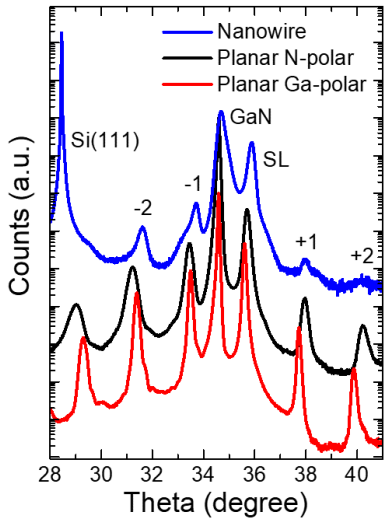

Figure 44. XRD $\theta - 2\theta$ scans of samples E3857, E3889G and E3889N, recorded around the (0002) reflection of GaN. The scans are vertically shifted for clarity. Labels indicated the (111) reflection of the Si substrate, the (0002) reflection of GaN, and the (0002) refl reflection of GaN, and the (0002) reflection of the superlattice, with several satellites [122].

4.3 Optical characterization

4.3.1 Photoluminescence

The NWs with peak emission at wavelengths longer than 280 nm were characterized using photoluminescence spectroscopy to assess their optical performance. As an example, the PL spectrum at 5 K for the sample E3857 is displayed in the Figure 45(a), compared to the spectra from planar layers with Ga and N polarity (E3889G and E3889N, respectively). The peak emission wavelength of the three samples is relatively close, in the 336-340 nm range. The spectra from planar samples present a multi-peak structure due to monolayer thickness fluctuations in the quantum wells [149], with the Ga polar sample presenting narrower lines. In contrast, the emission for the nanowire sample consists of a single spectral line, centered at 337 nm, with a large linewidth due to the geometry fluctuations in the nanowire ensemble.

The integrated PL intensity as a function of temperature is depicted in Figure 45 for samples E3857, E3889G and E3889N under continuous-wave, low-injection (power density = 0.00013 kW/cm^2) excitation. The luminescence from the planar structures drops by more than two orders of magnitude when increasing the temperature from 5 K to 300 K. In contrast, the emission intensity from the nanowires remains constant up to 100 K and remains at 63% of its maximum (low temperature) value at 300 K. This result confirms the relevance of carrier confinement in hindering non-radiative recombination.

As mentioned in Equation 3.4 in chapter 3, the room-temperature internal quantum efficiency (IQE) of the nanostructures is often estimated as the ratio of the room temperature and low-temperature integrated PL intensities. This estimation is based on the hypothesis that the PL intensity saturates at low temperature because of the carrier freeze out which prevents carriers from reaching defect-related non-radiative recombination centers. There is hence a risk of overestimation of the IQE if non-radiative recombination is active at low temperature, but also if the pumping intensity is high enough to saturate non-radiative recombination paths at high temperature.

To get an estimation of the IQE associated with the material properties, we tried to introduce as few extraneous perturbations as possible to straightforward linear response. Thus, the measurements presented here were performed using a continuous-wave laser, and very low power density excitation (10 µW laser power, focused on a spot with a diameter of 100 µm). The results in Figure 45(b) show that the luminescence from planar samples 3889G and 3889N clearly does not attain saturation at low temperature, so that the IQE calculated from these curves should be taken as an upper limit. On the contrary, all the nanowire samples in the study present a clear saturation of their PL for temperatures lower than 100 K, as shown for E3857 in Figure 45(b). Therefore, the ratio of their room temperature and low temperature PL intensities can be considered as a good estimation of their QE . The obtained IQE values are summarized in Table 9, together with the peak emission wavelength and linewidth at room temperature. In the case of E3857 and E3898, the IQE at room temperature is 60-63%, orders of magnitude higher than the IQE of planar structures with the same layer sequence (3889G and 3889GN). The higher value of IQE in 3889N in comparison to 3889G is explained by the localization of carriers in the thickness fluctuations observed in the N-polar structure.

When the perturbation introduced by the excitation source is very small (low injection regime), the IQE values describe the material properties in terms of radiative and non-radiative processes. However, it is difficult to compare these data with the literature since most reported values are measured under pulsed excitation [42,111–120], using power densities in the range of 5-1000 kW/cm^2 [111–114,116,117], to emulate the carrier injection at LED operating conditions. In this pumping

regime, the photo-generated carrier densities are higher than the doping level of the original structure (high injection) and nonradiative recombination paths are partially saturated. Therefore the obtained IQE is significantly higher than the low-injection value and depends on the excitation power density [111–114,117,121]. Maximum values of IQE are obtained for an excitation power density around 10-100 kW/cm^2 [114,117]. Note that in an electron-pumped UV lamp using an acceleration voltage of 5 kV and an injection current of 1 mA to irradiate a spot with a diameter of 1 mm, the excitation density would be below 1 kW/cm^2.

To explore the behaviour of the nanowire heterostructures under operating conditions, and compare with previous literature, we have measured PL as a function of the excitation power using a pulsed Nd-YAG laser. Measurements were performed at 6 K and at 300 K as mentioned in section 3.3.5. and the IQE was calculated with the equation 3.4.

The results for samples E3857, 3889G and 3889GN are presented in Figure 45(c). In the case of planar samples, the IQE increases with pulsed excitation. A maximum IQE around 3-4% is obtained for excitation in the range of 100-500 kW/cm^2. The values are lower than the IQE = 15-50% that can be found in the literature for this spectral range (measured by the same method) [114,117,121]. This difference can be explained by the choice of AlN/GaN as materials for barriers/wells, to be used as a reference for the nanowire heterostructures. In this case, the lattice mismatch is maximum in comparison with generally used $Al_xGa_{1-x}N/Al_yGa_{1-y}N$ heterostructures. This leads to enhanced plastic relaxation of the misfit strain [150], which has an important effect on the maximum IQE [112]. Looking back at Figure 45(c), in the case of quantum dots contained in nanowires, the IQE is stable under pulsed excitation up to around 50 kW/cm^2, and then decreases slightly.

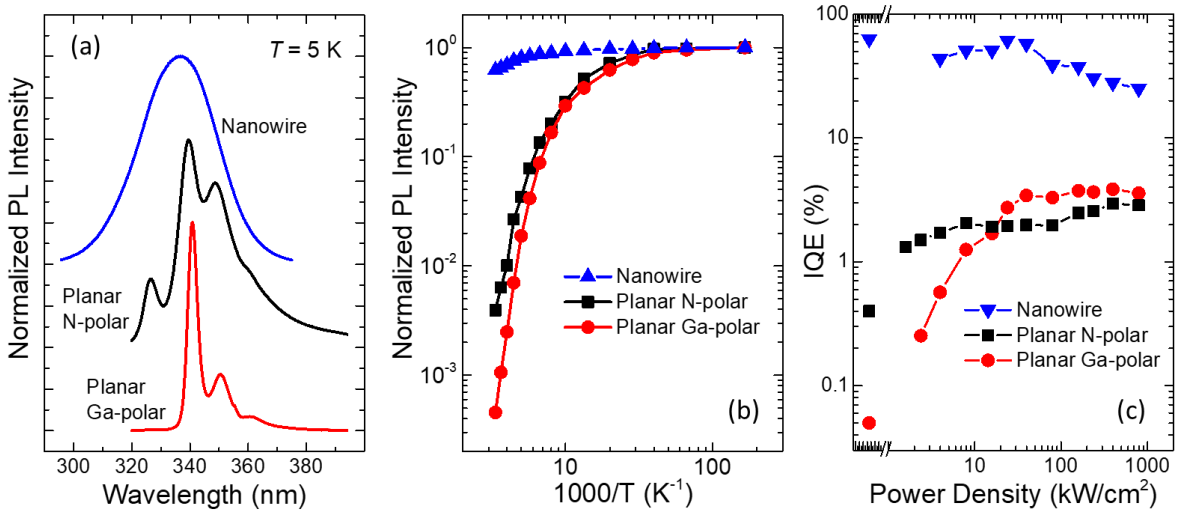

Figure 45. a) Variation of the PL spectra as a function of the temperature of the sample E3857 b) Intensity variation as a function of temperature for sample E3857 compared with E3889G and E3889N taken under continuous-wave, low-injection (power density = 0.00013 kW/cm2) excitation. c) Variation of the IQE at room temperature as a function of the excitation power density measured with a pulsed Nd-YAG laser. PL remains stable from 5 K to 100 K, decreasing by less than 50% at room temperature. AlGaN QDs in wires present IQE > 50% and stable as a function of the pumping power density, more than QWs.

Figure 46 compares the variation of the PL with temperature (low injection conditions) in GaN/AlN samples (E3857) and AlGaN/AlN samples (E3863). In both cases the PL remains approximately stable up to 100 K, followed by a drop of intensity that is more important in the case of AlGaN. Figure 46(c) depicts the integrated luminescence intensity from E3863 as a function of the

inverse temperature measured both by PL and CL, showing that there is no significant difference between the two measuring techniques. With this, we can extract an $IQE \approx 22\%$ for E3865, emitting at 258 nm and $IQE \approx 44\%$ for sample E3863, emitting at 286 nm using either CL or PL.

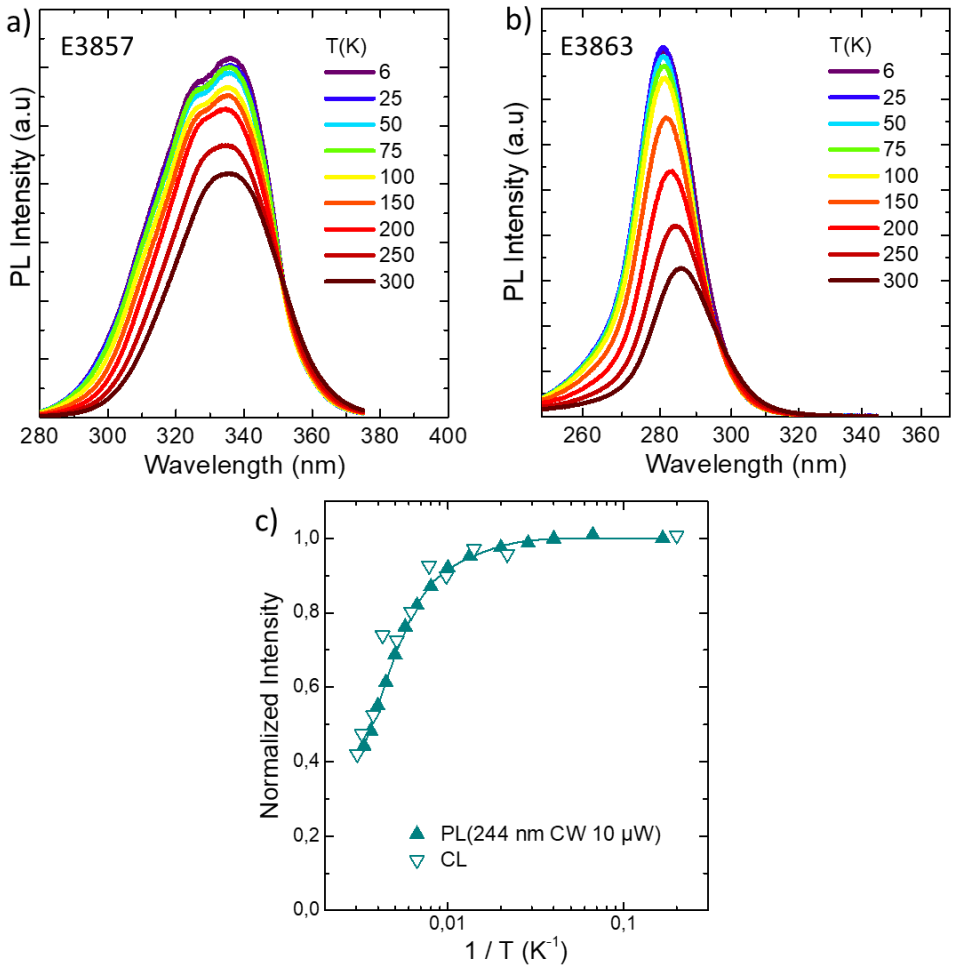

Figure 46. PL spectra measured under continuous wave excitation, with temperature (5 K – 300 K) for samples a) E3857 and b) E3863 emitting at 340 nm and 286 nm, respectively. The higher drop in intensity for E3863 at high temperatures is consistent with the presence of Al in the dots, as compared to the GaN dots in E3857 presenting better IQE (as listed in Table 9). c) Variation of the integrated PL intensity of E3863, and the integrated CL intensity of E3863 as a function of the inverse temperature, normalized to their value at low temperature. The solid line is a fit to 1/[1 + A exp(-E_a/(kT))], where E_a is a thermal activation energy, kT is the thermal energy, and A is a fitting constant (E_a = 48±4 meV and A = 7±2).

4.3.2 Cathodoluminescence

Cathodoluminescence measurements of all the samples in this series were performed in a CL-SEM. The normalized room-temperature emission from the GaN/AlN NW samples (E3898, E3861, E3862 and E3918) is displayed in Figure 47 (green spectra), and the peak emission wavelength is summarized in Table 9. The emission ranges from 340-336 nm, for samples E3857-E3898, to 265-277 nm for samples E3918-E3864. However, there is a monotonous decrease of the IQE at room temperature that follows the blue shift. Measurements in the low-injection regime, gives an IQE shift from 63% to about 30%, as illustrated in the inset of Figure 47. By incorporating aluminum in the dots, we get an additional blue shift in the emission, as is seen in Figure 47 (pink spectra). With 10% Al in the dots, the room temperature emission is mainly dominated by one spectral line which is tuneable

in the range of 331 nm (E3858, well thickness: 1.5 nm) to 258 nm (E3865, well thickness: 0.65). One can observe the decrease of the IQE values, as it is with the GaN dots, along with an increase in the relative linewidth as a function of the blue shift (ref. Figure 47). On the other hand, when comparing $Al_{0.1}Ga_{0.9}N$ dots emitting at the same wavelength as the GaN dots, the IQE remains roughly constant (seen in inset of Figure 47). This study proves that the addition of Al in the dots does not result in any significant degradation of the optical properties of these heterostructures.

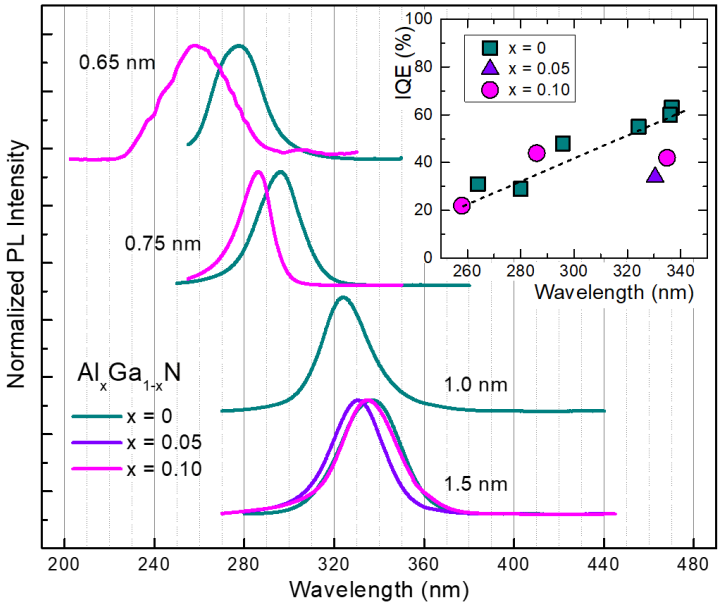

Figure 47. Room-temperature emission of the AlGaN dots in wires under study normalized to their maxima. The thickness of the AlGaN wells is indicated in the figure. The spectra are vertically shifted for clarity. The spectra from samples with 0.65 nm wells were measured by CL. The rest of the spectra were obtained from PL measurements. Inset: Variation of the IQE as a function of the peak emission wavelength. Different colours represent different Al content in the wells. The dashed line is only for guidance of the eyes.

4.3.3 Stability under electron pumping

Charging and stability issues have been encountered and reported for electron pumping in NWs due to the accumulation of charges and trapping on the surface [141,151–153]. This, in turn, degrades the emission and hinders with results [152,153]. Reduced quenching of CL emission was reported in the case of NWs by the addition of an AlN shell [122].

We conducted stability studies on our samples by measuring the evolution of the CL intensity with time. These studies were performed at room temperature, keeping a constant acceleration voltage V_A of 5 kV. The injected current was 25 pA and the beam was directed at the sample with a beam-spot diameter of 20 nm (giving an excitation power density of around 8 kW/cm^2 at the contact point). The results of these studies can be seen in Figure 48. It includes the evolution of the emission of samples E3889G and E3857 for a period of 300 seconds (5 minutes) under constant pumping. In contrast to the previous literature I mentioned (refs. [152,153]), we did not observe any notable degradation of the CL emission intensity. We could attribute the stability of these samples to the relatively thick AlN shell that surrounds the QDs, which could cause them to be insensitive to recombinations on the NW surface.

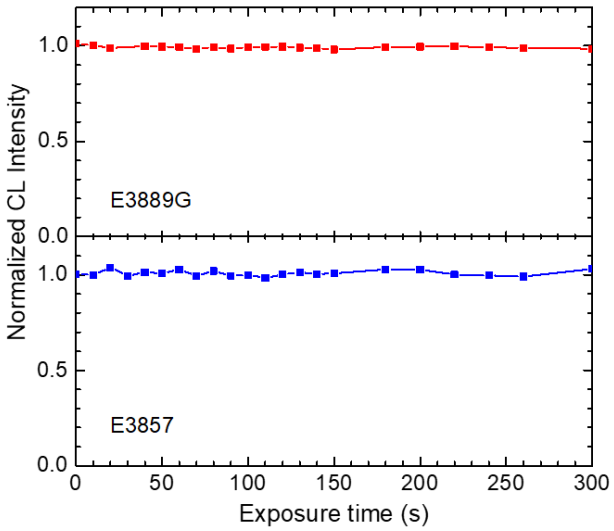

Figure 48. Evolution of the CL intensity as a function of time, measured with V_A = 5 kV and an injection current of 25 pA directed in a 20 nm beam spot.

Before performing deeper studies with CL, it is important to know that the CL emission also remains stable under the influence of varying electron beam currents. For this purpose, an electron gun operated in direct current mode, under normal incidence, with a beam spot diameter of 4±1 mm was used on the sample E3857. The acceleration voltage, V_A, was kept at 5 kV and the injected current was varied. As is clear from Figure 49, the integrated emission of the sample scales linearly with an increasing current showing no indication of saturation up to 400 µA of injected current. Therefore, we could safely move on to further studies without saturation issues.

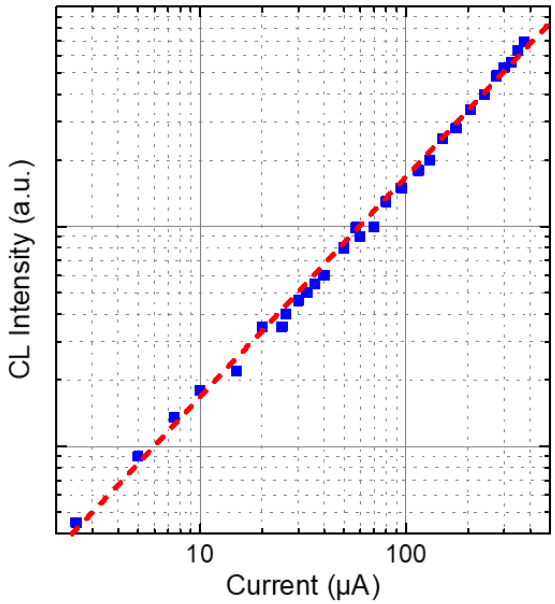

Figure 49. Evolution of the CL intensity for sample E3857 as a function of injected current in the sample. Measurements were performed using an electron gun operated in direct current mode, under normal incidence, with a beam spot diameter of 4±1 mm with a fixed V_A = 5 kV

4.3.4 Penetration depth and efficiency under electron pumping

Figure 50 (a) presents Monte Carlo simulations of the electron penetration depth in an $Al_xGa_{1-x}N$ layer with same average aluminium mole fraction as the active region of samples E3889G and E3857.

Keeping in mind that the SL thickness is about 400 nm, an acceleration voltage higher than 7.5 kV is necessary to inject carriers into the underlying GaN. However, the reduced material density in the nanowire samples should result in an enhancement of the electron penetration depth. To study the penetration depth of the electron beam experimentally, sample E3857 (and others) were characterized by CL as a function of the V_A or acceleration voltage (excitation normal to the surface in the SEM). The emission spectra are dominated by a line around 340 nm, assigned to carrier recombination in the quantum dot SL. The emission from the stem becomes visible for acceleration voltages above 5.5 kV, which points to a higher penetration depth in comparison with planar layers, which is justified by the reduced average material density in the nanowire ensemble.

The evolution of the CL intensity as a function of the acceleration voltage, V_A, was studied using an electron gun operated in direct current mode, under normal incidence, with a beam spot diameter of 4±1 mm. Measurements were performed with an injection current of 100 µA. Figure 50 (c) depicts the result for the nanowire sample E3857, showing that the maximum CL intensity is attained for $V_A \approx$ 5.5 kV, which is consistent with the penetration depth estimated from Figure 50 (b). Accordingly, a decrease of the emission efficiency is observed for $V_A >$ 5.5 kV [see Figure 50 (c)].

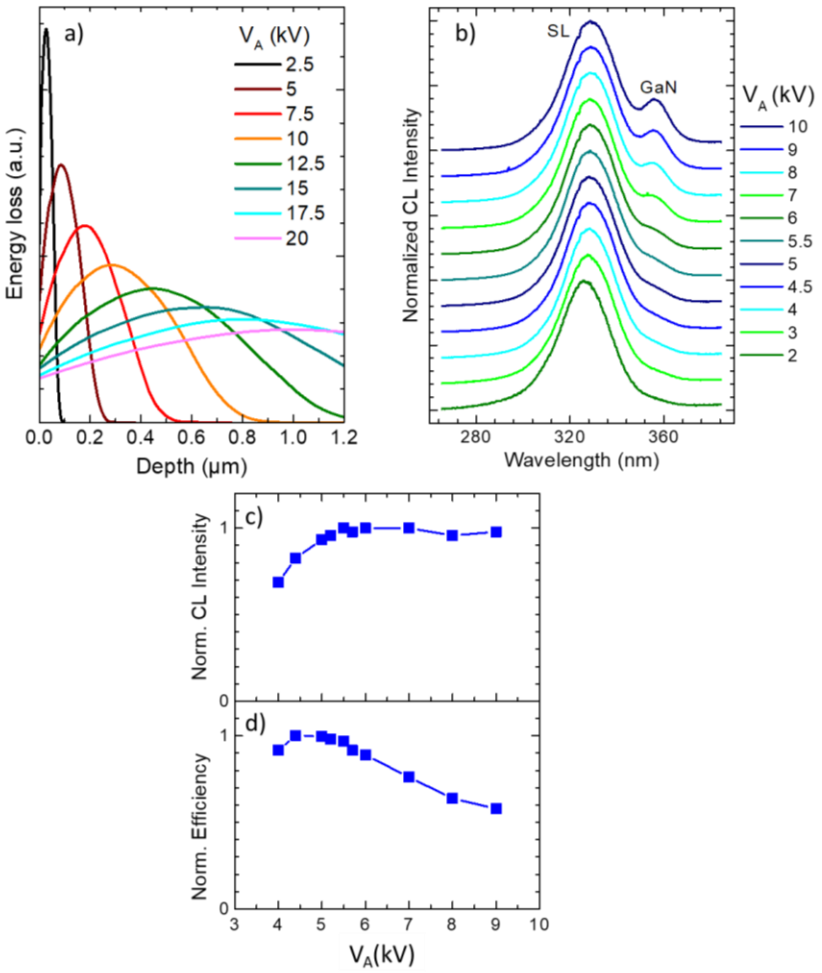

Figure 50. a) Monte Carlo simulation of the electron trajectory for AlN. (b) CL measurements of sample E3857 as a function of the acceleration voltage, V_A. Spectra are normalized at the peak value and vertically shifted for clarity. The emissions from the QD/well SL and from GaN are identified. (c) Normalized CL intensity and (d) emission efficiency as a function of V_A for sample E3857. Measurements were performed using an electron gun operated in direct current mode, under normal incidence, with a beam spot diameter of 4±1 mm.

We performed preliminary measurements of the EQE for some of the NW samples listed in Table 4.1. For these studies, we excited the samples with a pulsed Nd-YAG laser (λ = 266 nm, 2 ns pulses, repetition rate of 8 kHz) at two different levels of pumping power, namely 100 µW and 50 µW to ensure the results are consistent at low as well as high pumping power. The optically pumped samples were placed in an IE385836A-4 Thorlabs 2" integrating sphere, as shown in Figure 51. The emitted light is collected by an SM05P Thorlabs UV photodetector. The measured signal obtained by exciting the sample was then compared to that of the measurement obtained by replacing the sample with a full reflector. Measurements were performed on samples E3857, E3859, E3858, E3862, E3863, E3881, E3899, E3901, and E3911. The results give an average EQE = 3.42±0.55%, independent of the pumping power.

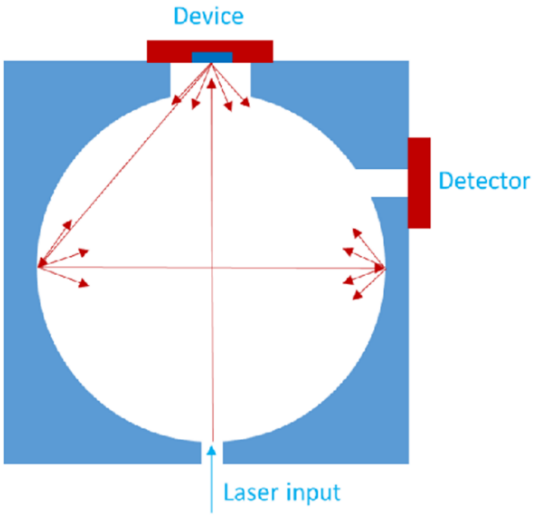

Figure 51. Set-up for EQE measurements with an integrating sphere with reflecting walls, under a pulsed excitation mode.

4.4 Conclusions

In summary, we have studied the eligibility of NW arrays as active media for electron-pumped UV emitters. The design of the heterostructures involves a 400-nm-long $Al_xGa_{1-x}N$/AlN ($0 \le x \le 0.1$) QD superlattices grown on self-assembled GaN NWs by PAMBE on n-type Si(111) wafers. The $Al_xGa_{1-x}N$ sections were grown under N-rich conditions and the AlN sections under stoichiometric conditions, to obtain homogeneous QDs with throughout the SL. The emission of these NWs were then compared with that of planar samples with the same periodicity and thickness and observed that the NW structures are less sensitive to nonradiative recombination. This resulted in higher IQE (more than 60%) at room temperature, even under low injection conditions. With pulsed optical excitation, we concluded that the IQE remains stable for excitation power densities up to 50 kW/cm^2. Experiments under electron pumping show that the NW SL is long enough to collect the electron-hole pairs generated by an electron beam with an acceleration voltage V_A = 5 kV. By varying the dot/barrier thickness ratio and the Al content in the dots, we were able to tune the NW peak emission in the range of 340 to 258 nm. This work describes the first assessment of NWs for application in electron-pumped UV sources and our results confirm the feasibility of the approach. Electron channeling effects can be compensated by an increase of the active region length by ≈ 60% in comparison to planar layers. Application of QD superlattices as active media, it is possible to keep the homogeneity of the dot geometry all along the active region in order to obtain NW ensembles providing a single emission line in the deep UV range. Moreover, we have demonstrated the stability of the NWs under electron

pumping. Next steps should include an evaluation of the external quantum efficiency under electron pumping, lifetime in operation conditions, and x-ray emission. The results reported here are very promising for the fabrication of electron-pumped UV lamps, which could be applied in the field of disinfection and water purification.

5 AlGaN/AlN quantum dots

In this chapter, I talk about Stranski-Krastanov $Al_xGa_{1-x}N$/AlN QDs, starting with our motivation to work on these type of heterostructures for application as the active region of electron-beam pumped UV lamps. In terms of experimental results, I focus first on $Al_xGa_{1-x}N$/AlN ($0 \leq x \leq 0.1$) QD SLs grown to study the optical performance in accordance to the varying III/V ratio during the growth process. Here, the target was to attain peak emission at 270 nm. Then, a second series was grown to study the optical performance by changing the Al content in the QDs, aiming at peak emission at shorter wavelengths. I describe the growth by PA-MBE of the 530-nm-thick superlattices (100 periods) of QDs. TEM, XRD and AFM studies was performed to extract structural information. The emission spectra was recorded with optical excitation as well as under electron pumping. The internal quantum efficiency was characterized at low to high injection ranges to provide information on non-radiative processes, and to emulate carrier injection in operation conditions. Power efficiency measurements were conducted by studying the angular distribution of UV emission.

The growth, AFM, XRD, SEM, NextNano³ simulations and optical analysis with PL and CL were performed by me. I also travelled several times to Lyon, to make CL measurements with electron gun was performed with the set-up of Prof. Stephen T. Purcell at ILM, Université de Lyon. The TEM images were provided by Catherine Bougerol and Adeline Grenier. The Monte Carlo simulations of electron trajectories were provided by Ioanna Dimkou. The XRD measurements were performed with the help of Edith Bellet-Amalric. The work was coordinated by Eva Monroy.

This work on the first series has been published as "**Internal quantum efficiency of AlGaN/AlN quantum dot superlattices for electron-pumped ultraviolet sources**", A Harikumar *et al* 2020 Nanotechnology 31 505205 (2020) [65].

5.1 Introduction and motivation

In addition to the nanowire heterostructures described in chapter 4, I considered another type of nanostructure for the fabrication of electron beam pumped UV emitters, namely QD superlattices. There is an important advantage of working with QDs: the three-dimensional carrier localization in the dots provide an enhancement of the emission yield at room temperature [62,63,115,154,155], which has motivated research on QDs for the development of high efficiency UV emitters [64,156–160]. We use plasma-assisted molecular beam epitaxy (MBE) for the growth, as it is known to produce layers of close-packed Stranski-Krastanov (SK) GaN QDs with high IQE [62,156,157]. Prior to this work, we have reported $Al_{0.1}Ga_{0.9}N$/AlN QDs emitting at wavelengths as short as 235 nm at room temperature with internal quantum efficiency $IQE \approx 30\%$ [156]. Previous PhD students have also demonstrated $Al_{0.1}Ga_{0.9}N$/AlN QDs with IQE higher than 50% in the 276-296 nm spectral range, but with high sensitivity to the amount of AlGaN in the QD layer [64]. Thus, the response was maximum for a deposition of 4-5 ML of AlGaN, but it dropped severely for higher or lower amounts.

Most viruses and bacteria experience photochemical changes to the nucleic acids when exposed to UV radiation, which damages their ability to reproduce [161]. The spectral response of pathogens to UV light, presented in Figure 52, shows two maxima located around 270 nm and 220 nm. The most common UV sources for disinfection are low-pressure mercury lamps [162], emitting at 253.7 nm with a power efficiency of about 20%. However, there is an international concern about the use of mercury, and the manufacture and export of mercury-containing products is subject to increasingly strict regulations. It is hence important to develop an alternative solid-state technology to replace the mercury lamp, trying to tune the emission peak to 270 nm, i.e. the spectral region that is more efficient for disinfection.

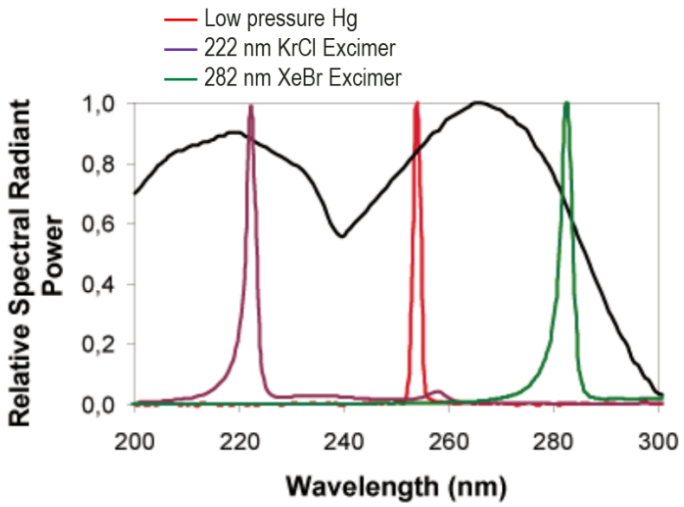

Figure 52. The response of pathogens to UV light and the current solutions, low pressure Hg lamp and excimer lamps, to tackle them. There are two maximums: around 270 nm range and 220 nm (image taken from: https://www.ushio.co.jp/en/technology/lightedge/).

On the other hand, recent studies have shown that the second disinfection peak at 220 nm might be also interesting. Radiation at 250-270 nm is highly carcinogenic and cataractogenic, thus representing a serious health hazard [163]. Recently, it has been demonstrated that far-UVC emission in the 220-230 nm range can efficiently inactivate bacteria without harm for humans [6], since it cannot penetrate the outer (non-living) layers of human skin or eyes, as schematically represented in Figure 53. The 222 nm range UV rays does not penetrate the epidermis of humans. In the same way, the 222 nm rays do not penetrate aqueous humor of the human eye and get absorbed without damaging the cornea [164].

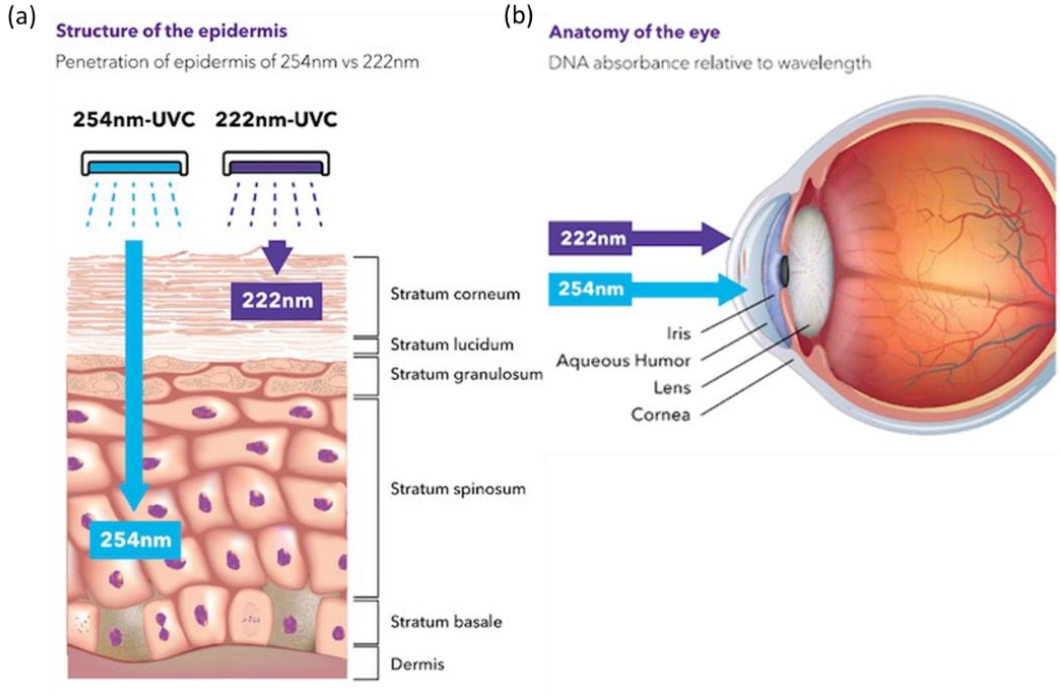

Figure 53. (a) Comparison of the penetration of UV light emitting at 254 nm and 222 nm in the epidermis of human body. The 222 nm rays do not penetrate the surface of the skin, while the 254 nm rays do. (b) Similarly, for the eyes, the 222 nm emission gets absorbed in the cornea while the 254 nm penetrates the aqueous humor and potentially damages it (Image courtesy: https://blooloop.com/technology/in-depth/far-uvc-technology-attractions-covid-19/).

LEDs based on AlGaN semiconductors and emitting at 270 nm have been pushed as a replacement for mercury lamps [39], as they are non-toxic, their emission is spectrally tunable to more efficient disinfection wavelengths, and they exhibit long lifetime and fast switching capabilities. However, despite there being a plethora of research in III–V LEDs, their performance is still not at the level of mercury arc lamps, and commercial devices exhibit power efficiencies lower than 1%. This limited performance is due to a variety of factors, such as the difficulty to obtain UV transparent AlN substrates, and the high resistivity of contacts and doped regions (particularly in the p-type layers, which is partially solved today by incorporating a UV-absorbing layer of Mg-doped GaN in the structure degrading the light extraction efficiency). These issues become even more severe at shorter wavelengths. LEDs emitting at 222 nm are not commercially available and their EQE in the laboratory is below 0.1% [39].

As mentioned in chapter 2, the drawbacks of UV LEDs can be solved with electron-pumped UV lamps. To analyze this possibility, in the first part of this chapter, our target was to attain highly efficient emission at 270 nm using $Al_xGa_{1-x}N$/AlN Stranski-Krastanov (SK) QDs. We explored the effect of the III/V ratio during the deposition of AlGaN QDs on their optical properties, obtaining QDs emitting in the range of 260 to 320 nm. In the second part of the chapter, we explored the effect of tuning the Al content while keeping the III/V ratio constant, obtaining QDs emitting at shorter wavelengths. The QDs were characterized to study their structural and optical properties. IQE values were calculated as a function of the optical pumping power, covering low excitation densities revealing the material properties in terms of non-radiative processes, and high excitation densities, which emulates carrier injection in operation conditions. In the case of electron-beam pumping, the variation of the efficiency as a function of the acceleration voltage and injection current is also discussed. We also studied the stability of these dots as a function of time, as well as varying currents. Finally, WPE values were calculated with angular measurements under CL pumping to prove the eligibility of these heterostructures for the final device.

5.2 QDs with target wavelength: 270 nm

5.2.1 Design and growth conditions

In order to study the advantages of using $Al_xGa_{1-x}N$/AlN Stranski-Krastanov (SK) QDs as the active region for electron-pumped UV emitters, we synthesized samples consisting of a stack of 100 layers of self-assembled $Al_xGa_{1-x}N$ QDs with x = 0 or 0.1, separated by 4 nm of AlN as barrier. Such QD superlattices were grown using plasma-assisted MBE on 1-µm-thick (0001)-oriented AlN-on-sapphire templates (as mentioned in section 3.1.1) at a temperature T_S = 720°C. The growth process was monitored by reflection high-energy electron diffraction (RHEED). The active nitrogen flux, Φ_N, was tuned to achieve a growth rate $\nu_{\mathrm{Ga}} = \Phi_{\mathrm{N}}$ = 0.52 monolayers/s (ML/s) under metal rich conditions. Note that 1 monolayer (ML) of AlN or GaN is 0.25 nm. The $Al_xGa_{1-x}N$ dots were grown using N-rich conditions, which are known to lead to a high density of small QDs [62–64,100]. The small size of the dots should prevent vertical correlation, which is known to lead to an increase of the QD size along the superlattice, with the resulting red shift of the emission [165]. We explored the effect of varying the Ga flux (i.e. the gallium-to-nitrogen flux ratio) in the range of Φ_{Ga} = 0.149-0.441 ML/s ($\Phi_{\mathrm{Ga}}/\Phi_N$= 0.29-0.85), keeping the Ga deposition time constant (12 s). In the case of ternary $Al_xGa_{1-x}N$ QDs, we added a flux of aluminium Φ_{Al} so that the targeted Al mole fraction in the dots is $x = \Phi_{\mathrm{Al}}/(\Phi_{\mathrm{Al}} + \Phi_{\mathrm{Ga}})$. The deposition of the QDs was followed by a growth interruption of 15 s. At the end of this process, a spotty RHEED pattern confirmed the presence of QDs. To favour the charge evacuation during the electron pumping process, the QDs were doped n-type with [Si] = 5×10^{18} cm^{-3}

(value estimated from Hall effect measurements using the Van der Pauw method on planar Si-doped GaN layers). This type of doping with of silicon during the growth process does not have any effect on the growth kinetics or in the resulting QD shape/density [100]. The AlN sections were grown under Al-rich conditions ($\Phi_{\mathrm{Al}}/\Phi_N$ = 1.1), followed by a growth interruption under nitrogen to consume the accumulated excess of Al. At the end of the growth of each AlN barrier, the RHEED pattern showed the straight lines, which is characteristic of a planar surface. The growth process was sharply interrupted (the precursor fluxes were shuttered, and the substrate was rapidly cooled down) after the deposition of the last QD layer, to enable optimal AFM characterization of the QD shape and density. A schematic description of the general structure is depicted in Figure 54 and a summary of the samples under study is presented in Table 10.

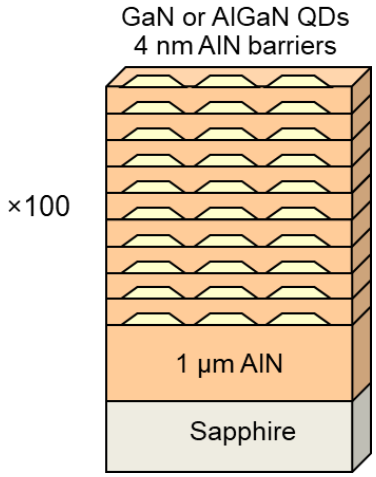

Figure 54. Simplified schematic of the QD SL structure consisting of 100 periods of QDs (about 1 nm) and 4 nm of AlN barrier [65].

Sample	Φ_{Ga} (ML/s)	Φ_{Al} (ML/s)	$\Phi_{\mathrm{Metal}}/\Phi_N$	Number of MLs	x	Peak emission (nm)	FWHM (nm)	IQE (%)	E_a (meV)
E3942	0.441	0	0.85	5.3	0	335	24	35	55±8
E3960	0.380	0	0.73	4.6	0	329	28	50	65±6
E3958	0.319	0	0.61	3.8	0	310	35	51	66±5
E3943	0.306	0	0.59	3.7	0	316	18	61	74±7
E3945	0.220	0	0.42	2.6	0	294	32	50	46±5
E3957	0.211	0	0.41	2.5	0	294	28	50	49±7
E3959	0.149	0	0.29	1.8	0	250	16	43	100±40
E3962	0.380	0.038	0.80	5.0	0.1	312	19	52	78±13
E3963	0.319	0.032	0.68	4.2	0.1	298	21	54	70±10
E3964	0.220	0.022	0.47	2.9	0.1	270	22	47	68±7
E3965	0.149	0.015	0.32	2.0	0.1	**244**, 277	15	33	68±14

*Table 10. Growth parameters and optical characteristics of the samples under study: Ga and Al fluxes in monolayers per second ($\Phi_{Ga}$and Φ_{Al}, respectively), metal-to-nitrogen ratio (Φ_{Metal}/Φ_N), number of monolayers deposited for the generation of each QD layer, nominal Al concentration in the dots (x), peak emission wavelength at room temperature (in the case of multiple peaks, the dominant peak appears in **bold** fonts), full width at half maximum (FWHM) of the main emission line at room temperature, internal quantum efficiency (IQE) at room temperature measurement under low-injection conditions, and activation energy (E_a) of the main nonradiative process extracted from variation of the PL intensity as a function of temperature.*

5.2.2 Structural characterization

The structural properties of the QD superlattices were characterized using:

- XRD, which is used to estimate the strain state and the SL period.
- AFM, which allows us to estimate the QD density and measure the QD height above the wetting layer.
- TEM, which provides a view of the total height QD+wetting layer and an estimation of the QD diameter.

Combining all this information, we get a view of the shape of these nanostructures, beyond the limits of each individual technique.

Starting with XRD, Figure 55 shows typical reciprocal space maps and θ–2θ diffractograms. In the reciprocal space map around the (10-15) reflection, depicted in Figure 55(a) for sample E3945, we can identify the reflection from the AlN substrate and the satellites of the QD superlattice (SL), which are vertically aligned. The satellites and the AlN reflection present the same in-plane reciprocal vector, $Q_x = -2/(a\sqrt{3}) = -3.710$ nm^{-1}, where a is the in-plane lattice parameter of AlN. This is an indication of pseudomorphic growth, where the mismatch stress is elastically released. Note that for this reflection, the out of plane reciprocal vector is $Q_z = 1/(5c)$, where c is the out of plane lattice parameter. The period of the structures was extracted from the inter-satellite distance in a θ-2θ scan around the (0002) reflection of AlN, as shown in Figure 55(b) for 3 $Al_{0.1}Ga_{0.9}N$/AlN QD samples grown with different metal-to-nitrogen flux ratio (E3962, E3963, and E3964), and a GaN/AlN QD superlattice (E3945). The large number of satellites reveals the high quality of the samples even after the growth of 100 QD layers. In the figure, the experimental results are compared with a theoretical calculation using the Rigaku SmartLab Studio II software. The calculation assumes a period of 5.43 nm and that the average out of plane lattice parameter of the QD superlattice is that of $Al_{0.90}Ga_{0.10}N$ fully strained on AlN.

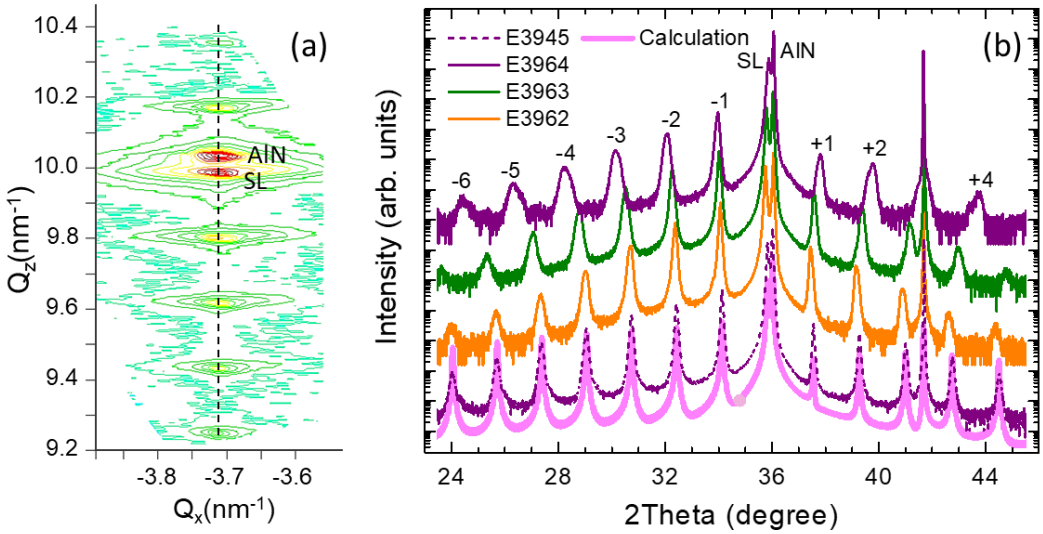

Figure 55. (a) Schematic description of the QD superlattices under study. (b) Reciprocal space map around the (10-15) reflection of sample E3945. Labels indicate the reflection of AlN and the main reflection of the QD superlattice (SL), which appear vertically aligned. (c) XRD θ-2θ scans of samples E3962, E3963 and E3964 recorded around the (0002) reflection of AlN. The scans are vertically shifted for clarity. Labels indicate the (0002) reflection of AlN and the QD superlattice (SL) with several satellites. The peak around 41.7° corresponds to the (0006) reflection of the sapphire template [65].

Looking at the E3962-E3963-E3964 series, we observe that the satellites become more separated in angle when decreasing the III/V ratio. This is due to the fact that the deposition time is constant (15 s), and so the amount of AlGaN deposited to form the QDs decreases for decreasing III/V ratio. The total amount of material deposited (in monolayers) is indicated in Table 10. From the XRD data, we deduce that the SL period decreases from 5.45 nm for E3962 to 5.25 nm for E3963 and 4.78 nm for E3964, which is consistent with the variation of the amount of AlGaN deposited in the QDs (let's remind here that 1 ML ≈ 0.25 nm).

XRD does not give any information about the QD shape. Therefore, the morphology of the topmost QD layers was analysed by AFM, with the result presented in Figure 56 for samples E3964 (GaN/AlN QDs) and E3962 ($Al_{0.1}Ga_{0.9}N$/AlN QDs). In such images, the QD density is $(3.3\pm0.4)\times10^{11}$ cm^{-2} and $(4.6\pm0.5)\times10^{11}$ cm^{-2}, respectively, and the height of the dots is about 0.46±0.20 nm and 0.64±0.25 nm, respectively, i.e. approximately 2-3 ML. Note that these values should correspond to the QD height above the wetting layer.

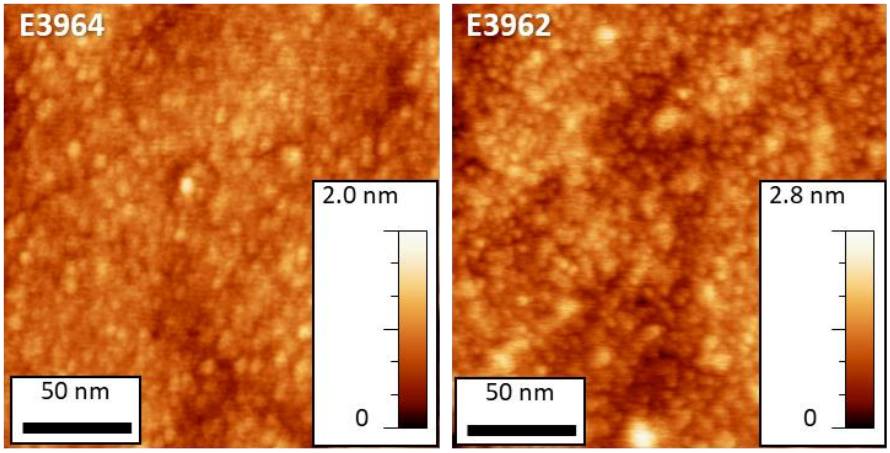

Figure 56. AFM images of samples E3964 and E3962 [65].

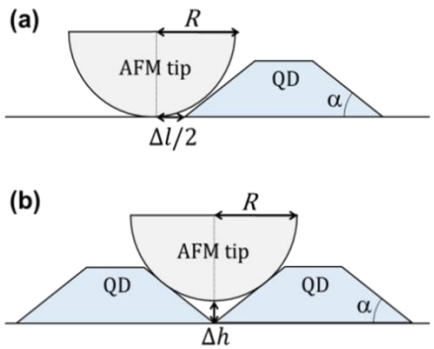

Figure 57. (a) Perceived increase of lateral dot size compared to the real dot size in the case of a low density of dots. (b) Perceived decrease of the dot height in the case of high density of dots.

In the case of high-density (close to 10^{12} cm^{-3}) QDs, as the samples presented here, the measurement of the QD density is reliable, but it is difficult to extract reliable measurements of the QD geometry from AFM. The dimension of the AFM tip is comparable to the dimension of the dots, and deconvolution of the effect of the AFM tip would require precise knowledge of the tip shape, as explained in Figure 57. Assuming a QD density of 5×10^{11} cm^{-2} and a hexagonal close-packed QD distribution, the distance between QDs would be around 11 nm, which is in the range of the expected QD diameter. Therefore, we would be close to the situation described in Figure 57(b), which leads to an underestimation of the QD height.

To further assess the QD geometry, samples E3960, E3962 and E3964 were analysed using cross-section HAADF-STEM and HRTEM, with the results presented in Figure 58. The QDs are clearly resolved, with facets that form an angle of ≈32° with the (0001) plane. The images confirm that the in-plain locations of the QDs are not vertically correlated. The QD base diameter is 6.9±1.0 nm, 6.2±1.0 nm and 6.5±1.0 nm, and the QD height (including wetting layer) is 5±1 ML, 5.5±1.0 ML and 4±1 ML, for samples E3960, E3962 and E3964, respectively. In addition, the wetting layer thickness is estimated at 2 ML, 2-3 ML and 1-2 ML for E3960, E3962 and E3964, respectively. The average values and error bars were extracted by analysing images of at least 10 QDs per sample. In terms of QD height, the results are consistent with AFM measurements. Comparing the results of E3960 (GaN/AlN QDs) and E3962 ($Al_{0.1}Ga_{0.9}N$/AlN QDs), grown with the same Ga flux, we conclude that the additional Al flux in E3962 does not introduce a significant distortion of the QD morphology. In the case of E3964, the metal fluxes are reduced by approximately a factor of two with respect to E3962, keeping the same Al/Ga ratio. As a result, the QD height reduces drastically, but the diameter of the dots remains approximately constant. This observation points to a temperature-limited QD diameter, i.e. the diameter is given by the adatom diffusion length, which is determined by the substrate temperature.

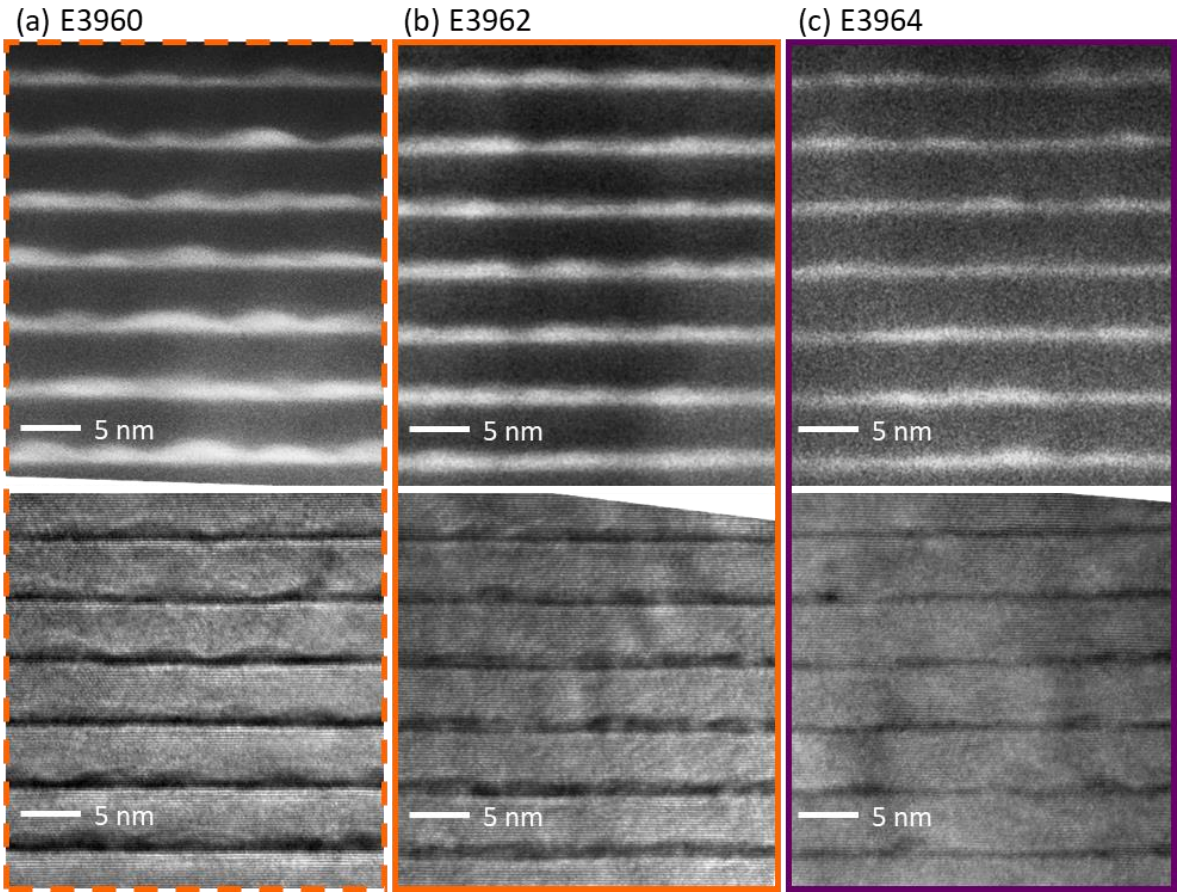

Figure 58. Top: HAADF-STEM images of samples (a) E3960, (b) E3962 and (c) E3964 showing 6-7 periods of the GaN/AlN quantum dot superlattice. Dark/bright contrast corresponds to Al-rich/Ga-rich areas. Bottom: HRTEM off-axis (10° tilt from the [11-20] zone axis) images of the same samples. Here bright/dark contrast corresponds to Al-rich/Ga-rich areas. The colour code is associated with the sample and is consistent along the chapter [65].

At this point, combining the measurement of the SL period by XRD, the QD density by AFM and the QD base diameter and height, and the thickness of the wetting layer by TEM, we have a complete description of the QD geometry.

5.2.3 Spectral behavior

To study the optical performance of the QDs, we recorded and compare the CL emission of the various samples in Table 10 (shown in Figure 59). The measurements presented here were recorded in an FE-SEM set-up with the accelerating voltage fixed at 5 kV. Solid(dashed) lines represent $Al_{0.1}Ga_{0.9}N$(GaN) QDs, and the spectra are vertically shifted, keeping together samples that were grown with the same gallium flux, decreasing from Φ_{Ga}= 0.380 ML/s (bottom) to 0.149 ML/s (top). A blue shift is observed in the peak emission wavelengths of $Al_{0.1}Ga_{0.9}N$ dots as compared to GaN dots with the same Φ_{Ga}. The shift corresponds to an average increase of 250 meV in band gap, which is consistent with the incorporation of 10% of Al in the dots. The peak emission wavelength (λ) of the samples under study and the emission full width at half maximum (FWHM) are summarized in Table 10. The peak emission can shift from 335 to 250 nm for GaN/AlN QDs and from 312 to 244 nm for $Al_{0.1}Ga_{0.9}N$/GaN QDs. This means that it is possible to obtain a peak emission at the targeted 270 nm wavelength for disinfection. Note that the emission relative linewidth, defined as FWHM/λ, remains in the range of 6-11% for all samples.

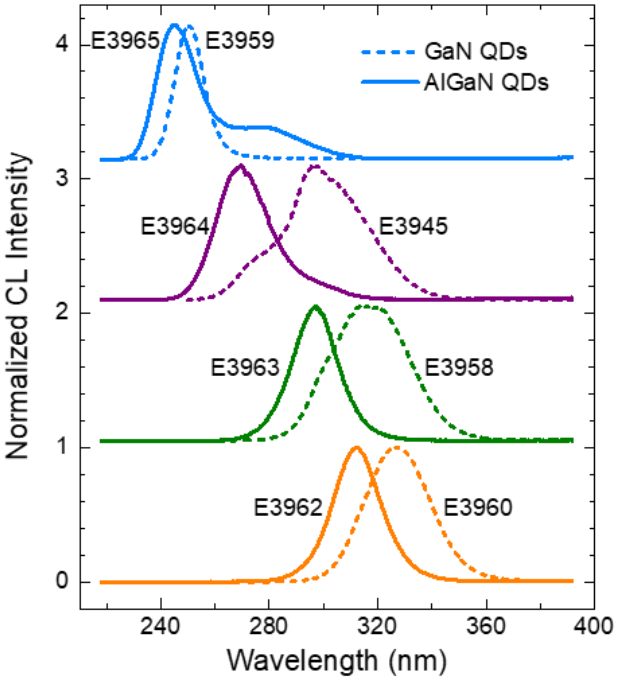

Figure 59. Room-temperature CL emission from GaN/AlN (dashed) and $Al_{0.1}Ga_{0.9}N$/AlN quantum dot superlattices grown with different fluxes of gallium (from bottom to top, Φ_{Ga}= 0.380, 0.319, 0.220, and 0.149 ML/s). The spectra are normalized to their maxima and vertically shifted for clarity [65].

5.2.2 Band profile simulations

To evaluate the agreement of the experimental emission wavelength with theoretical expectations, and to analyse the sensitivity of the emission to fluctuations in structural parameters, we have performed 3D simulations of the strain distribution, band diagram and quantum confined levels of E3960, E3962 and E3964, using the structural characterization data as input parameters. The computed values of ε_{xx}, ε_{zz}, $\varepsilon_{zz}/\varepsilon_{xx}$, the band gap, and the resulting e_1-h_1 transition energy and emission wavelength for the nominal E3962, E3960, and E3964 structures and several structural variations are listed in Table 11, Table 12 and Table 13, respectively. Using nominal parameters, i.e. the wetting layer thickness, QD height and base diameter extracted from TEM and the nominal Al

composition, we obtain theoretical transition wavelengths of 309±5 nm, 322±8 nm, and 287±8 nm, respectively. Note that H-1, H+1, D-1, D+1 mean nominal height-1 ML, nominal height+1 ML, nominal diameter-1 ML and nominal diameter+1 ML, respectively. Al-1 and Al+1 mean 1% Al less or more than the nominal Al content (10%). These values are in good agreement with experimental values (329 nm, 312 nm, and 270 nm, respectively). The larger deviation in the case of E3964 is due to the fact that the model is reaching its validity limits, since the QDs are only 4 ML high, so that a fluctuation of thickness of 1 ML corresponds to 25% of the height.

Simulation	QD height (ML)	QD diameter (nm)	WL thickness (ML)	x	ε_{xx} (%)	ε_{zz}, (%)	$\varepsilon_{zz}/\varepsilon_{xx}$	E_G (eV)	e_1-h_1 (eV)	λ (nm)
Nominal	**5.5**	**6.2**	**2.5**	**0.10**	**-1.16**	**-0.016**	**0.010**	**3.944**	**4.001**	**309.9**
H-1	4.5	**6.2**	**2.5**	0.10	-1.75	0.30	-0.170	3.930	4.041	306.8
H+1	6.5	**6.2**	**2.5**	0.10	-1.44	-0.36	0.247	3.960	3.992	310.6
D-1	**5.5**	5.2	**2.5**	0.10	-1.45	-0.23	0.159	3.954	4.091	303.1
D+1	**5.5**	7.2	**2.5**	0.10	-1.67	0.12	-0.075	3.939	3.928	315.7
H-1D-1	4.5	5.2	**2.5**	0.10	-1.67	0.14	-0.086	3.936	4.113	301.5
H+1D-1	6.5	5.2	**2.5**	0.10	-1.35	-0.58	0.432	3.973	4.091	303.1
H-1D+1	4.5	7.2	**2.5**	0.10	-1.79	0.39	-0.217	3.927	4.013	309.0
H+1D+1	6.5	7.2	**2.5**	0.10	-1.54	-0.16	0.106	3.952	3.903	317.7
Al-1	**5.5**	**6.2**	**2.5**	0.09	-1.61	-0.016	0.010	3.919	3.978	311.7
Al+1	**5.5**	**6.2**	**2.5**	0.11	-1.58	-0.015	0.009	3.970	4.025	308.1

*Table 11. Simulations based on the structure of E3962 (experimental emission wavelength = 312 nm). Input structural parameters include QD height, QD base diameter, wetting layer (WL) thickness and Al mole fraction (x) in the dots and in the WL. Nominal values are marked in **bold**. As relevant output data, we collect here the in-plane and out-of-plane strain (ε_{xx} and ε_{zz}, respectively) at the point of the maximum of the electron wavefunction, as well as the $\varepsilon_{zz}/\varepsilon_{xx}$ ratio and the resulting band gap (E_G) at the same point, the energy difference between the first electron level (e_1) and the first hole level (h_1), and the corresponding expected emission wavelength (λ).*

Simulation	QD height (ML)	QD diameter (nm)	WL thickness (ML)	x	ε_{xx} (%)	ε_{zz} (%)	$\varepsilon_{zz}/\varepsilon_{xx}$	E_G (eV)	e_1-h_1 (eV)	λ (nm)
Nominal	**5.0**	**6.9**	**2.0**	**0**	**-1.88**	**0.15**	**-0.078**	**3.678**	**3.818**	**324.8**
H-1	4.0	**6.9**	**2.0**	0	-2.03	0.52	-0.256	3.663	3.912	317.0
H+1	6.0	**6.9**	**2.0**	0	-1.74	-0.10	0.057	3.691	3.770	328.9
D-1	**5.0**	5.9	**2.0**	0	-1.81	0.07	-0.042	3.684	3.928	315.7
D+1	**5.0**	7.9	**2.0**	0	-1.93	0.25	-0.129	3.674	3.769	329.0
H-1D-1	4.0	5.9	**2.0**	0	-1.98	0.41	-0.209	3.667	4.005	309.6
H+1D+1	6.0	7.9	**2.0**	0	-1.18	0.50	-0.273	3.685	3.730	332.4

*Table 12. Simulations based on the structure of E3960 (experimental emission wavelength = 329 nm). Input structural parameters include QD height, QD base diameter, wetting layer (WL) thickness and Al mole fraction (x) in the dots and in the WL. Nominal values are marked in **bold**. As relevant output data, we collect here the in-plane and out-of-plane strain (ε_{xx} and ε_{zz}, respectively) at the point of the maximum of the electron wavefunction, as well as the $\varepsilon_{zz}/\varepsilon_{xx}$ ratio and the resulting band gap (E_G) at the same point, the energy difference between the first electron level (e_1) and the first hole level (h_1), and the corresponding expected emission wavelength (λ).*

Simulation	QD height (ML)	QD diameter (nm)	WL thickness (ML)	x	ε_{xx} (%)	ε_{zz} (%)	$\varepsilon_{zz}/\varepsilon_{xx}$	E_G (eV)	e_1-h_1 (eV)	λ (nm)
Nominal	**4.0**	**6.5**	**1.5**	**0.1**	**-1.80**	**0.42**	**-0.232**	**3.925**	**4.307**	**287.9**
H-1	3.0	**6.5**	**1.5**	0.1	-1.9	0.66	-0.345	3.914	4.461	277.9
H+1	5.0	**6.5**	**1.5**	0.1	-1.7	0.13	-0.08	3.937	4.217	294.0
D-1	**4.0**	5.5	**1.5**	0.1	-1.7	0.288	-0.165	3.93	4.370	283.8
D+1	**4.0**	7.5	**1.5**	0.1	-1.8	0.5	-0.27	3.921	4.266	290.7
H-1D-1	3.0	5.5	**1.5**	0.1	-1.8	0.589	-0.312	3.917	4.505	275.3
H+1D+1	5.0	7.5	**1.5**	0.1	-1.7	0.251	-0.145	3.933	4.152	298.7
Al+1	**4.0**	**6.5**	**1.5**	0.11	-1.7	0.414	-0.232	3.952	4.33	286.4

*Table 13. Simulations based on the structure of E3964 (experimental emission wavelength = 270 nm). Input structural parameters include QD height, QD base diameter, wetting layer (WL) thickness and Al mole fraction (x) in the dots and in the WL. Nominal values are marked in **bold**. As relevant output data, we collect here the in-plane and out-of-plane strain ($\varepsilon_{xx}$and ε_{zz}, respectively) at the point of the maximum of the electron wavefunction, as well as the $\varepsilon_{zz}/\varepsilon_{xx}$ ratio and the resulting band gap (E_G) at the same point, the energy difference between the first electron level (e_1) and the first hole level (h_1), and the corresponding expected emission wavelength (λ).*

Using E3962 as a model structure, Figure 60 shows the perturbation of the electronic structure introduced by variations of the QD diameter and height. Figure 60(a) and (b) show the evolution of the electron square wavefunction in a QD located in the centre of the stack, as a function of the QD diameter (nominal and ±1 nm) and the QD height (nominal and ±1 ML). Note that the variations are introduced in such a way that the angle of the QD facets remains constant (≈ 32° with the base, as it corresponds to {10-13} planes). Due to the internal electric field, the electron is shifted towards the apex of the dot, which increases its sensitivity of the lateral confinement. Thus, laterally, the wavefunction spreads when increasing the QD diameter or decreasing the QD height, and it concentrates when reducing the QD diameter or increasing the QD height. Additionally, a vertical displacement of the wavefunction is clearly observed when varying the QD height. The magnitude of the displacement of the electron [0.43 nm between the extreme situations in Figure 60(b)] is identical (difference smaller than 0.2%) to the shift observed when varying the thickness of quantum well by the same amount (from 4.5 to 6.5 ML), which points to the fact that the effect of the lateral confinement is relatively weak, in spite of the shape of the electron wavefunction (larger in-plane spread for smaller QDs).

Figure 60(c) represents the hole square wavefunction in the nominal structure, whose shape does not present significant changes when varying the structural parameter. The probability of finding the hole is maximum at the bottom of the QDs. The electric field pushes the hole towards the wetting layer, but it remains laterally confined in the dot. This is because the valence band presents an in-plane maximum at the centre of the QDs, since it is the point with minimum strain. The in-plane (ε_{xx}) and out-of-plane (ε_{zz}) strain, displayed in Figure 60(c) for the nominal structure, are maximum in the wetting layer between two dots, whereas they decrease when penetrating the QD. The effect is more remarkable in the case of ε_{zz}. In an AlGaN/AlN quantum well, the compressive stress imposed by the smaller in-plane lattice parameter of AlN results in a compressive (negative) ε_{xx} in the quantum well. As a reaction to minimize the elastic energy in the layer, the out-of-plane lattice expands following $\varepsilon_{zz} = -(2\,c_{13}/c_{33})\varepsilon_{xx}$, where c_{13} and c_{33} are elastic constants. If we assume $c_{13} = 106$ GPa and $c_{33} = 398$ GPa for GaN [31], $c_{13} = 108$ GPa and $c_{33} = 373$ GPa for AlN [33], and a linear interpolation for the ternary alloy, we obtain $\varepsilon_{zz} = -\left(\frac{2c_{13}}{c_{33}}\right)\varepsilon_{xx} = -0.537\varepsilon_{xx}$ in $Al_{0.1}Ga_{0.9}N$. This describes approximately the behaviour of the wetting layer between the dots. However, in the dots, the

presence of AlN in contact with the facets introduces a vertical compressive stress, which results in ε_{zz} values close to zero in Figure 60(c).

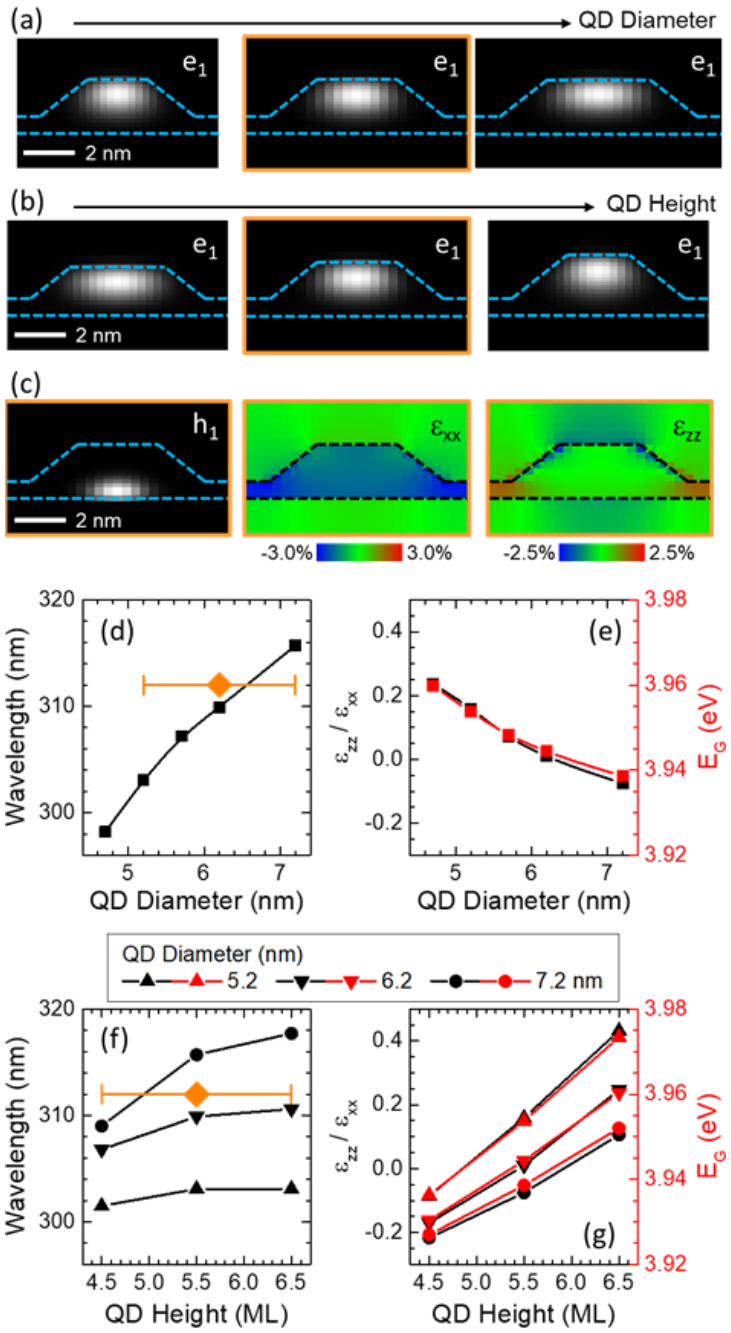

Figure 60. Calculations based on the structural parameters of E3962 (Nominally QDs with height = 5.5 ML, base diameter = 6.2 nm, wetting layer height = 2.5 ML, Al mole fraction in the QDs and in the wetting layer = 0.1). (a) Evolution of the electron square wavefunction (e_1) as a function of the QD diameter (5.2 nm, 6.2 nm, and 7.2 nm). The calculation with nominal parameters is framed in orange. (b) Evolution of the electron square wavefunction (e_1) as a function of the QD height (4.5 ML, 5.5 ML, and 6.5 ML). (c) For the nominal structure, hole square wavefunction (h_1), in-plane strain (ε_{xx}) and out of plane strain (ε_{zz},). (d) Variation of the emission wavelength as a function of the QD diameter. The experimental data with its structural error bar appears as an orange diamond. (e) Variation of the $\varepsilon_{zz}/\varepsilon_{xx}$ ratio and the band gap (E_G) at the maximum of the electron wavefunction, as a function of the QD diameter. (f) Variation of the emission wavelength as a function of the QD height for various values of QD diameter. The experimental data with its structural error bar appears as an orange diamond. (g) Variation of the $\varepsilon_{zz}/\varepsilon_{xxx}$ ratio and the band gap (E_G) at the maximum of the electron wavefunction, as a function of the QD height. The results are given for various values of QD diameter [65].

Let us concentrate now on the evolution of the expected emission wavelength calculated from the energy difference between the first electron and hole levels (e_1-h_1) and depicted in Figure 60(d) as a function of the QD diameter. In spite of the fact that the displacement of the electron wavefunction in Figure 60(a) is minimum, the emission energy presents a strong red shift when increasing the QD diameter. The spectral shift of 12.6 nm when changing the diameter by ±1 nm (variation that we had observed in the structural characterization of the sample) is comparable to the emission linewidth (FWHM = 19 nm at room temperature). To understand this shift, it is necessary to look at the evolution of the $\varepsilon_{zz}/\varepsilon_{xx}$ strain ratio, depicted in Figure 60(e). In QDs with small diameter, $\varepsilon_{zz}/\varepsilon_{xx}$ differs significantly from what is expected in a planar structure (-0.537), even reaching positive values. As the diameter increases, $\varepsilon_{zz}/\varepsilon_{xx}$ decreases, but it is still as high as -0.075 for a diameter of 7.2 nm. The variation of the strain state has direct impact on the band gap of the material via the band gap deformation potentials, as is illustrated in Figure 60(e). Therefore, the shift of the emission wavelength is mostly induced by the modification of the strain state.

If we look at the evolution of the emission wavelength as a function of the QD height, represented in Figure 60(f) for various values of QD diameter, an increase in height results in a slight red shift of the emission. However, the effect is moderate, only 2-4 nm when varying the height in the ±1 ML range that marks the structural dispersion, in spite of the clear vertical displacement of the electron wavefunction in Figure 60(b). This can also be understood looking at the evolution of $\varepsilon_{zz}/\varepsilon_{xx}$ as a function of the QD height and its effect on the band gap, both depicted in Figure 60(g). The increase of $\varepsilon_{zz}/\varepsilon_{xx}$ when increasing the QD height results in a larger band gap, which partially compensates the red shift tendency associated with the smaller vertical confinement and enhanced quantum confined Stark effect. Comparing the predicted shifts in Figure 60(d) and (f) and the experimental result with the error bars that describe the dot-to-dot structural fluctuations, it becomes clear that the QD diameter plays an important role in the determination of the emission wavelength and linewidth. We have also analysed the effect of varying the Al mole fraction in the dots and wetting layer by ±1% (see Figure 60), which corresponds to our error bar in the MBE flux calibration for this Al composition. We observe that the magnitude of the spectral shift induced by the deviation in composition would be ±1.8 nm, very small in comparison with the effect of the strain.

The detailed analysis presented here for E3962 is valid for other structures. For instance, looking at the results obtained for E3960, compiled in Table 12, fluctuations of the QD diameter by ±1 nm result in a spectral shift of 13.3 nm, larger than the effect of varying the QD height by ±1 ML, which leads to a spectral shift of 11.9 nm. In the extreme case of E3964 (Table 13), with QDs that are only 4 ML high, the effect of the diameter is relevant (spectral shift of 6.9 nm for a variation of the diameter by ±1 nm) but smaller than the effect of varying the height by ±1 ML (spectral shift of 16.1 nm), which appears as the major cause of spectral broadening.

5.2.3 Assessment of the Internal Quantum Efficiency

To quantify the IQE of the structures, temperature-dependent PL measurements were carried out with, first, a continuous wave laser at low power density (≈ 1.3 W/cm^2). The result is illustrated in Figure 61(a) and (b), where E3960 is used as an example. We take the liberty to calculate the IQE of the samples as the ratio of the integrated luminescence intensity at room temperature and at low temperature, i.e. $IQE \approx I(300\ \mathrm{K})/I(0\ \mathrm{K})$. This equation assumes that at 0 K nonradiative recombination is negligible. The resulting IQE can be overestimated if nonradiative recombination centres are active at low temperature or if nonradiative recombination centres are saturated by high power injection at room temperature. Figure 61(b) shows the integrated PL intensity as a function of the inverse temperature. The PL intensity remains approximately constant until 100 K and then drops

exponentially. The trend is well described by the Arrhenius equation:

$$I(T) \propto 1/\left(1 + Aexp(-E_a/kT)\right) \tag{5.1}$$

where *k* is Boltzmann constant, and *A* is a fitting parameter and E_a is the thermal activation energy of the dominant nonradiative process (E_a = 62±4 meV in the figure). This behaviour supports our assumption that nonradiative processes are negligible at low temperature, and the low power density of the laser (low injection) allows measuring the intrinsic IQE of the structures, without saturation of nonradiative centres. The values of the IQE measured this way are listed in Table 140, together with E_a for various samples. IQE values around 50% are systematically obtained for QDs grown with $\Phi_{\mathrm{Metal}}/\Phi_N$< 0.75. This is an improvement with respect to previous reports, where similar characterization (low injection) rendered IQE values in the range of 10-40% for GaN/AlN QDs grown with $\Phi_{\mathrm{Metal}}/\Phi_N$= 0.8-0.9 [63,156]. If we compare with the results obtained by Himwas et al. for $Al_{0.1}Ga_{0.9}N$/AlN QDs with $\Phi_{\mathrm{Metal}}/\Phi_N$= 0.63 [64], IQEs around 50% were only achieved for QD layers generated from 4-5 ML of $Al_{0.1}Ga_{0.9}N$. Our results here point to the fact that further reduction of the metal-to-nitrogen ratio increases the efficiency of small QDs, so that IQE around 50% is possible for QDs generated from only 3 ML of either GaN or $Al_{0.1}Ga_{0.9}N$.

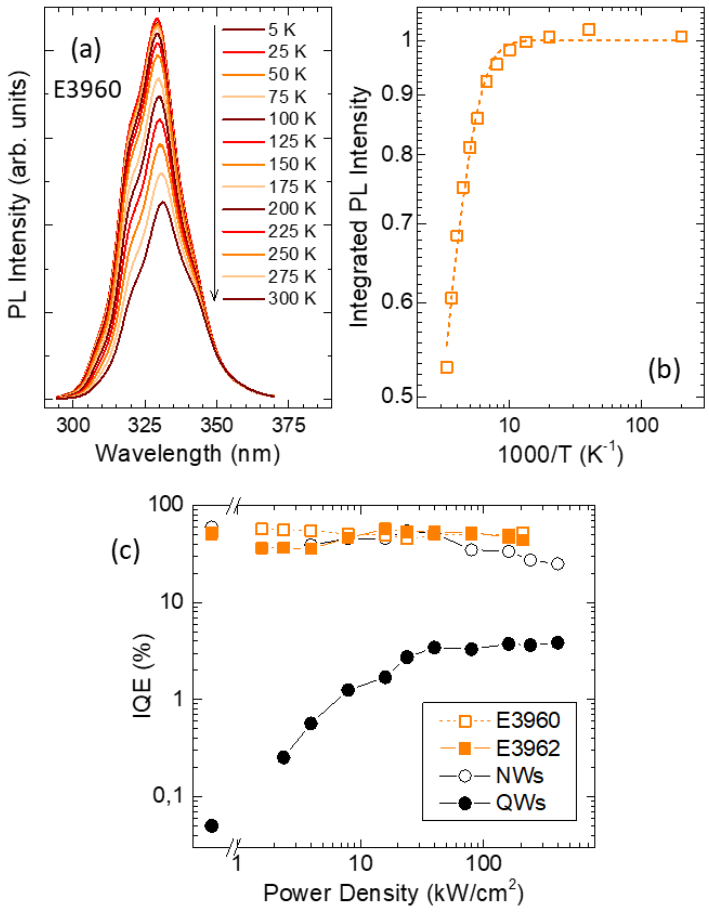

Figure 61. PL spectra from sample E3960 measured at various temperatures under low excitation density conditions (100 µW laser power, focused on a spot with a diameter of 100 µm). b) In the same sample, variation of the integrated PL intensity as a function of the inverse temperature. The dashed line is a fit to $I(T) \propto 1/\left(1 + Aexp(-E_a/kT)\right)$*, where k is Boltzmann constant, and A and* E_a *are fitting parameters. An activation energy* E_a *= 62±4 meV is extracted from the fit. c) Variation of the* IQE *for samples E3960, E3962 at room temperature as a function of the excitation power density measured with a pulsed Nd-YAG laser compared to NWs and QWs of similar structures [65].*

It is however true that most IQE values reported in literature are measured with a pulsed laser and at much higher power densities [42,111–120], in the range of 5-1000 kW/cm^2 to be close to the operation conditions of LEDs. This procedure leads to higher IQE values, which depend on the pulse width, repetition rate and power density of the pumping laser [111–114,117,121]. Nevertheless, our samples have been characterized with a pulsed laser (266 nm, 2 ns pulses, repetition rate of 8 kHz) and the IQE variation as a function of the excitation power density was recorded purely for the sake of comparison with literature. Measurements were performed at 6 K and at 300 K. For the calculation of the IQE at room temperature, taking into account the drop of the PL efficiency at low temperature due to the many-body effects induced by high-power excitation, we use equation 3.5 (chapter 3). The results are displayed in Figure 61(c). The GaN/AlN and $Al_{0.1}Ga_{0.9}N$/AlN SK QD samples (E3960 and E3962 in the figure, respectively) are compared with GaN/AlN QDs in nanowires and GaN/AlN multi-quantum-wells (from ref. [122]). The efficiency of both SK QDs and nanowires remain quite stable as a function of the pumping power. In the case of SK QDs, the IQE remains approximately constant for pumping power densities as high as 200 kW/cm^2. This proves our QDs are by far superior to other heterostructures in terms of stability under high excitation. However, it should be kept in mind that, in an electron-pumped UV lamp using an acceleration voltage of 5 kV and an injection current of 1 mA to irradiate a spot with a diameter of 1 mm, the excitation density would be below 1 kW/cm^2. This situation is clearly unfavorable for the use of quantum well structures.

5.2.4 Efficiency under electron beam pumping

Firstly, to attain high conversion efficiencies, the active region of these heterostructures should be able to collect a maximum number of electron-hole pairs generated by the impinging electrons via impact ionization. Therefore, we need to be sure to create the electron-hole pairs within the active region, to ensure minimum loss of energy. To estimate the penetration depth of the beam, we consider the Monte Carlo simulations using the CASINO software. Figure 41(a) (chapter 4) displays the energy loss of the impinging beam as it penetrates into the structure, assuming that it is pure AlN. From the figure, the energy loss associated to the electron-hole generation process takes place within the 530 nm of the active region for $V_A \leq 7.5$ kV and should hence lead to maximum energy conversion. Note that the fact of considering the structure consisting of pure AlN describes the worst-case scenario, since the density of GaN ($\rho = 6.10\ g/cm^{-3}$) is almost twice that of AlN ($\rho = 3.26\ g/cm^{-3}$), and the penetration depth of the electron beam is inversely proportional to the material density [44].

Experimental measurements of CL as a function of the accelerating voltage were also conducted to assess the penetration depth of the electron beam in operating conditions. We studied all the samples at acceleration voltages ranging from 2 kV to 30 kV. As an example, the spectra of E3964, normalized by their maximum and shifted vertically for clarity, are presented in Figure 62(a). For low acceleration voltages ($V_A \leq 15$ kV), we observe a single emission line, assigned to the QDs, at 270 nm. An additional emission at 330 nm appears for $V_A > 20$ kV. This is commonly assumed to be caused by carbon contamination in the AlN template [166–168]. The variation of the QD emission intensity normalized by the injection current (in the range of 500-614 nA) as a function of V_A is displayed in Figure 62(b). A saturation of the intensity is observed around $V_A = 9$ kV. Dividing the intensity by the injected power density, we obtain the variation of the emission efficiency as a function of V_A [Figure 62(c)]. The efficiency remains stable until $V_A = 9$ kV. Note that the total thickness of the active layers is around 530 nm. Comparing the experimental results with the Monte Carlo simulations in Figure 41(a), the electron penetration depth for $V_A = 9$ kV corresponds approximately to the total thickness of the active layers. Therefore, we can safely say that the efficiency remains approximately constant across the entire active region.

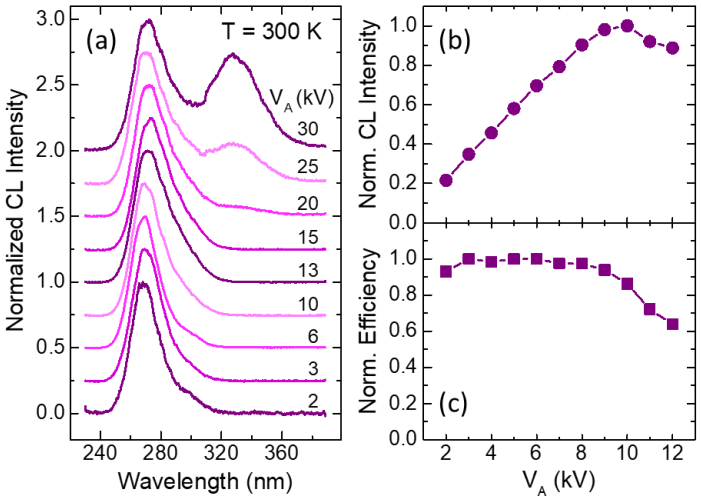

Figure 62. a) CL measurements of sample E3964 as a function of the acceleration voltage, V_A. Spectra are normalized at the maximum intensity value and vertically shifted for clarity. The emission from the quantum dot superlattice peaks at 270 nm. The band around 330 nm that appears for V_A > 20 kV is assigned to carbon contamination in the AlN template. c) Normalized CL intensity and (d) emission efficiency as a function of V_A for the same sample. Measurements were performed using an electron gun operated in direct current mode, under normal incidence, with a beam spot diameter of 4±1 mm [65].

To assess if our samples could work under high pumping currents without saturation, we measured the QD emission as a function of the injection current using an electron gun focused on a 4±1 mm spot. As an example, the results obtained for E3964 are presented in Figure 63(a). We first fixed V_A = 5 kV (which we assume is close to operation conditions, to prevent x-ray emission) and observed no saturation up to 800 µA (maximum injection current in our setup). In contrast, for V_A = 10 kV we observed a saturation of the emission intensity for injection current higher than 400 µA, presumably due to charging. This could be explained by the fact that, at 10 kV, part of the electron-hole pairs are generated in the AlN template, which makes it more difficult to evacuate the excess electrons. Interestingly, the saturation is associated to a spectral red shift of the emission, as illustrated in Figure 63(b). This shift can be partially due to thermal effects, and to the fact that smaller QDs, emitting at shorter wavelengths, are more prone to charging effects than larger QDs, emitting at longer wavelengths. This phenomenon in heterostructures with smaller QDs is attributed to the increased resistance as a result of the higher average Al content in the sample.

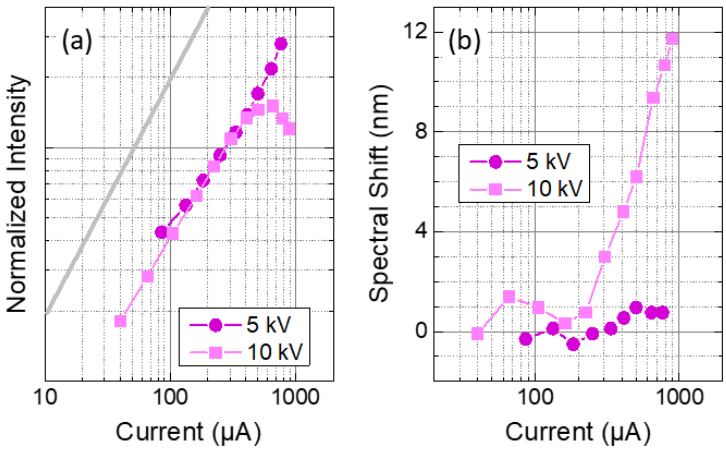

Figure 63. (a) Variation of CL intensity (sample E3964) as a function of the injection current measured for E3964 at V_A = 5 kV and 10 kV. The slope of the solid grey line corresponds to a linear increase. No saturation is observed up until 800 µA for V_A = 5 kV while a saturation for currents higher than 400 µA is observed at V_A = 10 kV. (b) Spectral shift observed as a function of the injection current [65].

Finally, as mentioned in chapter 4 in section 4.4.1., CL studies of GaN heterostructures in some groups have been reported to show a reversible degradation of the emission during the experiments attributed to charge accumulation and trapping at the surface. Therefore, we studied the stability of our samples under electron irradiation by measuring the evolution of the CL intensity with time. We studied two types of samples with identical heterostructures emitting at 330 nm, namely a bare GaN QD SL and a QD SL with a conductive $Al_{0.3}Ga_{0.7}N$ capping layer of 10 nm thickness over the SL. These measurements were performed first with an FE-SEM set-up and then with an electron gun. The FE-SEM experiment was performed at room temperature with an acceleration voltage V_A = 5 kV, the injected current was 25 pA and the beam was irradiating with spot size < 10 nm (i.e. excitation power density around 8 kW/cm^2 at the impact point). As seen in Figure 64, an effect of quenching over a period of 300 seconds for the bare GaN sample. This issue is easily fixed with a conductive capping layer, where the intensity remained stable in the scale of minutes with no sign of degradation. With the electron gun set-up, the measurements were performed for bare GaN SL at room temperature, acceleration voltage V_A = 5 kV, the injected current being 0.5 nA, with a spot size 4±1 mm. Here, electron gun pumping showed no charging issues without the need for a capping layer, as the spot size is larger, i.e. the pumping power density is much lower. This proves that our samples would potentially show no charging issues in the final device.

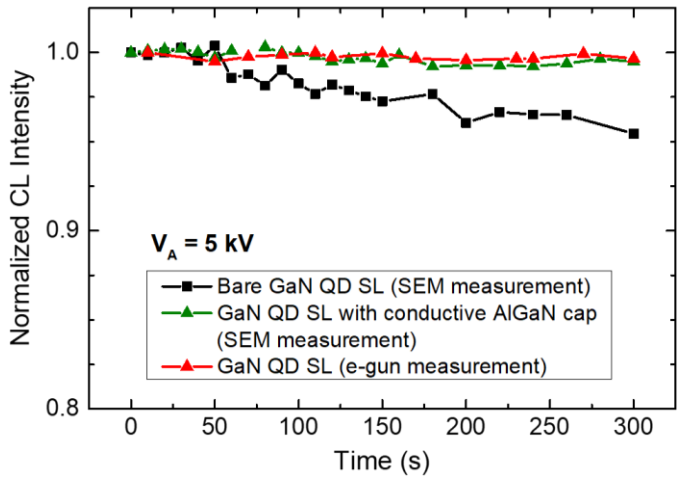

Figure 64. CL quenching measurements with time measured with two different set-ups. SEM measurements (spot size < 10 nm) show quenching in the scale of minutes, fixed with a conductive capping layer (green). In red, the electron gun pumping showed no charging issues as the spot size is larger (4±1 mm).

5.3 Towards shorter wavelengths: Increasing the Al content

5.3.2 Growth conditions

For this series, the growth was conducted by keeping the III-V ratio constant and varying the Al content in the dots. We do this as the incorporation of Al results in the lowering of the emission wavelength. As was the case for the previous series, we grew $Al_xGa_{1-x}N$/AlN SK QDs as the active region. These consisted of a stack of 100 layers of self-assembled $Al_xGa_{1-x}N$ QDs separated by 4 nm of AlN as barrier. For this series of $Al_xGa_{1-x}N$ QDs, we explored the effect of varying the Al content by tuning both Φ_{Al} and Φ_{Ga}, so that the targeted Al mole fraction in the dots is x = $\Phi_{Al}/(\Phi_{Al} + \Phi_{Ga})$ but the metal-to-nitrogen ratio remains constant ($(\Phi_{Al} + \Phi_{Ga})/\Phi_N = 0.5$) for all the samples. We considered QDs with x = 0.2, 0.4, 0.6 and 0.8. A summary of the samples under study is presented in Table 14.

Sample	x	Φ_{Ga} (ML/s)	Φ_{Al} (ML/s)	$\Phi_{\mathrm{Metal}}/\Phi_N$	Deposition time (QDs) (s)	Number of MLs	λ (nm)	FWHM (nm)	IQE (%)	WPE (%)
E4139	0	0.3	0	0.5	15	4.5	317	23.7		0.42
E4144	0.2	0.24	0.06	0.5	15	4.5	271	16.4	47	0.19
E4145	0.4	0.18	0.12	0.5	15	4.5	257	16.5		0.43
E4142	0.38	0.3	0.24	0.9	15	4.5	270	18.5		0.31
E4146	0.6	0.12	0.18	0.5	15	4.5	234	13.1	38	0.39
E4151	0.6	0.220	0.022	0.5	12	4.5	**228**+274	12.8	21	
E4150	0.8	0.06	0.24	0.5	15	4.5	**225**+254	18.1		0.50
E4152	0.8	0.149	0.015	0.5	12	4.5	**223**+263	13.1	33	
E4140	0.17	0.3	0.06	0.6	15	5.4	290	21		0.12
E4141	0.29	0.3	0.12	0.7	15	6.3	284	16		0.2

*Table 14. Growth parameters and optical characteristics of the samples under study: Al content as x, Ga and Al fluxes in monolayers per second ($\Phi_{Ga}$and Φ_{Al}, respectively), metal-to-nitrogen ratio (Φ_{Metal}/Φ_N), time of deposition of the dots, number of monolayers deposited for the generation of each QD layer, peak emission wavelength (λ) at room temperature (in the case of multiple peaks, the dominant peak appears in **bold** fonts), the FWHM, internal quantum efficiency (IQE) at room temperature measurement under low-injection conditions, and the wall plug efficiency (WPE).*

The QD superlattices were grown on 1-µm-thick (0001)-oriented AlN-on-sapphire templates (as mentioned in section 3.1.1.) at a temperature T_S = 720°C. The active nitrogen flux, Φ_N, was tuned to achieve a growth rate ν_{Ga} = Φ_{N} = 0.52 monolayers/s (ML/s) under metal rich conditions. The QD deposition time was 15 s for almost all the samples, changing it to 12 s for samples E3951 and E3952. The deposition of the QDs was followed by a growth interruption of 15 s. To favour the charge evacuation during the electron pumping process, the QDs were doped n-type with [Si] = 5×10^{18} cm^{-3} (value estimated from Hall effect measurements using the Van der Pauw method on planar Si-doped GaN layers). The AlN sections were grown under Al-rich conditions ($\Phi_{\mathrm{Al}}/\Phi_N$ = 1.1), followed by a growth interruption under nitrogen to consume the accumulated excess of Al, as we did for the previous series. At the end of the growth of each AlN barrier, the RHEED pattern showed the straight lines, which is characteristic of a planar surface.

The growth process was sharply interrupted (the precursor fluxes were shuttered, and the substrate was rapidly cooled down) after the deposition of the last QD layer, to enable optimal AFM characterization of the QD shape and density. The result of the AFM measurements is illustrated in Figure 65(c) for sample E4141. In such images, the QD density is ≈ $1.85\times10^{11}$$cm^{-2}$, and the height of the dots is about 0.4±0.17 nm, i.e. approximately 2-3 ML. Note that these values should correspond to the QD height above the wetting layer. Here, the QD density implies that the distance between QDs is approximately 18 nm. Since these dots emitting at shorter wavelength are significantly shorter than the previous series, we had to grow the sample E4141 to increase the metal content (and in turn the height) of the dots to be able to conduct AFM measurements to determine the density of dots.

To further assess the QD geometry, samples were studied using cross-section HAADF-STEM. The results for the same are presented in Figure 65. The QDs are fairly resolved. The QD base diameter is in the range of 5-7 nm, and the QD height (including wetting layer) is 4±1 ML, for sample E4140. In addition, the wetting layer thickness is estimated at 2-3 ML. The average values and error bars were extracted by analysing images of at least 10 QDs per sample. Note that the measurement of the base diameter, clearly smaller than the distance between dots estimated from AFM, implies that we are in a situation as described in Figure 57(a) for the AFM measurements, i.e. the value of QD height above

the wetting layer extracted from AFM is reliable, which is confirmed by the fact that similar results of the QD height are extracted from AFM and STEM measurements. Comparing these dots to those grown with less Al (previous series varying the III/V ratio), it is clear that they have the tendency to be more planar. This is due to the reduced strain difference between the AlGaN dots and the AlN barrier. So with 20% or more of Al in this case, a noticeable distortion of the QD morphology is observed, unlike with only 10% in the previous series.

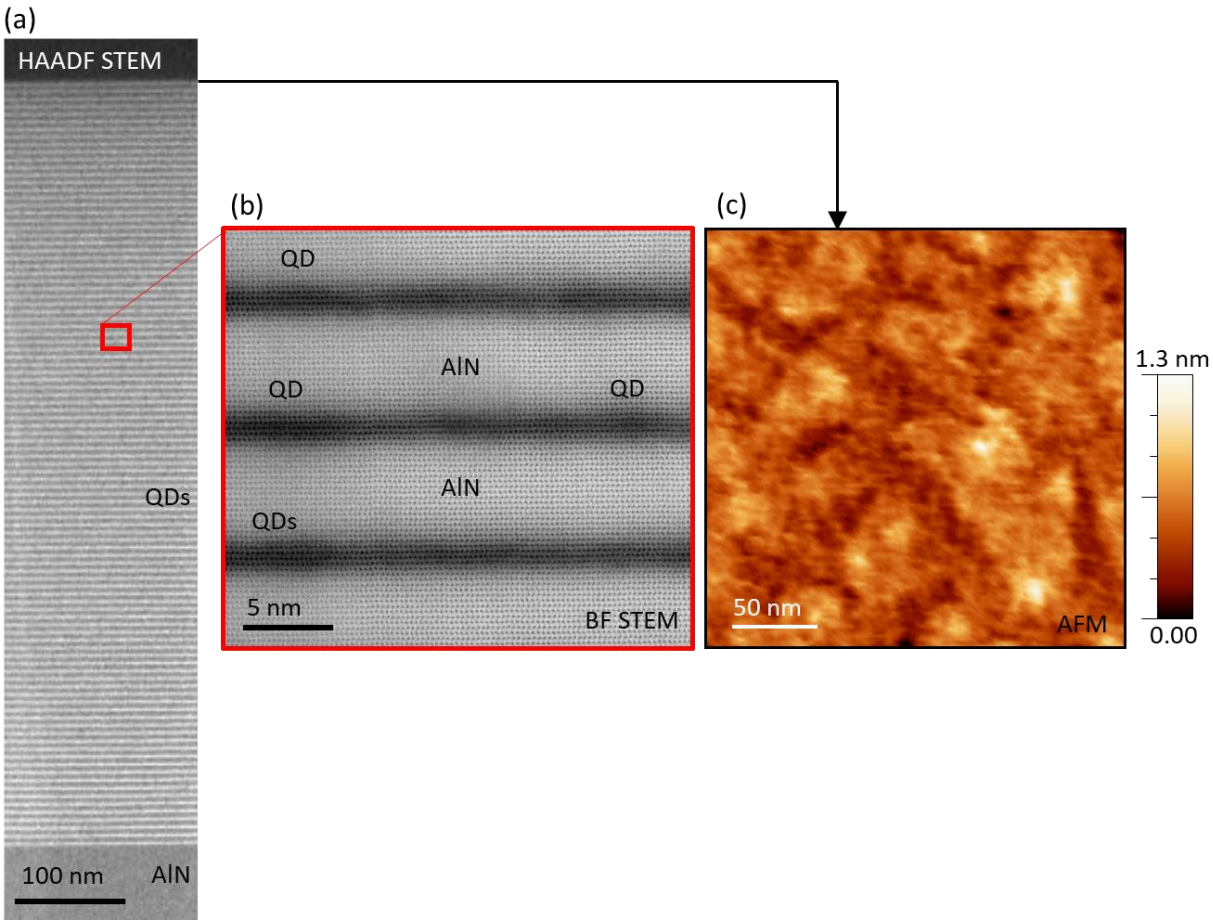

Figure 65. The HAADF-STEM, BF-STEM images of the QDs in study and AFM for observing the morphology of the top layer.

5.3.3 Optical characterization

The CL emission of the dots at room temperature was recorded and compared as shown in Figure 66. The measurements presented here were recorded in an FE-SEM set-up with the accelerating voltage fixed at 5 kV. In the graph, we considered only samples grown with a III/V ratio of 0.5 and a QD deposition time of 15 s. The spectra are vertically shifted, increasing the Al mole fraction, from x = 0 (bottom) to 0.8 (top). The peak emission wavelength (λ) of the samples under study and the emission full width at half maximum (FWHM) are summarized in Table 14. The spectra blue shifts from 317 to 225 nm when increasing the Al content in the QDs from 0 to 80%. The relative FWHM remains in the range of 5.6-8% in all the samples, without clear trend as a function of the Al content. In the samples with higher Al content, we observe a shoulder at longer wavelengths, in the range of 255-275 nm. This luminescence might be due to a bimodal distribution of QDs or to emission associated with point defects and pollutants, which might be magnified by reabsorption of the luminescence from the QDs. At this point, it was not possible to identify the origin of this luminescence, which might be discriminated by measurements of time-resolved CL. However, first experiments were not conclusive.

With increasing the Al content from 0.6 to 0.8, the spectral blue shift was small but the long wavelength parasitic emission was more intense in the sample with x = 0.8. This observation brought us to consider a reduction of the deposition time from 15 s to 12 s, as a way to blue shift the emission without increasing the Al content in the QDs. We performed the experiment for samples with x = 0.6 (E4151) and x= 0.8 (E4152). In both cases, the emission slightly blue shifted with respect to samples with 15 s of deposition time. However, the secondary long-wavelength peak was systematically more intense and better defined in the samples with shorter deposition time, as seen in Figure 66(b).

In table 14, we decided to also include sample E4142. This sample, with almost 40% of Al in the QDs, differs from E4145 in the fact that it was grown with a much higher III/V ratio (0.9 for E4142 vs. 0.5 for E4145). The result is that the emission of E4142 is significantly red shifted (as expected from the higher amount of material in the QDs, and in agreement with our previous study).

To quantify the IQE of the structures, temperature-dependent CL measurements were carried out with an FE-SEM set-up. We calculated the IQE of the samples as the ratio of the integrated luminescence intensity at room temperature and at low temperature, i.e. $IQE \approx I(300\ \mathrm{K})/I(0\ \mathrm{K})$. The measurement proved difficult due to charging effects. To be sure of the reliability of the measurements, we probed at least 5 different regions of the sample at each temperature, and we performed the room temperature measurements before cooling down and after cooling down. The measurements collected in Table 14 gave reliable results, with slight deviations of intensity from point to point (smaller than 10%) and recovering the original luminescence when warming up. We observe that $IQEs$ higher than 30% can be obtained for samples emitting at wavelengths shorter than 230 nm.

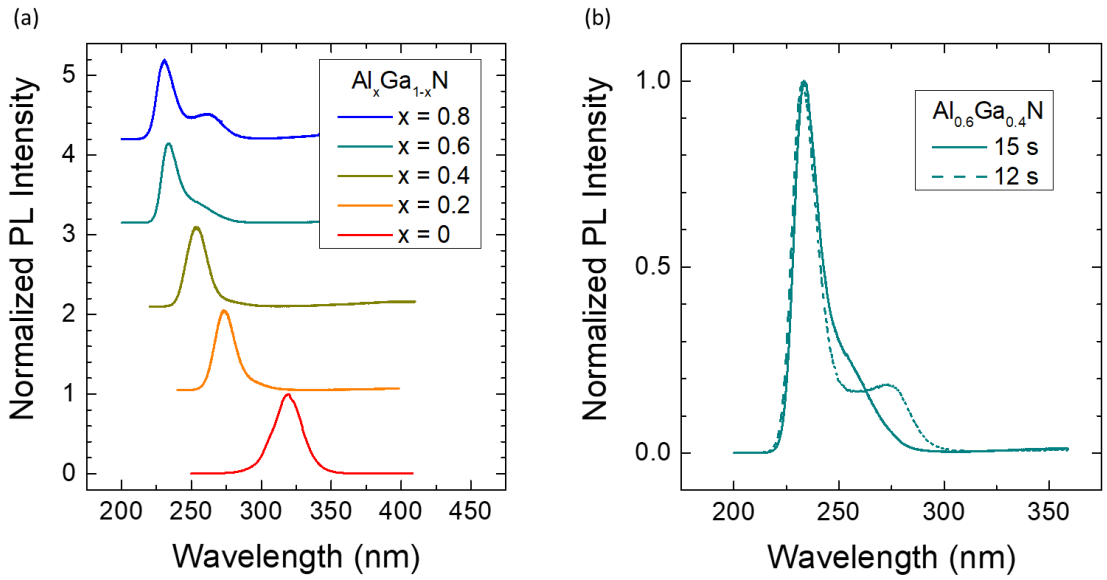

Figure 66. (a) Room-temperature CL emission from AlGaN/AlN quantum dot superlattices grown with varying Al content (from bottom to top, x = 0, 0.2, 0.4, 0.6, 0.8 and $(\Phi_{Al}+\Phi_{Ga})/\Phi_N$= 0.52). The spectra are normalized to their maxima and vertically shifted for clarity. (b) Variation of spectra by keeping Al content constant at 60% and changing the deposition time (continuous line: 15 s and dotted line: 12 s). Multiple peaks are observed by reducing the deposition time of the dots.

5.3.4 Power efficiency measurements

We measured the WPE of our samples by first calculating the angular distribution of the UV emission. To measure the angular distribution, a calibrated UV photodetector (GaP) was been attached to a rotator in the chamber to measure CL (the system has been installed by Dr. S. Purcell),

as mentioned in section 3.3.6 and Figure 40. As an example, the distribution obtained for sample E4013 (copy of sample E3964 from Table 10) is displayed in Figure 67.

These WPE measurements were performed on $Al_xGa_{x-1}N$ QDs with x= 0, 0.2, 0.4, 0.6 and 0.8. We used equation 3.5 and 3.6, to calculate the WPE of the samples and the results are listed in Table 15. From our calculations, an average WPE of 0.36% is observed for all the samples, without any clear tendency as a function of the emission wavelength.

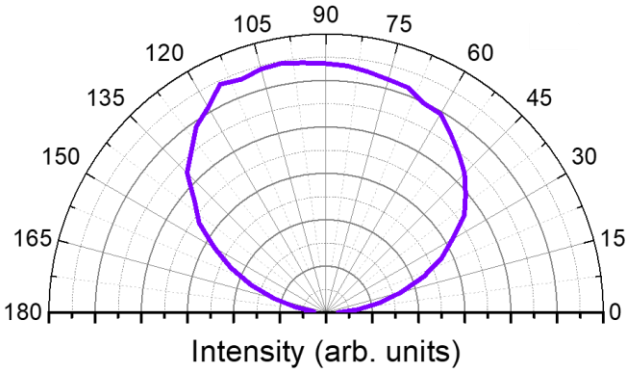

Figure 67. Measurement of the angular distribution of the luminescence angle of sample E4013 under electron beam excitation.

Sample name	Peak emission (nm)	WPE
E4013	290	0.31%
E4139	317	0.42%
E4144	271	0.19%
E4145	257	0.43%
E4142	270	0.31%
E4146	234	0.39%
E4150	225+254	0.5%

Table 15.The wall plug efficiency (WPE) of samples measured with angular emission with electron pumping.

These numbers are compared to those reported in the literature in Figure 68, where our results appear as green symbols. We observe a significant improvement of the WPE numbers for our samples at shorter wavelengths, which makes this approach promising for disinfection around the 220 nm spectral region. Note that so far, there was no effort to improve the light extraction efficiency of the samples and thermal management was not addressed. Therefore, there is still significant room for improvement.

5.4 Conclusions

To summarize, we have demonstrated 100-period $Al_xGa_{1-x}N$/AlN QDs emitting at wavelengths between 335 and 225 nm at room temperature, with a relative linewidth in the 5.5-11% range. The $Al_xGa_{1-x}N$/AlN active region is about 530 nm long, which is enough to collect the electron-hole pairs generated by an electron beam with an acceleration voltage $V_A \leq 9$ kV. This was experimentally confirmed with extensive CL studies. We did not observe any significant variation of the efficiency or emission line width for acceleration voltages in the range of $2 \leq V_A \leq 9$ kV, which indicates that the nanostructures are homogeneous along the growth axis, and the linewidth is mostly limited by the in-plane fluctuations of the QD diameter.

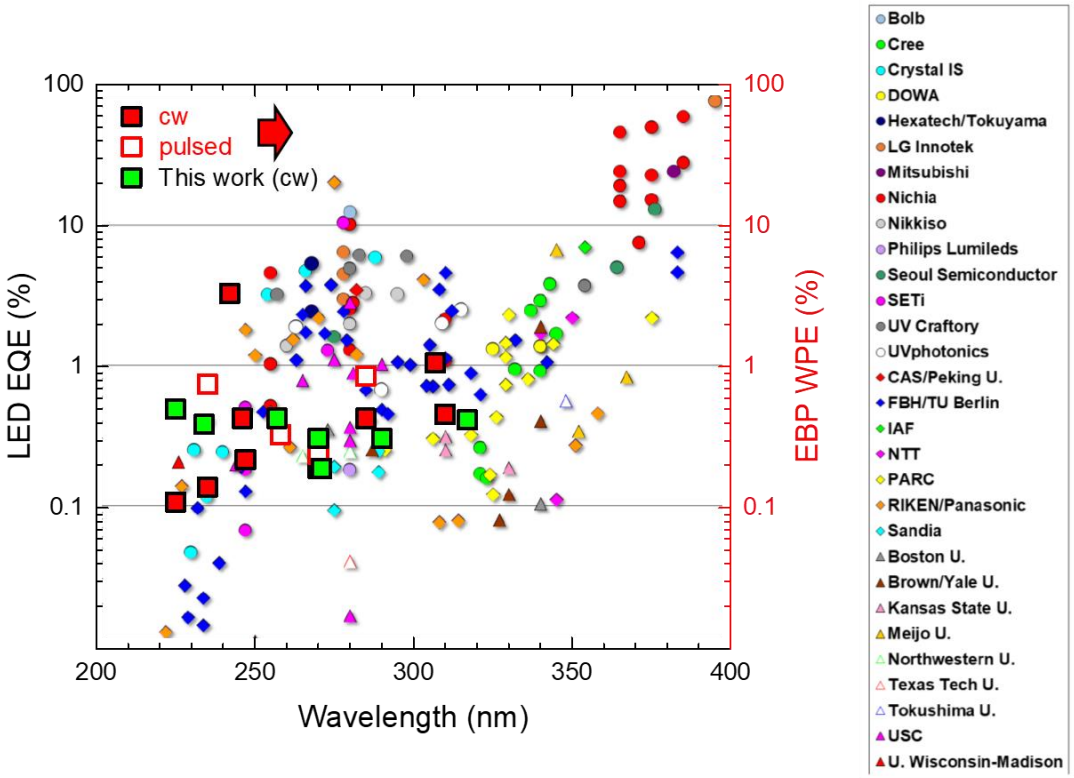

Figure 68. EQE reported in literature (smaller points with various colours) plotted with WPE of electron pumped UV lamps in literature (larger red squares) and our results (larger green squares).

We have first studied a series of $Al_xGa_{1-x}N$/AlN ($0 \leq x \leq 0.1$) QD superlattices where we have varied the III/V ratio during the deposition of the QDs. In this case, the superlattices displayed peak emission between 335 and 244 nm. The evolution the emission peak in accordance to the QD shape was investigated from the fitting of theoretical calculations performed by Nextnano[3] solver to the experimental results. We concluded that the evolution of the emission wavelength as a function of the QD height (an increase in height results in a slight red shift of the emission) is less significant than the variation of QD diameter, which plays a more important role in the determination of the emission wavelength and linewidth. The increase of $\varepsilon_{zz}/\varepsilon_{xx}$ when increasing the QD height results in a larger band gap, which partially compensates the red shift tendency associated with the smaller vertical confinement with the larger QD height and enhanced quantum confined Stark effect. We observe that the magnitude of the spectral shift induced by the deviation in composition is about ±1.8 nm, very small in comparison with the effect of the strain.

In this series, the IQE of all the samples were quantified, obtaining values around 50% for QDs synthesized with III/V ratio < 0.75. Efficiencies remained stable as a function of the pumping power up to high as 200 kW/cm^2, proving that SK QDs can be used for application in devices with various pumping requirements. Under electron beam pumping at 5 kV, the UV emission of the heterostructures scales linearly with the injected current in the measured range up to 800 µA (with continuous pumping using an electron gun). For V_A = 10 kV, a saturation is observed for injection currents higher than 400 µA which is attributed to enhanced charging effects due to the injection of carriers in the AlN substrate.

In a second series of samples, we maintained a III/V ratio of 0.5 and increased the Al content in the QDs from x = 0 to x = 0.8, trying to reach even shorter wavelengths. The spectra blue shifts from

317 to 225 nm when increasing the Al content in the QDs from 0 to 80%. The relative FWHM remains in the range of 5.6-8% in all the samples. Cathodoluminescence measurements show that IQEs around 30% can be achieved in QD samples emitting at wavelengths shorter than 230 nm.

The power efficiency of from selected samples was extracted from the integration of measurements of the emitted optical power as a function of the angle. An average of efficiency 0.38% is obtained for samples emitting in the 317-225 nm range, without clear tendency as a function of wavelength. We observe a significant improvement of the WPE numbers for our samples at shorter wavelengths, which makes this approach promising for disinfection in the deep UV spectral region. This study promises great potential for further studies on these particular QDs.

6 Conclusions and perspectives

6.1 Conclusions

This thesis was aimed towards investigating an active media for electron-pumped ultraviolet (UV) lamps for disinfection. We proposed two types of heterostructures for this purpose, namely AlGaN/AlN quantum dots (QDs) embedded in GaN nanowires (NWs) synthesized on Si(111) substrates and AlGaN/AlN QDs grown by the Stranski-Krastanov (SK) method on AlN. I studied the performance of both kinds of nanostructures and came up with the following conclusions.

We first presented the feasibility of AlGaN/AlN NWs for electron-pumped UV emitters. These NWs consisted of a 900-nm-long GaN stem capped with a 400-nm-long $Al_xGa_{1-x}N$/AlN multi-quantum dot superlattice (SL). Structural and optical studies demonstrated that the QD dimensions were quite homogeneous along the length of the SL giving a single emission line in the deep UV range, which was tuned in the range from 340 to 258 nm by varying the dot/barrier thickness ratio and the Al content in the dots. Compared to planar samples of similar periodicity and thickness, the NW structures are less sensitive to non-radiative recombination under PL excitation, attaining IQE levels higher than 60% at 340 nm at room temperature, decreasing when reducing the emission wavelength. At 270 nm, the IQE was around 30%. These efficiencies were measured under low injection conditions. Under pulsed optical excitation, attaining high injection, the IQE remains stable for excitation power densities up to 200 kW/cm^2.

Studies under electron pumping show that electron channeling effects can be compensated by an increase of the active region length by ≈ 60% in comparison to planar layers. As a result, our NW SL are thick enough to collect the electron-hole pairs generated by an electron beam operated with an acceleration voltage V_A = 5 kV. The external quantum efficiency under optical pumping was measured for some samples, with promising results (3.42±0.55%).

Regarding AlGaN/AlN QD SLs, we propose a design for the AlGaN/AlN QD SLs active region with a thickness of 530 nm obtained by measuring the electron penetration depth, given by the acceleration voltage of the beam. The active region structure consisted of 100 periods of QDs and AlN barrier thickness of 4 nm (to achieve surface planarization after the deposition of each QD layer). We demonstrated that by modifying the III/V ratio and/or the composition of the QDs, the peak emission wavelength can be tuned from 225 nm to 335 nm while keeping the internal quantum efficiency (IQE) higher than 35% up to 60%. With an Al composition ≤ 10% and a III/V ratio < 0.75, we managed to consistently get an IQE of about 50%. Under pulsed optical excitation, the IQE remains stable for excitation power densities up to 200 kW/cm^2.

The evolution the emission peak in accordance to the QD shape is investigated from the fitting of theoretical calculations performed by Nextnano^3 solver to the experimental results. We concluded that the evolution of the emission wavelength as a function of the QD height is less significant than the variation of QD diameter. The variation in QD height and strain plays a more important role in the determination of the emission wavelength and linewidth.

Under electron beam pumping at 5 kV, the UV emission of the heterostructures scales linearly with the injected current in the measured range up to 800 µA (with continuous pumping using an electron gun) without any indication of saturation. For V_A = 10 kV, a saturation is observed for injection

currents higher than 400 μA which is attributed to enhanced charging effects due to the injection of carriers in the AlN substrate.

QDs emitting in the shorter wavelength with higher amount of Al in the dots show promising results, with IQE values over 30% at wavelengths shorter than 230 nm. An average WPE of 0.38% is measured for these structures, even for samples with short-wavelength peak emission (225 nm). These results are very interesting for the application of these QD SLs in electron beam pumped UV emitters for disinfection not only at 270 nm but also close to the 220 nm germicidal peak.

6.2 Perspectives

6.2.1 Nanowire technology

This work provides the assessment of QDs in NWs at an initial stage for application in electron-pumped UV sources. Our results confirm the feasibility of this approach with potential for further improvement. This could be achieved by removing the silicon substrate and transferring the ensemble to a UV reflecting material. In addition, growth efforts should be made to reduce the length of the GaN stem, or replace it with AlGaN. In the path towards an operating prototype, the cathodoluminescence efficiency should be quantified and the lifetime under electron excitation should be evaluated (we have already confirmed stability in the scale of 5 min, but long term studies should still be performed).

The NW studies reported here are very promising for other applications beyond UV emission. NWs can be integrated in flexible electronics, silicon photonics or implantable devices. Our demonstration of high uniformity in long (many periods) AlGaN/AlN superlattices in a NW opens prospects for new miniature ultrasensitive photodetectors (including intersubband photodetectors) or sensors, or as new building blocks in NW LEDs.

6.2.2 Stranski-Krastanov QD technology

Using these nanostructures, electron-pumped devices can be scaled down to millimeter size, so that it can compete with LEDs in domains where efficiency and total output power are relevant. For the utilisation of such technology, the cost per milliwatt of optical power comes into play, which could become competitive with LEDs due to the simpler material growth and processing. By keeping the acceleration voltage at 5 kV, the generation of x-ray should be low enough to implement this domestically. For industrial applications where x-ray irradiation is not a problem anymore, V_A could, in principle, be increased and, in that case, the feasibility of longer active regions could be further inspected.

All my work was performed on AlN-on-sapphire templates, with the advantage of being transparent in the UV range. It will be important to assess the thermal performance of these samples by performing cathodoluminescence studies under pumped excitation. If thermal issues are relevant, several approaches could be considered:

- Improvement of the sapphire-to-holder contact with a material that improves thermal dissipation.
- Use of SiC substrates, which would lead to better thermal management at the price of reducing the light extraction efficiency (SiC is not transparent in the UV range for disinfection).

- Change of the lamp geometry. All our tests consider a reflection configuration for the lamp [11]. A transmission mode geometry could also be considered. There, the active region would be metalized and electrons would be injected through the metal. Thermal dissipation would be different in such a configuration.

Light extraction is one of the major concerns of fabricating UV lamps, which was not addressed in this thesis. Some of the methods to improve light extraction from the active region are listed below:

1. Sidewall polishing of samples to prevent losses from the sides.
2. Back wall polishing to make the backside perfectly reflecting to prevent losses from the backside.
3. Surface patterning to improve the extraction.

For future studies, these post-growth treatments for further improvements in efficiencies should be seriously considered.

As a preliminary study to estimate theoretically the effect of light extraction treatments on our samples, Fabien Rol from CEA-LETI performed some LightTools simulations [169]. The target was to estimate the percentage of the generated light that is transmitted to air. The simulations were performed assuming that the QD superlattice behaves as an AlGaN material emitting at 260 nm, assuming light is generated uniformly in this AlGaN layer. The layer is deposited on top of 1 µm of AlN and a 350 µm thick sapphire substrate. We assumed that the backside of the substrate was metallized with Al. To study the effect of roughening of the AlGaN surface, the roughening was assumed to be AlGaN pyramids in the shape of 1 µm radius cones with 60° cone angle, as shown in Figure 70. Following were the main takeaways from these simulations, assuming zero absorption:

- From 0 to 100% backside diffuse reflectivity, the LEE improved from 3% to 22%
- With front-side roughening, and varying also from 0 to 100% backside diffuse reflectivity, the LEE improved from 13% to 69%

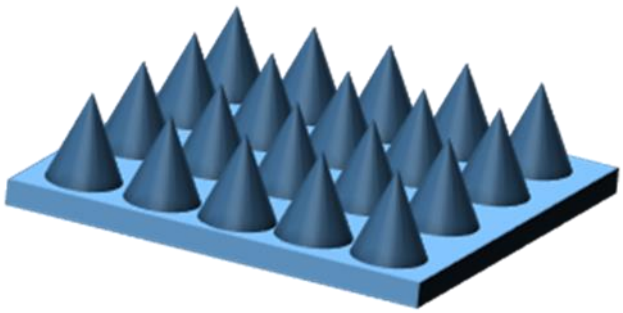

Figure 69. Illustration of cones used to depict surface roughening: These were 1 µm radius cones with 60° cone angle.

From the simulations we could deduce that backside polishing of samples gives a significant improvement of LEE, but not as much as frontside patterning. Therefore, frontside roughening (combined with backside polishing) should be the main focus of post-growth treatments.

Experimentally, we started with sidewall and backside polishing. This treatment was performed on sample E4013, which is identical to sample E3963 emitting at 290 nm. The sample was divided in two parts, one remained the reference, the second was only sidewall polished, and the third was sidewall and backside polished as well as metallized with a thin 100 nm layer of Al on the backside. Preliminary studies, of the WPE measurements mentioned in section 3.3.3., were performed. CL

measurements showed no major variations in the efficiency measurement (0.31%, 0.4% and 0.32% for the first, second and third samples, respectively). Further and more systematic studies are required to confirm this point.

Regarding the nanopatterning of the active surface, one can employ various lithography techniques like photolithography, electron beam lithography, nanoimprint lithography etc. We have decided to opt for a cost effective approach, which is the nanosphere lithography (NSL), also known as colloidal lithography [170]. It requires the deposition and self-assembly of polystyrene or silica nanospheres of desired size (here we used 600 nm spheres) and then etching the surface to achieve roughening.

During the course of my PhD, I developed a methodology for NSL optimized for our samples. First, the samples were treated with piranha solution to remove any organic residues and turn the surface hydrophilic (AlN is hydrophobic in nature). For the deposition of the silica nanospheres, I calculated the required amount of nanospheres to obtain a monolayer coverage of the sample, and I prepared a dilution so that the good amount of spheres is contained in droplet of 10 µl, which is enough to cover the sample surface. The solution with spheres was first sonicated. Then droplet is carefully measured with a micropipette, dropped on the sample, and dried at an angle of 10° [171].

According to our sample size and observations, the dilution and droplet size was modified to prevent in clustering of spheres or multilayers. Therefore, we conducted a series of experiments to achieve the right dilution and droplet amount for the nanosphere deposition. The optimum amount for 8×8 mm samples is a 2.5 µl droplet with a dilution of 0.5% in ethanol. This provided a homogeneous dispersion of self-assembled spheres.

After the dispersion, a two-step reactive ion etching (RIE) etching method for the roughening was performed. The first step was to reduce the size of the spheres by fluoride etching (using CF_4 CH_2F_2) to create space between the spheres. After the reduction of the size of the sphere, the top was metallized with a thin layer ≈ 100 nm, of Ni. Then the spheres were removed by sonication. The metallized negative area is left on the (previously occupied by the reduced spheres). Then chloride etching was performed on AlN with by Cl_2/BCl_3 for about 3 minutes to obtain roughness. We aimed for 100-200 nm depth on the surface to be able to direct light more efficiently. The SEM images of these steps are shown in Figure 70.

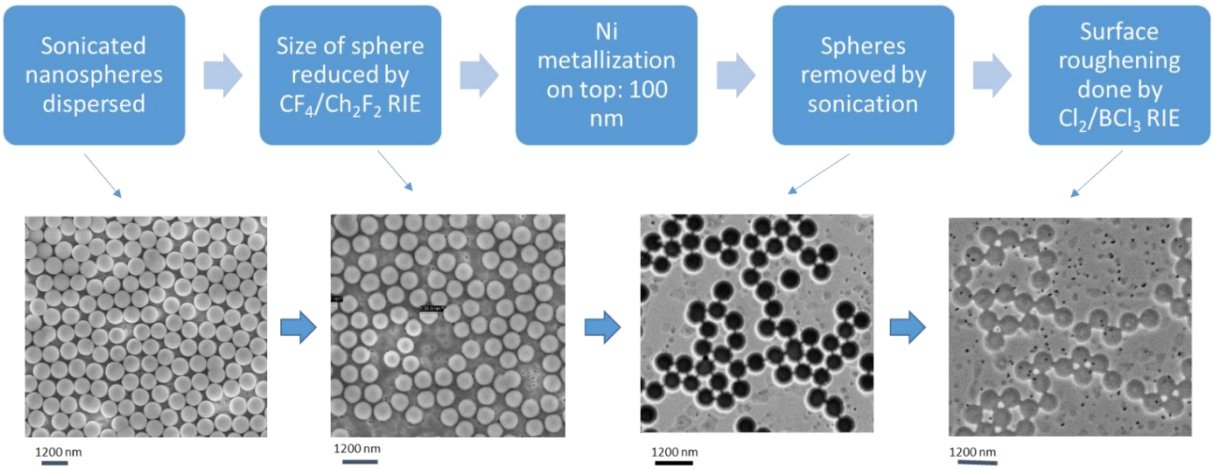

Figure 70. The nanosphere lithography steps for performing surface roughness. First, the nanospheres are dispersed on the surface, then the size of the spheres is reduced by fluoride etching, then the surface is metallized with Ni and then the spheres are removed. Finally, the surface is etched again and the metal is removed to obtain the surface roughness.

Unfortunately, preliminary EQE studies could not provide definite details on the improvement but must be looked into for future studies. With the support of theoretical calculations, the size of the spheres should be varied and the etching depth should be optimized. These studies could be one of the first to provide enhanced efficiencies for electron beam pumped UV emitters.

7 Bibliography

[1] Downes A and Blunt T P 1877 The Influence of Light upon the Development of Bacteria 1 *Nature* **16** 218–218

[2] Downing A M W, Blunt Thos P and Marshall J 1878 III. Researches on the effect of light upon Bacteria and other organisms *Proceedings of the Royal Society of London* **26** 488–500

[3] Wells W F and Fair G M 1935 VIABILITY OF B. COLI EXPOSED TO ULTRA-VIOLET RADIATION IN AIR *Science* **82** 280–1

[4] Mamahlodi M T 2019 Potential benefits and harms of the use of UV radiation in transmission of tuberculosis in South African health facilities *J Public Health Afr* **10** 742

[5] Bintsis T, Litopoulou-Tzanetaki E and Robinson R K 2000 Existing and potential applications of ultraviolet light in the food industry - a critical review *J Sci Food Agric* **80** 637–45

[6] Buonanno M, Welch D, Shuryak I and Brenner D J 2020 Far-UVC light (222 nm) efficiently and safely inactivates airborne human coronaviruses *Scientific Reports* **10** 10285

[7] Buonanno M, Ponnaiya B, Welch D, Stanislauskas M, Randers-Pehrson G, Smilenov L, Lowy F D, Owens D M and Brenner D J 2017 Germicidal Efficacy and Mammalian Skin Safety of 222-nm UV Light *Radiat Res* **187** 483–91

[8] Webpage: Minamata Convention on Mercury: https://www.mercuryconvention.org/en

[9] Muramoto Y, Kimura M and Nouda S 2014 Development and future of ultraviolet light-emitting diodes: UV-LED will replace the UV lamp *Semicond. Sci. Technol.* **29** 084004

[10] Glaab J, Haefke J, Ruschel J, Brendel M, Rass J, Kolbe T, Knauer A, Weyers M, Einfeldt S, Guttmann M, Kuhn C, Enslin J, Wernicke T and Kneissl M 2018 Degradation effects of the active region in UV-C light-emitting diodes *Journal of Applied Physics* **123** 104502

[11] Cuesta S, Harikumar A and Monroy E 2022 Electron beam pumped light emitting devices *J. Phys. D: Appl. Phys.*

[12] Davydov V Y, Emtsev V V, Goncharuk I N, Smirnov A N, Petrikov V D, Mamutin V V, Vekshin V A, Ivanov S V, Smirnov M B and Inushima T 1999 Experimental and theoretical studies of phonons in hexagonal InN *Applied Physics Letters* **75** 3297

[13] Vurgaftman I, Meyer J R and Ram-Mohan L R 2001 Band parameters for III–V compound semiconductors and their alloys *Journal of Applied Physics* **89** 5815

[14] Kanoun M B, Goumri-Said S, Merad A E and Mariette H 2005 Ab initio study of structural parameters and gap bowing in zinc-blende AlxGa1−xN and AlxIn1−xN alloys *Journal of Applied Physics* **98** 063710

[15] Vurgaftman I and Meyer J R 2003 Band parameters for nitrogen-containing semiconductors *Journal of Applied Physics* **94** 3675

[16] Morkoç H, Strite S, Gao G B, Lin M E, Sverdlov B and Burns M 1994 Large-band-gap SiC, III-V nitride, and II-VI ZnSe-based semiconductor device technologies *Journal of Applied Physics* **76** 1363–98

[17] Sumiya M and Fuke S 2004 Review of polarity determination and control of GaN *MRS Internet Journal of Nitride Semiconductor Research* **9** 1–34

[18] Kobayashi A, Sankey O F, Volz S M and Dow J D 1983 Semiempirical tight-binding band structures of wurtzite semiconductors: AlN, CdS, CdSe, ZnS, and ZnO *Phys. Rev. B* **28** 935–45

[19] Dingle R, Sell D D, Stokowski S E and Ilegems M 1971 Absorption, Reflectance, and Luminescence of GaN Epitaxial Layers *Phys. Rev. B* **4** 1211–8

[20] Chen G D, Smith M, Lin J Y, Jiang H X, Wei S, Asif Khan M and Sun C J 1996 Fundamental optical transitions in GaN *Applied Physics Letters* **68** 2784–6

[21] Li J, Nam K B, Nakarmi M L, Lin J Y, Jiang H X, Carrier P and Wei S-H 2003 Band structure and fundamental optical transitions in wurtzite AlN *Applied Physics Letters* **83** 5163

[22] Merz C, Kunzer M, Kaufmann U, Akasaki I and Amano H 1996 Free and bound excitons in thin wurtzite GaN layers on sapphire *Semicond. Sci. Technol.* **11** 712–6

[23] Xu Y-N and Ching W Y 1993 Electronic, optical, and structural properties of some wurtzite crystals *Physical Review B* **48** 4335–51

[24] Santic B 2003 On the hole effective mass and the free hole statistics in wurtzite GaN *Semicond. Sci. Technol.* **18** 219–24

[25] Im J S, Moritz A, Steuber F, Härle V, Scholz F and Hangleiter A 1998 Radiative carrier lifetime, momentum matrix element, and hole effective mass in GaN *Applied Physics Letters* **70** 631

[26] Salvador A, Liu G, Kim W, Aktas Ö, Botchkarev A and Morkoç H 1995 Properties of a Si doped GaN/AlGaN single quantum well *Appl. Phys. Lett.* **67** 3322–4

[27] Ramos L E, Teles L K, Scolfaro L M R, Castineira J L P, Rosa A L and Leite J R 2001 Structural, electronic, and effective-mass properties of silicon and zinc-blende group-III nitride semiconductor compounds *Phys. Rev. B* **63** 165210

[28] Ng T K, Holguin-Lerma J A, Kang C H, Ashry I, Zhang H, Bucci G and Ooi B S 2021 Group-III-nitride and halide-perovskite semiconductor gain media for amplified spontaneous emission and lasing applications *J. Phys. D: Appl. Phys.* **54** 143001

[29] Dridi Z, Bouhafs B and Ruterana P 2003 First-principles investigation of lattice constants and bowing parameters in wurtzite AlxGa1 xN, InxGa1 xN and InxAl1 xN alloys *Semicond. Sci. Technol.* **18** 850–6

[30] Takagi Y, Ahart M, Azuhata T, Sota T, Suzuki K and Nakamura S 1996 Brillouin scattering study in the GaN epitaxial layer *Physica B: Condensed Matter* **219–220** 547–9

[31] Polian A, Grimsditch M and Grzegory I 1996 Elastic constants of gallium nitride *Journal of Applied Physics* **79** 3343–4

[32] Kim K, Lambrecht W R L and Segall B 1996 Elastic constants and related properties of tetrahedrally bonded BN, AlN, GaN, and InN *Phys. Rev. B* **53** 16310–26

[33] Wright A F 1997 Elastic properties of zinc-blende and wurtzite AlN, GaN, and InN *Journal of Applied Physics* **82** 2833–9

[34] McNeil L E, Grimsditch M and French R H 1993 Vibrational Spectroscopy of Aluminum Nitride *Journal of the American Ceramic Society* **76** 1132–6

[35] Deger C, Born E, Angerer H, Ambacher O, Stutzmann M, Hornsteiner J, Riha E and Fischerauer G 1998 Sound velocity of AlxGa1−xN thin films obtained by surface acoustic-wave measurements *Applied Physics Letters* **72** 2400–2

[36] Eller B S, Yang J and Nemanich R J 2014 Polarization Effects of GaN and AlGaN: Polarization Bound Charge, Band Bending, and Electronic Surface States *J. Electron. Mater.* **43** 4560–8

[37] Bernardini F, Fiorentini V and Vanderbilt D 2001 Accurate calculation of polarization-related quantities in semiconductors *Phys. Rev. B* **63** 193201

[38] Ambacher O, Foutz B, Smart J, Shealy J R, Weimann N, Chu K, Murphy M, Sierakowski A, Schaff W, Eastman L, Dimitrov R, Mitchell A and Stutzmann M 2000 Two dimensional electron gases induced by spontaneous and piezoelectric polarization undoped and doped AlGaN/GaN heterostructures *Journal of Applied Physics* **87** 334–44

[39] Amano H, Collazo R, Santi C D, Einfeldt S, Funato M, Glaab J, Hagedorn S, Hirano A, Hirayama H, Ishii R, Kashima Y, Kawakami Y, Kirste R, Kneissl M, Martin R, Mehnke F, Meneghini M, Ougazzaden A, Parbrook P J, Rajan S, Reddy P, Römer F, Ruschel J, Sarkar B, Scholz F, Schowalter L J, Shields P, Sitar Z, Sulmoni L, Wang T, Wernicke T, Weyers M, Witzigmann B, Wu Y-R, Wunderer T and Zhang Y 2020 The 2020 UV emitter roadmap *J. Phys. D: Appl. Phys.* **53** 503001

[40] Takano T, Mino T, Sakai J, Noguchi N, Tsubaki K and Hirayama H 2017 Deep-ultraviolet light-emitting diodes with external quantum efficiency higher than 20% at 275 nm achieved by improving light-extraction efficiency *Appl. Phys. Express* **10** 031002

[41] Oto T, Banal R G, Kataoka K, Funato M and Kawakami Y 2010 100 mW deep-ultraviolet emission from aluminium-nitride-based quantum wells pumped by an electron beam *Nature Photonics* **4** 767–70

[42] Wang Y, Rong X, Ivanov S, Jmerik V, Chen Z, Wang H, Wang T, Wang P, Jin P, Chen Y, Kozlovsky V, Sviridov D, Zverev M, Zhdanova E, Gamov N, Studenov V, Miyake H, Li H, Guo S, Yang X, Xu F, Yu T, Qin Z, Ge W, Shen B and Wang X 2019 Deep Ultraviolet Light Source from Ultrathin GaN/AlN MQW Structures with Output Power Over 2 Watt *Advanced Optical Materials* **7** 1801763

[43] Dimkou I, Harikumar A, Ajay A, Donatini F, Bellet-Amalric E, Grenier A, den Hertog M I, Purcell S T and Monroy E 2019 Design of AlGaN/AlN Dot-in-a-wire Heterostructures for Electron-Pumped UV Emitters *Phys. Status Solidi A* pssa.201900714

[44] Leamy H J 1982 Charge collection scanning electron microscopy *Journal of Applied Physics* **53** R51–80

[45] Everhart T E and Hoff P H 1971 Determination of Kilovolt Electron Energy Dissipation vs Penetration Distance in Solid Materials *Journal of Applied Physics* **42** 5837–46

[46] Karpov S Y and Makarov Y N 2002 Dislocation effect on light emission efficiency in gallium nitride *Applied Physics Letters* **81** 4721

[47] Kneissl M and Rass J 2016 *III-Nitride Ultraviolet Emitters: Technology and Applications* (Cham: Springer International Publishing : Imprint: Springer)

[48] Ozol D I, Sheshin E P, Danilkin M I and Vereschagina N Yu 2020 Cathodoluminescent UV Sources for Biomedical Applications *4th International Conference on Nanotechnologies and Biomedical Engineering* IFMBE Proceedings vol 77, ed I Tiginyanu, V Sontea and S Railean (Cham: Springer International Publishing) pp 313–7

[49] Ozol D I 2016 Cascade luminescence as a way to increase the energy efficiency of cathodoluminophores *2016 29th International Vacuum Nanoelectronics Conference (IVNC)* 2016 29th International Vacuum Nanoelectronics Conference (IVNC) (Vancouver, BC, Canada: IEEE) pp 1–2

[50] Watanabe K, Taniguchi T, Niiyama T, Miya K and Taniguchi M 2009 Far-ultraviolet plane-emission handheld device based on hexagonal boron nitride *Nature Photon* **3** 591–4

[51] Lee D and Song S H 2017 Ultra-thin ultraviolet cathodoluminescent device based on exfoliated hexagonal boron nitride *RSC Adv.* **7** 7831–5

[52] Shimahara Y, Miyake H, Hiramatsu K, Fukuyo F, Okada T, Takaoka H and Yoshida H 2011 Fabrication of Deep-Ultraviolet-Light-Source Tube Using Si-Doped AlGaN *Appl. Phys. Express* **4** 042103

[53] Matsumoto T, Iwayama S, Saito T, Kawakami Y, Kubo F and Amano H 2012 Handheld deep ultraviolet emission device based on aluminum nitride quantum wells and graphene nanoneedle field emitters *Opt. Express* **20** 24320

[54] Ivanov S V, Jmerik V N, Nechaev D V, Kozlovsky V I and Tiberi M D 2015 E-beam pumped mid-UV sources based on MBE-grown AlGaN MQW: Mid-UV sources based on MBE-grown AlGaN MQW *physica status solidi (a)* **212** 1011–6

[55] Rong X, Wang X, Ivanov S V, Jiang X, Chen G, Wang P, Wang W, He C, Wang T, Schulz T, Albrecht M, Jmerik V N, Toropov A A, Ratnikov V V, Kozlovsky V I, Martovitsky V P, Jin P, Xu F, Yang X, Qin Z, Ge W, Shi J and Shen B 2016 High-Output-Power Ultraviolet Light Source from Quasi-2D GaN Quantum Structure *Adv. Mater.* **28** 7978–83

[56] Tabataba-Vakili F, Wunderer T, Kneissl M, Yang Z, Teepe M, Batres M, Feneberg M, Vancil B and Johnson N M 2016 Dominance of radiative recombination from electron-beam-pumped deep-UV AlGaN multi-quantum-well heterostructures *Appl. Phys. Lett.* **109** 181105

[57] Jmerik V N, Nechaev D V, Toropov A A, Evropeitsev E A, Kozlovsky V I, Martovitsky V P, Rouvimov S and Ivanov S V 2018 High-efficiency electron-beam-pumped sub-240-nm ultraviolet emitters based on ultra-thin GaN/AlN multiple quantum wells grown by plasma-assisted molecular-beam epitaxy on *c* -Al $_2$ O $_3$ *Appl. Phys. Express* **11** 091003

[58] Yoo S T, So B, Lee H I, Nam O and Chang Park K 2019 Large area deep ultraviolet light of Al $_{0.47}$ Ga $_{0.53}$ N/Al $_{0.56}$ Ga $_{0.44}$ N multi quantum well with carbon nanotube electron beam pumping *AIP Advances* **9** 075104

[59] Ichikawa N, Ikeda K, Honda Y, Taketomi H, Kawai K and Suzuki T 2016 Development of a UV Light Source Using Pr:LuAG Thin Film Pumped by Electron Beam *Electron Comm Jpn* **99** 33–9

[60] Yoo S T, Hong J H, Kang J S and Park K C 2018 Deep-ultraviolet light source with a carbon nanotube cold-cathode electron beam *Journal of Vacuum Science & Technology B* **36** 02C103

[61] Yoo S T, Lee H I and Park K C 2019 363 nm UVA light generation with carbon nanotube electron emitters *Microelectronic Engineering* **218** 111142

[62] Renard J, Kandaswamy P K, Monroy E and Gayral B 2009 Suppression of nonradiative processes in long-lived polar GaN/AlN quantum dots *Applied Physics Letters* **95** 131903

[63] Gačević Ž, Das A, Teubert J, Kotsar Y, Kandaswamy P K, Kehagias Th, Koukoula T, Komninou Ph and Monroy E 2011 Internal quantum efficiency of III-nitride quantum dot superlattices grown by plasma-assisted molecular-beam epitaxy *Journal of Applied Physics* **109** 103501

[64] Himwas C, den Hertog M, Bellet-Amalric E, Songmuang R, Donatini F, Si Dang L and Monroy E 2014 Enhanced room-temperature mid-ultraviolet emission from AlGaN/AlN Stranski-Krastanov quantum dots *Journal of Applied Physics* **116** 023502

[65] Harikumar A, Donatini F, Bougerol C, Bellet-Amalric E, Thai Q-M, Dujardin C, Dimkou I, Purcell S T and Monroy E 2020 Internal quantum efficiency of AlGaN/AlN quantum dot superlattices for electron-pumped ultraviolet sources *Nanotechnology* **31** 505205

[66] Hestroffer K 2012 *Croissance et caractérisation de nanofils de GaN et d'hétérostructures filaires de GaN/AlN* PhD Thesis (Grenoble: Université Grenoble Alpes)

[67] Nötzel R 1996 Self-organized growth of quantum-dot structures *Semicond. Sci. Technol.* **11** 1365–79

[68] Karczewski G, Maćkowski S, Kutrowski M, Wojtowicz T and Kossut J 1999 Photoluminescence study of CdTe/ZnTe self-assembled quantum dots *Appl. Phys. Lett.* **74** 3011–3

[69] Mariette H 2005 Formation of self-assembled quantum dots induced by the Stranski–Krastanow transition: a comparison of various semiconductor systems *Comptes Rendus Physique* **6** 23–32

[70] Cho A Y and Arthur J R 1975 Molecular beam epitaxy *Progress in Solid State Chemistry* **10** 157–91

[71] Lim C B 2017 *Hétérostructures GaN/Al(Ga)N pour l'optoélectronique infrarouge : orientations polaires et non-polaires* PhD Thesis (Grenoble: Université Grenoble Alpes)

[72] Hasegawa S 2012 Reflection High-Energy Electron Diffraction *Characterization of Materials* (John Wiley & Sons, Ltd) pp 1–14

[73] Mahan J E, Geib K M, Robinson G Y and Long R G 1998 A review of the geometrical fundamentals of reflection high-energy electron diffraction with application to silicon surfaces *Journal of Vacuum Science & Technology A: Vacuum, Surfaces, and Films* **8** 3692

[74] Ohring M 2001 *Materials Science of Thin Films.* (Burlington: Elsevier)

[75] Ambacher O 1998 Growth and applications of Group III-nitrides *Journal of Physics D: Applied Physics* **31** 2653–710

[76] Kandaswamy P K 2010 *Al(Ga)N/GaN nanostructures for intersubband optoelectronics in the near- and mid-infrared* PhD Thesis (Grenoble: Université Grenoble Alpes)

[77] Lee J-H and Im K-S 2021 Growth of High Quality GaN on Si (111) Substrate by Using Two-Step Growth Method for Vertical Power Devices Application *Crystals* **11** 234

[78] Himwas C, Hertog M den, Donatini F, Dang L S, Rapenne L, Sarigiannidou E, Songmuang R and Monroy E 2013 AlGaN/AlN quantum dots for UV light emitters *physica status solidi c* **10** 285–8

[79] Himwas C 2015 *Nitride based nanostructures for ultraviolet emission* PhD Thesis (Grenoble: Université Grenoble Alpes)

[80] Lieberman M A and Lichtenberg A J 2005 Chemical Kinetics and Surface Processes *Principles of Plasma Discharges and Materials Processing* (Hoboken, NJ, USA: John Wiley & Sons, Inc.) pp 285–325

[81] Adelmann C, Brault J, Mula G, Daudin B, Lymperakis L and Neugebauer J 2003 Gallium adsorption on (0001) GaN surfaces *Phys. Rev. B* **67** 165419

[82] Heying B, Averbeck R, Chen L F, Haus E, Riechert H and Speck J S 2000 Control of GaN surface morphologies using plasma-assisted molecular beam epitaxy *Journal of Applied Physics* **88** 1855–60

[83] Kandaswamy P K, Guillot F, Bellet-Amalric E, Monroy E, Nevou L, Tchernycheva M, Michon A, Julien F H, Baumann E, Giorgetta F R, Hofstetter D, Remmele T, Albrecht M, Birner S and Dang L S 2008 GaN/AlN short-period superlattices for intersubband optoelectronics: A systematic study of their epitaxial growth, design, and performance *Journal of Applied Physics* **104** 093501

[84] Myoung J M, Gluschenkov O, Kim K and Kim S 1999 Growth kinetics of GaN and effects of flux ratio on the properties of GaN films grown by plasma-assisted molecular beam epitaxy *Journal of Vacuum Science & Technology A: Vacuum, Surfaces, and Films* **17** 3019–28

[85] Adelmann H C 2002 *Growth and strain relaxation mechanisms of group III nitride heterostructures* PhD Thesis (Grenoble: Université Joseph Fourier)

[86] Neugebauer J, Zywietz T, Scheffler M, Northrup J, Chen H and Feenstra R 2003 Adatom Kinetics On and Below the Surface: The Existence of a New Diffusion Channel *Physical Review Letters* **90** 056101

[87] Northrup J, Neugebauer J, Feenstra R and Smith A 2000 Structure of GaN(0001) : The laterally contracted Ga bilayer model *Physical Review B* **61** 9932–5

[88] Koblmueller G, Averbeck R, Geelhaar L, Riechert H, Hösler W and Pongratz P 2003 Growth diagram and morphologies of AlN thin films grown by molecular beam epitaxy *Journal of Applied Physics* **93** 9591–7

[89] Iliopoulos E and Moustakas T D 2002 Growth kinetics of AlGaN films by plasma-assisted molecular-beam epitaxy *Applied Physics Letters* **81** 295–7

[90] Monroy E, Daudin B, Bellet-Amalric E, Gogneau N, Jalabert D, Enjalbert F, Brault J, Barjon J and Dang L S 2003 Surfactant effect of In for AlGaN growth by plasma-assisted molecular beam epitaxy *Journal of Applied Physics* **93** 1550–6

[91] Takayanagi K, Tanishiro Y, Takahashi M and Takahashi S 1985 Structural analysis of Si(111)-7×7 by UHV-transmission electron diffraction and microscopy *Journal of Vacuum Science & Technology A* **3** 1502–6

[92] Cherns D, Meshi L, Griffiths I, Khongphetsak S, Novikov S V, Farley N, Campion R P and Foxon C T 2008 Defect reduction in GaN/(0001)sapphire films grown by molecular beam epitaxy using nanocolumn intermediate layers *Applied Physics Letters* **92** 121902

[93] Brubaker M D, Levin I, Davydov A V, Rourke D M, Sanford N A, Bright V M and Bertness K A 2011 Effect of AlN buffer layer properties on the morphology and polarity of GaN nanowires grown by molecular beam epitaxy *Journal of Applied Physics* **110** 053506

[94] Musolino M, Tahraoui A, Fernández-Garrido S, Brandt O, Trampert A, Geelhaar L and Riechert H 2015 Compatibility of the selective area growth of GaN nanowires on AlN-buffered Si substrates with the operation of light emitting diodes *Nanotechnology* **26** 085605

[95] Schenk H P D, Kipshidze G D, Kaiser U, Fissel A, Kräußlich J, Schulze J and Richter W 1999 Investigation of two-dimensional growth of AlN(0001) on Si(111) by plasma-assisted molecular beam epitaxy *Journal of Crystal Growth* **200** 45–54

[96] Himwas C, Hertog M den, Dang L S, Monroy E and Songmuang R 2014 Alloy inhomogeneity and carrier localization in AlGaN sections and AlGaN/AlN nanodisks in nanowires with 240–350 nm emission *Applied Physics Letters* **105** 241908

[97] Adelmann C, Gogneau N, Sarigiannidou E, Rouvière J-L and Daudin B 2002 GaN islanding by spontaneous rearrangement of a strained two-dimensional layer on (0001) AlN *Appl. Phys. Lett.* **81** 3064–6

[98] Gogneau N, Jalabert D, Monroy E, Shibata T, Tanaka M and Daudin B 2003 Structure of GaN quantum dots grown under "modified Stranski–Krastanow" conditions on AlN *Journal of Applied Physics* **94** 2254–61

[99] Daudin B, Widmann F, Feuillet G, Samson Y, Arlery M and Rouvière J 1997 Stranski-Krastanov growth mode during the molecular beam epitaxy of highly strained GaN *Physical Review B* **56** R7069–72

[100] Guillot F, Bellet-Amalric E, Monroy E, Tchernycheva M, Nevou L, Doyennette L, Julien F H, Dang L S, Remmele T, Albrecht M, Shibata T and Tanaka M 2006 Si-doped GaN⁄AlN quantum dot superlattices for optoelectronics at telecommunication wavelengths *Journal of Applied Physics* **100** 044326

[101] Damilano B, Grandjean N, Semond F, Massies J and Leroux M 1999 From visible to white light emission by GaN quantum dots on Si(111) substrate *Applied Physics Letters* **75** 962–4

[102] Gogneau N, Sarigiannidou E, Monroy E, Monnoye S, Mank H and Daudin B 2004 Surfactant effect of gallium during the growth of GaN on AlN(0001¯) by plasma-assisted molecular beam epitaxy *Appl. Phys. Lett.* **85** 1421–3

[103] Brown J, Wu F, Petroff P M and Speck J S 2004 GaN quantum dot density control by rf-plasma molecular beam epitaxy *Appl. Phys. Lett.* **84** 690–2

[104] Horcas I, Fernández R, Gómez-Rodríguez J M, Colchero J, Gómez-Herrero J and Baro A M 2007 WSXM: A software for scanning probe microscopy and a tool for nanotechnology *Review of Scientific Instruments* **78** 013705

[105] Fairbairn M W and Moheimani S O R 2013 Control Techniques for Increasing the Scan Speed and Minimizing Image Artifacts in Tapping-Mode Atomic Force Microscopy: Toward Video-Rate Nanoscale Imaging *IEEE Control Systems Magazine* **33** 46–67

[106] García R and Pérez R 2002 Dynamic atomic force microscopy methods *Surface Science Reports* **47** 197–301

[107] Wiesendanger R and Roland W 1994 *Scanning Probe Microscopy and Spectroscopy: Methods and Applications* (Cambridge University Press)

[108] Schroder D K 2005 Frontmatter *Semiconductor Material and Device Characterization* (Hoboken, NJ, USA: John Wiley & Sons, Inc.) pp i–xv

[109] Calle F, Sánchez F J, Tijero J M G, Sánchez-García M A, Calleja E and Beresford R 1997 Exciton and donor - acceptor recombination in undoped GaN on Si(111) *Semiconductor Science and Technology* **12** 1396–403

[110] Shan W, Little B D, Fischer A J, Song J J, Goldenberg B, Perry W G, Bremser M D and Davis R F 1996 Binding energy for the intrinsic excitons in wurtzite GaN *Phys. Rev. B* **54** 16369–72

[111] Shatalov M, Yang J, Sun W, Kennedy R, Gaska R, Liu K, Shur M and Tamulaitis G 2009 Efficiency of light emission in high aluminum content AlGaN quantum wells *Journal of Applied Physics* **105** 073103

[112] Ban K, Yamamoto J, Takeda K, Ide K, Iwaya M, Takeuchi T, Kamiyama S, Akasaki I and Amano H 2011 Internal Quantum Efficiency of Whole-Composition-Range AlGaN Multiquantum Wells *Appl. Phys. Express* **4** 052101

[113] Bryan Z, Bryan I, Xie J, Mita S, Sitar Z and Collazo R 2015 High internal quantum efficiency in AlGaN multiple quantum wells grown on bulk AlN substrates *Appl. Phys. Lett.* **106** 142107

[114] Murotani H, Akase D, Anai K, Yamada Y, Miyake H and Hiramatsu K 2012 Dependence of internal quantum efficiency on doping region and Si concentration in Al-rich AlGaN quantum wells *Appl. Phys. Lett.* **101** 042110

[115] Liao Y, Thomidis C, Kao C and Moustakas T D 2011 AlGaN based deep ultraviolet light emitting diodes with high internal quantum efficiency grown by molecular beam epitaxy *Appl. Phys. Lett.* **98** 081110

[116] Banal R G, Funato M and Kawakami Y 2011 Extremely high internal quantum efficiencies from AlGaN/AlN quantum wells emitting in the deep ultraviolet spectral region *Appl. Phys. Lett.* **99** 011902

[117] Mickevičius J, Tamulaitis G, Shur M, Shatalov M, Yang J and Gaska R 2012 Internal quantum efficiency in AlGaN with strong carrier localization *Appl. Phys. Lett.* **101** 211902

[118] Bhattacharyya A, Moustakas T D, Zhou L, Smith David J and Hug W 2009 Deep ultraviolet emitting AlGaN quantum wells with high internal quantum efficiency *Appl. Phys. Lett.* **94** 181907

[119] Hao G-D, Tamari N, Obata T, Kinoshita T and Inoue S 2017 Electrical determination of current injection and internal quantum efficiencies in AlGaN-based deep-ultraviolet light-emitting diodes *Opt. Express* **25** A639

[120] Dong P, Yan J, Zhang Y, Wang J, Zeng J, Geng C, Cong P, Sun L, Wei T, Zhao L, Yan Q, He C, Qin Z and Li J 2014 AlGaN-based deep ultraviolet light-emitting diodes grown on nano-patterned sapphire substrates with significant improvement in internal quantum efficiency *Journal of Crystal Growth* **395** 9–13

[121] Frankerl C, Hoffmann M P, Nippert F, Wang H, Brandl C, Tillner N, Lugauer H-J, Zeisel R, Hoffmann A and Davies M J 2019 Challenges for reliable internal quantum efficiency determination in AlGaN-based multi-quantum-well structures posed by carrier transport effects and morphology issues *Journal of Applied Physics* **126** 075703

[122] Dimkou I, Harikumar A, Donatini F, Lähnemann J, den Hertog M I, Bougerol C, Bellet-Amalric E, Mollard N, Ajay A, Ledoux G, Purcell S T and Monroy E 2020 Assessment of AlGaN/AlN superlattices on GaN nanowires as active region of electron-pumped ultraviolet sources *Nanotechnology* **31** 204001

[123] Yacobi B G and Holt D B 1986 Cathodoluminescence scanning electron microscopy of semiconductors *Journal of Applied Physics* **59** R1–24

[124] Donatini F and Dang L S 2010 A single-step electron beam lithography of buried nanostructures using cathodoluminescence imaging and low temperature *Nanotechnology* **21** 375303

[125] Birner S 2011 *Modeling of semiconductor nanostructures and semiconductor–electrolyte interfaces* PhD Thesis (Garching b. München: Technische Universität München)

[126] Fiorentini V, Bernardini F and Ambacher O 2002 Evidence for nonlinear macroscopic polarization in III–V nitride alloy heterostructures *Applied Physics Letters* **80** 1204–6

[127] Bernardini F, Fiorentini V and Vanderbilt D 1997 Spontaneous polarization and piezoelectric constants of III-V nitrides *Phys. Rev. B* **56** R10024–7

[128] Gorczyca I, Suski T, Christensen N E and Svane A 2011 Size effects in band gap bowing in nitride semiconducting alloys *Physical Review B* **83** 153301

[129] Morkoç H 2013 *Nitride Semiconductor Devices: Fundamentals and Applications* (John Wiley & Sons)

[130] Rinke P, Winkelnkemper M, Qteish A, Bimberg D, Neugebauer J and Scheffler M 2008 Consistent set of band parameters for the group-III nitrides AlN, GaN, and InN *Physical Review B* **77** 075202

[131] Yan Q, Rinke P, Janotti A, Scheffler M and Van de Walle C G 2014 Effects of strain on the band structure of group-III nitrides *Phys. Rev. B* **90** 125118

[132] Hovington P, Drouin D and Gauvin R 2006 CASINO: A new monte carlo code in C language for electron beam interaction -part I: Description of the program *Scanning* **19** 1–14

[133] Toth M and Phillips M R 1998 Monte Carlo modeling of cathodoluminescence generation using electron energy loss curves *Scanning* **20** 425–32

[134] Barrigón E, Heurlin M, Bi Z, Monemar B and Samuelson L 2019 Synthesis and Applications of III–V Nanowires *Chem. Rev.* **119** 9170–220

[135] Renard J, Songmuang R, Bougerol C, Daudin B and Gayral B 2008 Exciton and Biexciton Luminescence from Single GaN/AlN Quantum Dots in Nanowires *Nano Letters* **8** 2092–6

[136] Nguyen H P T, Cui K, Zhang S, Fathololoumi S and Mi Z 2011 Full-color InGaN/GaN dot-in-a-wire light emitting diodes on silicon *Nanotechnology* **22** 445202

[137] Holmes M J, Choi K, Kako S, Arita M and Arakawa Y 2014 Room-Temperature Triggered Single Photon Emission from a III-Nitride Site-Controlled Nanowire Quantum Dot *Nano Lett.* **14** 982–6

[138] Gačević Ž, Vukmirović N, García-Lepetit N, Torres-Pardo A, Müller M, Metzner S, Albert S, Bengoechea-Encabo A, Bertram F, Veit P, Christen J, González-Calbet J M and Calleja E 2016 Influence of composition, strain, and electric field anisotropy on different emission colors and recombination dynamics from InGaN nanodisks in pencil-like GaN nanowires *Phys. Rev. B* **93** 125436

[139] Jahangir S, Mandl M, Strassburg M and Bhattacharya P 2013 Molecular beam epitaxial growth and optical properties of red-emitting (λ = 650 nm) InGaN/GaN disks-in-nanowires on silicon *Appl. Phys. Lett.* **102** 071101

[140] Beeler M, Lim C B, Hille P, Bleuse J, Schörmann J, de la Mata M, Arbiol J, Eickhoff M and Monroy E 2015 Long-lived excitons in GaN/AlN nanowire heterostructures *Phys. Rev. B* **91** 205440

[141] Zagonel L F, Mazzucco S, Tencé M, March K, Bernard R, Laslier B, Jacopin G, Tchernycheva M, Rigutti L, Julien F H, Songmuang R and Kociak M 2011 Nanometer Scale Spectral Imaging of Quantum Emitters in Nanowires and Its Correlation to Their Atomically Resolved Structure *Nano Lett.* **11** 568–73

[142] Rigutti L, Teubert J, Jacopin G, Fortuna F, Tchernycheva M, De Luna Bugallo A, Julien F H, Furtmayr F, Stutzmann M and Eickhoff M 2010 Origin of energy dispersion in Al(x)Ga(1−x)N/GaN nanowire quantum disks with low Al content *Physical Review B* **82** 235308

[143] Furtmayr F, Teubert J, Becker P, Conesa-Boj S, Morante J R, Chernikov A, Schäfer S, Chatterjee S, Arbiol J and Eickhoff M 2011 Carrier confinement in GaN/AlxGa1−xN nanowire heterostructures (0<x≤1) *Physical Review B* **84** 205303

[144] Carnevale S D, Yang J, Phillips P J, Mills M J and Myers R C 2011 Three-Dimensional GaN/AlN Nanowire Heterostructures by Separating Nucleation and Growth Processes *Nano Lett.* **11** 866–71

[145] Rivera C, Jahn U, Flissikowski T, Pau J, Muñoz E and Grahn H T 2007 Strain-confinement mechanism in mesoscopic quantum disks based on piezoelectric materials *Physical Review B* **75** 045316

[146] Zagonel L F, Rigutti L, Tchernycheva M, Jacopin G, Songmuang R and Kociak M 2012 Visualizing highly localized luminescence in GaN/AlN heterostructures in nanowires *Nanotechnology* **23** 455205

[147] Ajay A, Lim C B, Browne D A, Polaczynski J, Bellet-Amalric E, den Hertog M I and Monroy E 2017 Intersubband absorption in Si- and Ge-doped GaN/AlN heterostructures in self-assembled nanowire and 2D layers *physica status solidi (b)* **254** 1600734

[148] Sabelfeld K K, Kaganer V M, Limbach F, Dogan P, Brandt O, Geelhaar L and Riechert H 2013 Height self-equilibration during the growth of dense nanowire ensembles: Order emerging from disorder *Appl. Phys. Lett.* **103** 133105

[149] Tchernycheva M, Nevou L, Doyennette L, Julien F H, Guillot F, Monroy E, Remmele T and Albrecht M 2006 Electron confinement in strongly coupled GaN/AlN quantum wells *Applied Physics Letters* **88** 153113

[150] Kandaswamy P K, Bougerol C, Jalabert D, Ruterana P and Monroy E 2009 Strain relaxation in short-period polar GaN/AlN superlattices *Journal of Applied Physics* **106** 013526

[151] Lim S K, Brewster M, Qian F, Li Y, Lieber C M and Gradečak S 2009 Direct Correlation between Structural and Optical Properties of III−V Nitride Nanowire Heterostructures with Nanoscale Resolution *Nano Lett.* **9** 3940–4

[152] Lähnemann J, Flissikowski T, Wölz M, Geelhaar L, Grahn H T, Brandt O and Jahn U 2016 Quenching of the luminescence intensity of GaN nanowires under electron beam exposure: impact of C adsorption on the exciton lifetime *Nanotechnology* **27** 455706

[153] Robins L H, Bertness K A, Barker J M, Sanford N A and Schlager J B 2007 Optical and structural study of GaN nanowires grown by catalyst-free molecular beam epitaxy. II. Sub-band-gap luminescence and electron irradiation effects *Journal of Applied Physics* **101** 113506

[154] Toropov A A, Shevchenko E A, Shubina T V, Jmerik V N, Nechaev D V, Evropeytsev E A, Kaibyshev V Kh, Pozina G, Rouvimov S and Ivanov S V 2017 AlGaN Nanostructures with Extremely High Room-Temperature Internal Quantum Efficiency of Emission Below 300 nm *Journal of Elec Materi* **46** 3888–93

[155] Toropov A A, Evropeitsev E A, Nestoklon M O, Smirnov D S, Shubina T V, Kaibyshev V Kh, Budkin G V, Jmerik V N, Nechaev D V, Rouvimov S, Ivanov S V and Gil B 2020 Strongly Confined Excitons in GaN/AlN Nanostructures with Atomically Thin GaN Layers for Efficient Light Emission in Deep-Ultraviolet *Nano Lett.* **20** 158–65

[156] Himwas C, Songmuang R, Le Si Dang, Bleuse J, Rapenne L, Sarigiannidou E and Monroy E 2012 Thermal stability of the deep ultraviolet emission from AlGaN/AlN Stranski-Krastanov quantum dots *Applied Physics Letters* **101** 241914

[157] Islam S M, Lee K, Verma J, Protasenko V, Rouvimov S, Bharadwaj S, (Grace) Xing H and Jena D 2017 MBE-grown 232–270 nm deep-UV LEDs using monolayer thin binary GaN/AlN quantum heterostructures *Appl. Phys. Lett.* **110** 041108

[158] Brault J, Matta S, Ngo T-H, Al Khalfioui M, Valvin P, Leroux M, Damilano B, Korytov M, Brändli V, Vennéguès P, Massies J and Gil B 2019 Internal quantum efficiencies of AlGaN quantum dots grown by molecular beam epitaxy and emitting in the UVA to UVC ranges *Journal of Applied Physics* **126** 205701

[159] Yang W, Li J, Zhang Y, Huang P-K, Lu T-C, Kuo H-C, Li S, Yang X, Chen H, Liu D and Kang J 2015 High density GaN/AlN quantum dots for deep UV LED with high quantum efficiency and temperature stability *Sci Rep* **4** 5166

[160] Tanaka S, Lee J-S, Ramvall P and Okagawa H 2003 A UV Light-Emitting Diode Incorporating GaN Quantum Dots *Jpn. J. Appl. Phys.* **42** L885–7

[161] Kowalski W 2009 *Ultraviolet Germicidal Irradiation Handbook: UVGI for Air and Surface Disinfection* (Berlin, Heidelberg: Springer Berlin Heidelberg)

[162] RAMSAY I A, NIEDZIELA J-C and OGDEN I D 2000 The Synergistic Effect of Excimer and Low-Pressure Mercury Lamps on the Disinfection of Flowing Water *Journal of Food Protection* **63** 1529–33

[163] Raeiszadeh M and Adeli B 2020 A Critical Review on Ultraviolet Disinfection Systems against COVID-19 Outbreak: Applicability, Validation, and Safety Considerations *ACS Photonics* **7** 2941–51

[164] Kaidzu S, Sugihara K, Sasaki M, Nishiaki A, Igarashi T and Tanito M 2019 Evaluation of acute corneal damage induced by 222-nm and 254-nm ultraviolet light in Sprague–Dawley rats *Free Radical Research* **53** 611–7

[165] Gogneau N, Fossard F, Monroy E, Monnoye S, Mank H and Daudin B 2004 Effects of stacking on the structural and optical properties of self-organized GaN/AlN quantum dots *Appl. Phys. Lett.* **84** 4224–6

[166] Bickermann M, Epelbaum B M, Filip O, Tautz B, Heimann P and Winnacker A 2012 Faceting in AlN bulk crystal growth and its impact on optical properties of the crystals *Phys. Status Solidi C* **9** 449–52

[167] Koppe T, Hofsäss H and Vetter U 2016 Overview of band-edge and defect related luminescence in aluminum nitride *Journal of Luminescence* **178** 267–81

[168] Collazo R, Xie J, Gaddy B E, Bryan Z, Kirste R, Hoffmann M, Dalmau R, Moody B, Kumagai Y, Nagashima T, Kubota Y, Kinoshita T, Koukitu A, Irving D L and Sitar Z 2012 On the origin of the 265 nm absorption band in AlN bulk crystals *Appl. Phys. Lett.* **100** 191914

[169] Webpage: Optical Design Solutions: https://www.synopsys.com/optical-solutions.html

[170] Zhang G and Wang D 2009 Colloidal Lithography—The Art of Nanochemical Patterning *Chemistry – An Asian Journal* **4** 236–45

[171] Liu J, Chen C, Yang G, Chen Y and Yang C-F 2017 Effect of the Fabrication Parameters of the Nanosphere Lithography Method on the Properties of the Deposited Au-Ag Nanoparticle Arrays *Materials* **10** 381

This project is a contribution to the development of high-brightness, mercury-free, 100% recyclable and high-gloss ultraviolet (UV) lamps for disinfection at 270 nm. The performance of AlGaN-based UV LEDs remains limited by carrier injection problems, due to the high activation energy of dopants in this material and the difficulties to implement ohmic contacts. To circumvent these problems, we propose to pump an active region based on AlGaN nanostructures with an electron beam. For investigating the active media for electron-pumped UV lamps for disinfection, two types of heterostructures are considered, namely AlGaN/AlN quantum dots (QDs) embedded in GaN nanowires (NWs) synthesized on Si(111) substrates and AlGaN/AlN QDs grown by the Stranski-Krastanov (SK) method on AlN-on-sapphire templates. These choices were based on the high internal quantum efficiency (IQE) that can be achieved in QDs thanks to the three dimensional confinement of carriers. The growth of all the structures was performed by plasma-assisted molecular beam epitaxy.

The first stage of the work involved establishing the feasibility of QDs on NWs for this application. Structural and optical studies demonstrated that the QD dimensions were quite homogeneous along the 400-nm-long superlattice (SL), giving a single emission line tunable in the range from 340 to 258 nm. We demonstrated IQE levels higher than 60% at 340 nm at room temperature, decreasing when reducing the emission wavelength. At 270 nm, the IQE was around 30%. These values were obtained under low injection, but remain stable for pumping densities up to 200 kW/cm^2. Under electron beam pumping, channeling effects due to the NW geometry can be compensated by increasing the active region length by 60% in comparison to planar layers. The external quantum efficiency under optical pumping provides promising results (3.42±0.55%).

The second stage of the work involved studying AlGaN/AlN SK-QD SLs. It is demonstrated that by modifying the III/V ratio and/or the composition of the QDs, the peak emission wavelength can be tuned from 225 nm to 335 nm while keeping the IQE around 50% in the 250-335 nm range, and higher than 35% in the 225-250 nm range. The IQE of these nanostructures remain stable from low to high injection power densities up to 200 kW/cm^2. An average power efficiency of 0.38% is measured for as-grown structures, and that without any treatment to improve the light extraction efficiency or thermal management. These results are very promising for the development of an efficient, environment friendly UV technology for disinfection.

Keywords: AlGaN, quantum dots, nanowires, molecular beam epitaxy, electron pumping, lamp, ultraviolet

---

Ce projet est une contribution au développement de lampes ultraviolettes (UV) à haute luminosité, sans mercure, 100 % recyclables et à haute brillance, pour la désinfection à 270 nm. Les performances des LED UV à base d'AlGaN restent limitées par des problèmes d'injection de porteurs, dus à la haute énergie d'activation des dopants dans ce matériau et aux difficultés de mise en œuvre des contacts ohmiques. Pour contourner ces problèmes, nous proposons de pomper une région active à base de nanostructures d'AlGaN avec un faisceau d'électrons. Pour étudier les milieux actifs des lampes UV à pompage électronique pour la désinfection, deux types d'hétérostructures sont considérés, à savoir les boîtes quantiques (BQs) AlGaN/AlN intégrées dans des nanofils (NFs) GaN synthétisés sur des substrats Si(111) et les BQs AlGaN/AlN développées par la méthode Stranski-Krastanov (SK) sur des matrices AlN sur saphir. Ces choix étaient basés sur la haute efficacité quantique interne (IQE) qui peut être atteinte dans les BQ grâce au confinement tridimensionnel des porteurs. La croissance de toutes les structures a été réalisée par épitaxie par jets moléculaires assistée par plasma.

La première étape du travail a consisté à établir la faisabilité des BQ dans les NFs pour cette application. Des études structurelles et optiques ont démontré que les dimensions des BQs étaient assez homogènes le long du super-réseau (SR) de 400 nm de long, donnant une seule raie d'émission accordable dans la plage de 340 à 258 nm. Nous avons démontré des niveaux d'IQE supérieurs à 60% à 340 nm à température ambiante, diminuant lors de la réduction de la longueur d'onde d'émission. A 270 nm, l'IQE était d'environ 30 %. Ces valeurs ont été obtenues sous faible injection, mais restent stables pour des densités de pompage jusqu'à 200 kW/cm^2. Sous pompage par faisceau d'électrons, les effets de canalisation dus à la géométrie NF peuvent être compensés en augmentant la longueur de la région active de 60 % par rapport aux couches planaires. L'efficacité quantique externe sous pompage optique donne des résultats prometteurs (3,42±0,55%).

La deuxième étape du travail a consisté à étudier les SRs de BQs SK AlGaN/AlN. Il est démontré qu'en modifiant le rapport III/V et/ou la composition des BQs, la longueur d'onde d'émission maximale peut être réglée de 225 nm à 335 nm, tout en maintenant l'IQE autour de 50 % dans la gamme 250-335 nm, et plus de 35 % dans la gamme 225-250 nm. L'IQE de ces nanostructures reste stable des densités de puissance d'injection faibles jusqu'à 200 kW/cm^2. Un rendement énergétique moyen de 0,38 % est mesuré pour les structures brutes de croissance, et cela sans aucun traitement pour améliorer l'efficacité d'extraction de la lumière ou la gestion thermique. Ces résultats sont très prometteurs pour le développement d'une technologie UV efficace et respectueuse de l'environnement pour la désinfection.

Mots clés: AlGaN, boîtes quantiques, nanofils, épitaxie par jets moléculaires, pompage d'électrons, lampe, UV